



High aspect ratio sub-micron structuring of transparent materials using non-diffractive ultrafast laser beams : dynamics and interaction regimes

Praveen Kumar Velpula

► To cite this version:

Praveen Kumar Velpula. High aspect ratio sub-micron structuring of transparent materials using non-diffractive ultrafast laser beams : dynamics and interaction regimes. Optics / Photonic. Université Jean Monnet - Saint-Etienne, 2015. English. NNT : 2015STET4005 . tel-01433865

HAL Id: tel-01433865

<https://theses.hal.science/tel-01433865>

Submitted on 13 Jan 2017

HAL is a multi-disciplinary open access archive for the deposit and dissemination of scientific research documents, whether they are published or not. The documents may come from teaching and research institutions in France or abroad, or from public or private research centers.

L'archive ouverte pluridisciplinaire **HAL**, est destinée au dépôt et à la diffusion de documents scientifiques de niveau recherche, publiés ou non, émanant des établissements d'enseignement et de recherche français ou étrangers, des laboratoires publics ou privés.

Université Jean Monnet – Saint-Étienne

L'école doctorale “Sciences, Ingénierie, Santé”

Structuration sub-micronique de matériaux transparents à haut rapport d'aspect par faisceaux laser ultra-rapides non-diffractifs: dynamique et rgimes d'interaction

par

Praveen Kumar VELPULA

Thèse présentée pour obtenir le grade de Docteur en Sciences
en spécialité Optique, photonique et hyperfréquences.

Soutenue le 24 Mars 2015 devant le jury composé de:

Dr. S. GUIZARD	Ecole Polytechnique, Paris	Rapporteur
Dr. F. COURVOISIER	Université de Franche-Comté, Besancon	Rapporteur
Prof. J. SOLIS	Instituto de Óptica – CSIC, Madrid	Examinateur
Dr. B. POUMELLE	Université Paris-Sud, Orsay	Examinateur
Prof. F. GARRELIE	Université Jean Monnet, Saint-Étienne	Examinateur
Prof. Y. OUERDANE	Université Jean Monnet, Saint-Étienne	Examinateur
Dr. R. STOIAN	Université Jean Monnet, Saint-Étienne	Directeur
Dr. J-P. COLOMBIER	Université Jean Monnet, Saint-Étienne	Co-Directeur

Jean Monnet University – Saint-Étienne

High aspect ratio sub-micron structuring of transparent materials using non-diffractive ultrafast laser beams: dynamics and interaction regimes

by

Praveen Kumar VELPULA

Thesis presented in partial fulfillment of the requirements
for the degree of Doctor of Philosophy
in the subject of Optics, photonics and hyperfrequencies.

Defended on 24 March 2015 before the committee:

Dr. S. GUIZARD	Ecole Polytechnique, Paris
Dr. F. COURVOISIER	Université de Franche-Comté, Besancon
Prof. J. SOLIS	Instituto de Óptica – CSIC, Madrid
Dr. B. POUMELLE	Université Paris-Sud, Orsay
Prof. F. GARRELIE	Université Jean Monnet, Saint-Étienne
Prof. Y. OUERDANE	Université Jean Monnet, Saint-Étienne
Dr. R. STOIAN	Université Jean Monnet, Saint-Étienne
Dr. J-P. COLOMBIER	Université Jean Monnet, Saint-Étienne

Abstract

This thesis is focused on the controllability of laser-induced refractive index changes at sub-micron level over long dimensions i.e., with high aspect ratios and sections on the nanoscale. To this end, we explore non-diffractive zeroth-order ultrafast Bessel beams and factors contributing to energy confinement beyond the diffraction limit. Laser processing of transparent materials using non-diffracting beams offers a strong advantage for high aspect ratio sub-micron structures inside the bulk in view of nanophotonics and nanofluidics applications. We present the role of various focusing conditions and laser parameters on material modification in bulk fused silica and explore the different interaction regimes. This thesis tackles mostly the moderate focusing conditions as they offer a stable interaction regime backed up dispersion engineering over a large range of laser parameters. The laser pulse duration was found to be key in defining the type of laser induced refractive index or structural modification. For instance, machining using femtosecond laser pulses results in increased refractive index structures whereas picosecond laser pulses result in uniform void i.e., low index structures.

To acquire better control over the laser energy deposition and precision, a range of physical mechanisms responsible for the laser induced damage in non-diffractive excitation conditions have been observed experimentally and further interrogated by simulations indicating a critical role of light scattering on carriers. Time-resolved pump-probe microscopy measurements with a sub-picosecond temporal and sub-micron spatial resolution allow access to the instantaneous excitation and relaxation dynamics. Dynamic optical transmission and phase contrast offer complementary information of either electronic and glass matrix response. Primarily, ultrafast dynamics of free carriers was studied as the electron mediated energy transfer to the lattice is key to the subsequent material transformation. Role of instantaneous excitation at different laser pulse durations and energies is outlined. Then complete carrier dynamics is presented at different laser parameters. Particularly dynamics in conditions of positive refractive index structures and uniform voids is indicating two different paths of electronic relaxation and energy deposition: a fast defect mediated relaxation for positive index structures and slow thermomechanical relaxation for nanosize void structures. Finally, by correlating the results of time resolved studies, simulations and post-irradiated photoluminescence results, we formulate potential formation scenarios for the positive refractive index and low index or uniform void structures.

Résumé

Cette thèse se concentre sur la contrôlabilité de l'indice de réfraction au niveau sub-micronique par changements d'indice induits par laser sur de longues dimensions i.e., avec des hauts rapports d'aspect élevés et des sections à l'échelle nanométrique. À cette fin, nous explorons les faisceaux ultracourts de Bessel non-diffractifs d'ordre zéro et les facteurs qui contribuent au confinement de l'énergie au-delà de la limite de diffraction. Le traitement par laser de matériaux transparents à l'aide de faisceaux non diffractifs offre un avantage important pour les structures sub-microniques en volume de haut rapport d'aspect à des fins applicatives en nanophotonique et en nanofluidique. Nous présentons l'effet de différentes conditions de focalisation et de paramètres laser sur la modification de la silice fondue, explorant ainsi les différents régimes d'interaction. Cette thèse aborde essentiellement des conditions modérées de focalisation car elles offrent un régime d'interaction stable sur une large gamme de paramètres laser, permettant l'ingénierie de la dispersion. La durée de l'impulsion laser s'est révélée être essentielle dans la définition du type de modification de l'indice de réfraction ou de modification structurale. Par exemple, l'usinage utilisant des impulsions laser femtosecondes entraîne une augmentation des structures d'indice de réfraction alors que les impulsions laser picosecondes engendrent une cavité uniforme i.e., des structures de faible indice.

Pour acquérir un meilleur contrôle et une meilleure précision du dépôt d'énergie laser, un ensemble de mécanismes physiques responsables des dommages induits par laser dans des conditions d'excitation non-diffractives a été observé expérimentalement et examiné par des simulations indiquant le rôle essentiel de la diffusion de la lumière sur les électrons. Des mesures de microscopie pompe-sonde résolues en temps avec une résolution temporelle sub-picoseconde et spatiale sub-micronique donnent accès à l'excitation et à la relaxation dynamique instantanées. La transmission optique dynamique et le contraste de phase offrent des informations complémentaires sur la réponse électronique ou sur celle de la matrice vitreuse. La dynamique ultra-rapide des porteurs libres a été particulièrement étudiée puisque le transfert d'énergie des électrons vers le réseau est la clé de transformation ultérieure du matériau. Le rôle de l'excitation instantanée pour différentes durées et énergie d'impulsion laser est exposé. Ainsi, la dynamique complète des porteurs de charge est présentée pour différents paramètres du laser. En particulier, la dynamique d'obtention de structures d'indice de réfraction positif et des cavités uniformes indique deux chemins différents de relaxation

électronique et de dépôt de l'énergie: une relaxation rapide par l'intermédiaire de défauts pour les structures d'indice positif et une relaxation thermomécanique lente pour les cavités nanométriques. Enfin, en corrélant les résultats des études résolues en temps, les simulations et les résultats de photoluminescence après irradiation, nous formulons des scénarios potentiels de formation de l'indice de réfraction positif ainsi que des structures d'indice faible ou de vides uniformes.

Chapitre 1

Ce chapitre donne une vue d'ensemble et le contexte du travail présenté.

Chapitre 2

Ce chapitre décrit les fondements théoriques concernant le travail présenté dans cette thèse.

Chapitre 3

Ce chapitre décrit l'environnement expérimental et fournit une description technique des expériences mises en œuvre dans la thèse.

Chapitre 4

Ce chapitre décrit la fabrication de structures sub-microniques permanentes à haut rapport d'aspect en utilisant une unique impulsion laser ultrarapide par faisceaux de Bessel, associée à l'étude de différents régimes d'interaction par des simulations.

Chapitre 5

Ce chapitre se concentre sur le rôle de l'excitation maximale instantanée de type Bessel sur la modification du matériau par rapport aux paramètres du laser en utilisant la microscopie instantane pompe-sonde.

Chapitre 6

Ce chapitre décrit la dynamique sous-jacente des mécanismes physiques qui conduisent à différentes modifications structurales dans la silice fondue en utilisant l'excitation par faisceaux de Bessel non-diffractifs.

Chapitre 7

Ce chapitre résume les principales contributions pour la fabrication de structures à haut rapport d'aspect et les aspects fondamentaux de l'interaction. Aussi, nous commentons brièvement la portée et les perspectives du travail présenté.

Contents

1	Introduction	1
2	Theoretical background	5
2.1	Fundamental aspects of laser-matter interaction	5
2.1.1	Nonlinear excitation mechanisms	6
2.1.2	Drude model: optical properties	8
2.1.3	Kerr self-focusing and carrier defocusing effects	10
2.1.4	Relaxation mechanisms	11
2.2	Zeroth-order Bessel beams	15
2.2.1	Basic concepts and generation techniques of Bessel beams	16
2.2.2	Nonlinear interaction of Bessel beams	19
2.3	Conclusions	23
3	Experimental details	25
3.1	Laser system	25
3.2	Experimental setup	27
3.2.1	Generation of Bessel beams and sub-micron structuring	27
3.2.2	Ultrafast time resolved imaging	30
3.3	Working principle of the microscope	34
3.3.1	Optical transmission microscopy	35
3.3.2	Phase contrast microscopy	35
3.4	FDTD simulations: transmissivity vs electron density	39
3.5	Post irradiation techniques	41
3.6	Conclusions	41
4	Material processing using single shot ultrafast Bessel beams	43
4.1	Overview: importance of zeroth order Bessel beams for high aspect ratio structuring	44
4.2	Role of Bessel cone angle	46
4.3	Role of laser pulse duration	49

4.4	Material processing in femtosecond regime	53
4.4.1	Role of energy	53
4.4.2	Accumulation effect	54
4.5	Material processing in picosecond regime	56
4.6	Different interaction regimes with laser pulse duration and en- ergy	59
4.7	Nonlinear simulation results	61
4.7.1	Simulation results in femtosecond regime	62
4.7.2	Simulation results in picosecond regime	64
4.7.3	Energy deposition per electron	68
4.7.4	Role of free carrier damping time	69
4.7.5	Discussion: simulation results	69
4.8	Conclusions	71
5	Role of instantaneous (peak) Bessel excitation for material modification	73
5.1	Overview: Time-resolved studies for laser material processing .	73
5.2	Role of laser pulse duration on free carrier generation	75
5.3	Role of laser energy on free carrier generation	78
5.4	Plasma luminescence studies	82
5.4.1	Femtosecond regime	83
5.4.2	Picosecond regime	86
5.5	Role of probe wavelength	89
5.5.1	Femtosecond regime	89
5.5.2	Picosecond regime	90
5.5.3	Estimation of free carrier damping time	90
5.6	Role of probe polarization	91
5.7	Comments on estimated free carrier density	93
5.8	Conclusions	94
6	Ultrafast dynamics of Bessel excited material modification	97
6.1	Introduction	97
6.2	Dynamics of type-I positive refractive index structures	98
6.2.1	Around the damage threshold	99
6.2.2	Above and below the damage threshold	101
6.2.3	At higher energy	104
6.3	Dynamics of type-II uniform void structures	106
6.4	Potential formation mechanisms	109
6.4.1	Formation mechanisms of increased (smooth) refrac- tive index structures	111
6.4.2	Formation mechanisms of uniform voids	113

6.5	Dynamics in tight focusing conditions	114
6.6	Conclusions	116
7	Conclusions and perspectives	117
7.1	Conclusions	117
7.2	Future perspectives	119
A	Image treatment: Abel inverse transformation	121
	Bibliography	125
B	Acknowledgements	137
C	Publications	141

Chapter 1

Introduction

Since decade, confinement of light below the order of optical wavelength is a very active area of research and found a substantial importance in many diverse scientific fields including microscopy, trapping and advanced laser material processing [SWJ⁺08, MSGMD10]. Usually localization of light can be achieved through the pulse engineering in time and space and near-field techniques [DA12, FW11, ERH⁺07, WSL⁺08]. Spatial and temporal engineering of ultrafast laser pulses establish novel synergies between light and matter enabling the direct access to the smallest scales. Tailoring of ultrafast lasers determine a better controlled ionization process spatially confining the energy; consequently the material response enable the route to nanoscale material processing [ERH⁺07] by altering the temporal, spatial profiles of the pulse [MZC⁺12]. Equally laser polarization can be a control parameter for directional dependence of self-organized nanostructures on the surface and inside bulk materials [DSS⁺10, RVC08, KS08]. So it is obvious that qualitative phenomenal features of the interaction can be expected from the employment of beams with angularly and spatially localized optical fields including supercollimated and needle-like optical fields [WSL⁺08, BDG12], where the propagation remains quasi-nondiffracting in the spatial and temporal domain. Interaction of hollow shaped optical fields with dielectrics is also a perspective [HSKR10]. Extrapolating the concept of the localization of optical fields over a large scale in the perspectives of interaction with the bulk transparent materials leads to a potential advantage towards optical functions and 3D photonics [GM08, NWBT03, SSV⁺10].

Material processing of transparent materials using ultrafast lasers found a paramount importance because of the possibility of localization of laser energy inside the bulk material well below the diffraction limit by means of nonlinear interaction mechanisms and also due to the faster energy transfer to the lattice. These unique features of the ultrafast laser interaction

with transparent materials offer an attractive potential for controlling laser-induced refractive index changes inside the bulk material, a key in defining novel optical function. Based on this fact, a large variety of applications has been proposed in diverse research areas including light guiding [DMSH96], Bragg gratings, [WKNW13], embedded lasers [MDA⁺08], transportation of quantum information [SSV⁺10, CRO⁺11, SSV⁺12], permanent data storage [ZGBK14], astrophotonics [TBLS⁺11] and many other novel integrated photonic applications. Additionally, laser induced low index or void like structures were applied in fabrication of 3-D micro and nanofluidic devices [CSM04, SHM10, LCL⁺13, SC14]. For studying the fundamental nonlinear mechanisms, fused silica is a model material [SCF⁺02] as it shows structural matrix reorganization, fast carrier dynamics and a range of index variation from positive index structures to void-like domains or nanoscale self-organization. This response and its particular (anomalous) thermodynamic behavior encouraged in using dynamic probing techniques to interrogate material behavior. The dynamic material response along with nonlinear propagation provides indications on controlling energy deposition.

Controlling the laser induced refractive index at sub-micron scales is important for future novel 3-D photonic device applications. New paradigms of the nano interaction are posed in novel developments of nanophotonics and nanofluidics. In this respect, material processing using Gaussian laser beams is limited to the longitudinal dimension of the damage due to their spatio-temporal distortions during the propagation in transparent media which prevents the fine control over laser energy deposition. Many of the above mentioned applications require the control of laser-induced refractive index with high aspect-ratios. Furthermore, they require scanning and high number of laser pulses to achieve the high aspect-ratio structures. The challenge of obtaining long structures using Gaussian beams implies translation of the sample around the focal volume in a desired direction. These methods can produce long structures on the expense of processing time and they are accompanied by the non-uniformities in structural modification. In this aspect, non-diffractive beams offer a certain advantages.

Among the other non-diffractive beams, vortex or hollow core beams (higher order Bessel beams) [AD00], Mathieu beams [GVICR⁺01], accelerating Airy beams [SBDC07]; zeroth-order Bessel beams are most widely used because of their invariant transverse profile while propagation although spatial range of experimentally generated beams is limited by finite aperture of the laser beams. Due to high symmetrical energy distribution over an appreciable distance, the ultrafast Bessel beams provide a potentially new interaction regime compared to the Gaussian laser beams. Recently, non-diffractive zeroth-order ultrafast Bessel beams were proposed to show

potential for a complementary range of applications such as deep-drilling, waveguiding, efficient Bragg grating, high aspect ratio structuring [ASF03, DBB⁺13, MJM⁺01, MKŠ⁺13, BCL⁺10a, BCL⁺10b, BVC⁺14]. Also, nonlinear interaction of zeroth-order Bessel beams in various transparent media is equally addressed [PPF⁺04, PFC⁺08].

The main objective of this thesis is to achieve the control of laser induced refractive index at sub-micron level with high aspect-ratios using ultrafast zeroth-order Bessel beams while unravel new features of the interaction mechanisms. Particularly, the capability of achieving the nanoscale is of interest. The control is based on a comprehensive view of the processes including their dynamics and understanding of the physical mechanisms associated with carrier excitation and relaxation provide thus key factor for the better control and increased precision over the laser induced modification. In this frame, we studied the underlying fundamental mechanisms in non-diffractive interaction regime which are leading to the high aspect-ratio structures. Equally we developed a numerical model to understand nonlinear interaction of non-diffractive zeroth-order Bessel beams with transparent media. Specifically, this peculiar interaction results in either increased refractive index or low density sub-micron structures with high aspect ratios, by choosing the proper laser parameters at same focusing conditions. We explored the role of focusing conditions i.e., role of conical half angle of the Bessel beam inside the material on material modification. As moderate focusing conditions offer the stable interaction regime over a wide range of laser parameters compare to other focusing conditions, we studied in detail thus stable interaction regimes exploring self-limiting character of the carriers. We explore the role of dispersion and pulse duration in determining material responses varying from compaction to rarefaction. Remarkably, the accuracy of processing is well below the diffraction limit, achieving the scales down to 100 nm. In order to understand the carrier excitation and relaxation dynamics experimentally, we developed the time-resolved microscopy with sub-picosecond temporal resolution and sub-micron spatial resolution in optical amplitude and phase contrast. We suggest factors concerning to the remarkable energy confinement and suggest ways for material transformation. This thesis is organized as follows:

The following chapter 2 presents the theoretical background of fundamental mechanisms associated with the laser-material interaction in ultrafast regime, particularly the primary excitation and relaxation mechanisms. As this thesis deals with the material processing using zeroth-order Bessel beams, we give an overview on possible generation techniques of zeroth-order Bessel beams. We also discuss the nonlinear interaction mechanisms with transparent media in non-diffracting regimes and present a numerical model

that is employed for simulation results.

Chapter 3 gives the technical background of the experiments that we used for the thesis. We indicate experimental setups that we employed for generation of zeroth order Bessel beams, sub-micron structuring and time-resolved microscopy. Also, we discuss the post characterization techniques of the fabricated sub-micron structures.

Chapter 4 presents the fabrication of high aspect ratio sub-micron structures using single shot ultrafast laser Bessel beams. It mainly outlines the role of Bessel cone angle (focusing conditions), laser parameters such as laser pulse duration and energy on the material modification and stability of the interaction. We identified a span of laser parameters over which the interaction is stable in moderate focusing conditions with sections below diffraction limit. In order to understand the different regimes of the interaction, a numerical model based on nonlinear propagating Schrödinger equation with considering all the major nonlinear effects is applied to understand the nonlinear interaction of intense ultrafast zeroth-order Bessel beams with transparent materials.

Chapter 5 is focused on the role of instantaneous Bessel excitation in terms of the transmission, free carrier generation and plasma luminescence related to the material modification with respect to the laser parameters, using instantaneous pump-probe microscopy. It describes the carrier gas in the frame of Drude formalism.

Chapter 6 describes the dynamics and formation mechanisms of the high aspect ratio structures using time-resolved pump-probe microscopy. Particularly, dynamics is analyzed in terms of free carrier absorption and carrier density evolution via amplitude and phase contrast but we equally indicate activity at the level of the silica glass matrix. Based on the time-resolved results and with additional supporting information from simulations and static photoluminescence studies, we formulate potential formation mechanisms of high aspect ratio sub-micron structures such as uniform increased refractive index and low index or uniform void structures.

Finally, in chapter 7, we summarize the major contributions for the fabrication of high aspect ratio structures and their fundamental aspects of the interaction. Also we briefly comment on future scope and perspectives of this presented work.

Chapter 2

Theoretical background

This chapter describes the theoretical background concerning the presented work in this thesis. First it gives briefly the fundamental mechanisms associated with laser-matter interaction in ultrafast regimes such as primary excitation and relaxation mechanisms. Since our work is mainly focused on material processing using spatially engineered ultrafast beams (zeroth-order Bessel beams), we give an overview of zeroth-order Bessel beams including possible generation techniques. Then we discuss the nonlinear interaction mechanisms with transparent media in non-diffracting regimes. Also we present a numerical model employed to simulate the nonlinear interaction using ultrafast Bessel beams by considering the major nonlinear effects.

2.1 Fundamental aspects of laser-matter interaction

Focused ultrafast lasers can readily produce high peak powers ($\geq 10 \text{ TW/cm}^2$). This feature defines the distinctive aspect of the material interaction, particularly with transparent materials by resulting in a strong nonlinear absorption. The nonlinear nature of the absorption allows the deposition of large amount of optical energy on confined sub-micron or micron scales during the time much shorter than the time required for the thermalization of energy. This unique advantage favours the femtosecond (fs) laser processing of transparent materials over lithography and other photonic fabrication techniques as it gives access to three dimensions.

The laser induced optical breakdown occurs in transparent materials by ionization of a large number of electrons that in turn transfers the energy to the lattice. As a result, material undergoes structural modifications which results from the excitation followed by several relaxation process depending

on material and laser pulse characteristics. The subsequent processes that are involved before attaining the structural equilibrium after the fs laser exposure determine to a large extent the type of permanent refractive index or material modifications. For instance, possible ultrafast laser induced processes particularly in fused silica at subsequent stages with respect to the occurrence moment on the temporal scale are shown in Fig. 2.1. Primary excitation and relaxation mechanisms are discussed in the following.

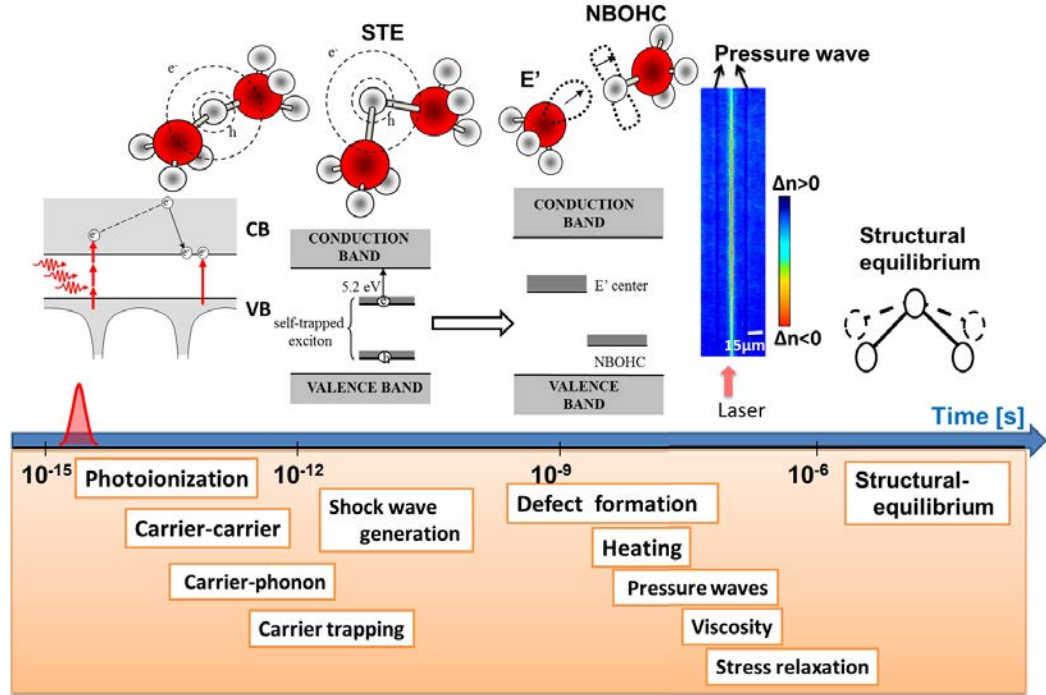


Figure 2.1: Various subsequent excitation and relaxation processes potentially involved in laser material modification particularly in fused silica with respect to their characteristic time scales after the femtosecond laser exposure.

2.1.1 Nonlinear excitation mechanisms

When the intense fs laser pulse interacts with the dielectric material, the optical energy is transferred to material determining the so called optical breakdown via an absorption runaway by promoting the electrons from valence band to conduction band via nonlinear excitation processes such as multiphoton, tunneling, defect-assisted and avalanche ionization mechanisms depending on laser frequency and intensity.

- **Multiphoton ionization:** Multiphoton ionization occurs due to the simultaneous absorption of multiple photons by a single electron in the valence band resulting in promoting of the valence band electron to the conduction band and leaving a hole in valence band. The transition probability scales as I^n . The number of photons (n) of energy ($\hbar\omega$) needed to promote the electrons from valence band to conduction band by fulfilling the condition $n\hbar\omega \geq E_{crit}$ with E_{crit} as

$$E_{crit} = E_g + E_{osc} = E_g + \frac{e^2\epsilon_0}{2cn_0m_{opt}\omega^2} \quad (2.1)$$

where E_g is the band gap energy of the material, E_{osc} corresponds to the oscillation energy and m_{opt} is the electron optical mass. This ionization is more effective with the high laser frequencies, below the frequencies required for linear absorption [SBM01].

- **Tunneling ionization:** Upon laser irradiation, the band structure of the dielectric can be distorted due to the presence of an electromagnetic field which suppresses the potential that binds a valence electron and its parent atom. If the laser field is strong enough, band to band transitions can occur whereby a bound electron tunnels out to become a free electron depending on the height of the potential barrier. This ionization is more effective when the strong laser fields and low laser frequencies are used [SBM01].
- **Defect-assisted ionization:** Presence of defect states in the material's bandgap (leading to intermediate energy levels) lower the multiphoton absorption order. These defect levels could be due to the impurities in the dielectrics or point defects.
- **Avalanche ionization:** Avalanche ionization involves the free carrier absorption involving electron acceleration in the laser field and in the presence of scattering centers followed by the impact ionization process. An electron already in the conduction band can sequentially absorb several laser photons until its energy exceeds the band gap energy and this electron can then collisionally ionize another bound electron via impact ionization from valence band resulting in two electrons at the conduction band minimum. This process will repeat as long as the laser field is present, causing the conduction band electron density to increase exponentially. It is important to note here that the avalanche ionization requires some seed electrons to already be in the conduction band of the material. These initial electrons are provided either by

thermally excited carriers, by easily ionized impurity or defect states or by the carriers that are directly generated by multiphoton or tunneling ionization. Also, implicitly the laser heating should be superior to collisional time. The continuity equation for producing free carriers via avalanche ionization reads as:

$$\left(\frac{\partial \rho_e}{\partial t}\right)_{Ava} = \left[\frac{\sigma \rho_e}{\left(1 + \frac{m}{m_e}\right) E_g} |\epsilon|^2 \right] \frac{\rho_a}{\rho_0}. \quad (2.2)$$

where $\rho_a = \rho_0 - \rho_e$ and ρ_0 are the density of neutral and total atoms in the glass matrix respectively. m is the optical mass. The denominator term is justified by momentum and energy conservation leading to a required minimal kinetic energy for the colliding electron [KRVS00].

As we have seen briefly the free carrier excitation mechanisms by nonlinear means in the presence of intense laser fields, in the following we estimate the generated free carrier density and free carrier contribution to the optical constants using the Drude formalism which give the response of the material hosting the free carriers to the optical field.

2.1.2 Drude model: optical properties

As soon as the free carriers are generated in the conduction band, material response to the optical field is changed dynamically. The free carrier contribution to the optical constants (for example, dielectric function) is estimated from the simple classical conductivity model, called the Drude model. This model is widely used to understand the transient optical response or optical properties of the free carrier plasmas, generated in dielectrics by ultra-short laser irradiation [TSTZ⁺06, SFH⁺96, MQG⁺04]. Generally this optical response is given by the complex dielectric function. Equation of motion that is associated with the collisions involving electrons and atoms of a non ideal lattice, i.e., containing lattice defects under an optical electric field $E = E_0 \exp(i\omega t)$ and with the oscillation damping is given by

$$m \frac{d^2 x}{dt^2} + m\gamma \frac{dx}{dt} = eE = eE_0 \exp(i\omega t) \quad (2.3)$$

where e , m are the electronic charge and mass respectively. γ is the damping factor and it is related to Drude damping or scattering time as $\gamma = \frac{1}{\tau}$ with assuming a single relaxation time. The above differential equation 2.3 gives the solution as

$$x = -\frac{eE}{m\omega^2 + im\omega\gamma} \quad (2.4)$$

The polarization is defined as $P = N_e ex$ where ex is the electric dipole moment and N_e is the free electron density. The complex dielectric constant is related to the polarization as

$$\tilde{\epsilon} = 1 + \frac{P}{\epsilon_0 E} \quad (2.5)$$

From the equations 2.4 and 2.5, we can obtain the free electron contribution to the dielectric constant as

$$\tilde{\epsilon} = 1 - \left(\frac{N_e e^2}{m \epsilon_0} \right) \frac{1}{\omega^2 + i \omega \gamma} \quad (2.6)$$

Eqn. 2.6 of complex dielectric constant in terms of τ can be rewritten as:

$$\tilde{\epsilon} = 1 - \left(\frac{N_e}{N_c} \right) \frac{1}{1 + \frac{i}{\omega \tau}} \quad (2.7)$$

where N_c is the critical electron density where the laser interacts resonantly with the plasma ($\text{Re}(\tilde{\epsilon}) = 0$), $N_c = \frac{m \epsilon_0 \omega^2}{e^2}$. The above equation can be separated into real and imaginary parts as:

$$\tilde{\epsilon} = \epsilon_1 + i \epsilon_2 = 1 - \left(\frac{N_e}{N_c} \right) \frac{1}{1 + (\omega \tau)^{-2}} + i \left(\frac{N_e}{N_c} \right) \frac{(\omega \tau)^{-1}}{1 + (\omega \tau)^{-2}} \quad (2.8)$$

Using the above derived complex dielectric function, optical properties of the material such as reflectance, absorbance and transmittance can be estimated. The reflection coefficient (R) for a normal incidence from the Fresnel law can be written as:

$$R = \frac{\sqrt{\epsilon_1^2 + \epsilon_2^2} + 1 - \sqrt{2(\sqrt{\epsilon_1^2 + \epsilon_2^2} + \epsilon_1)}}{\sqrt{\epsilon_1^2 + \epsilon_2^2} + 1 + \sqrt{2(\sqrt{\epsilon_1^2 + \epsilon_2^2} + \epsilon_1)}} = \frac{(n - 1)^2 + k^2}{(n + 1)^2 + k^2} \quad (2.9)$$

The transmittance and absorbance can be evaluated from the extinction coefficient ($k = \sqrt{\frac{1}{2}(\sqrt{\epsilon_1^2 + \epsilon_2^2} - \epsilon_1)}$) and the Beer-Lambert law. The Beer-Lambert law read as:

$$I = I_0 \exp(-\alpha L) \quad (2.10)$$

where α is absorbance, defined as:

$$\alpha = \frac{4\pi k}{\lambda} = -\frac{1}{L} \ln\left(\frac{I}{I_0}\right) \quad (2.11)$$

I is the intensity of the transmitted light, I_0 is the intensity of incident light and L is the thickness over which absorbance is integrated. Transmittance (I/I_0) can be written as

$$T = \exp(-\alpha L) = \exp\left(-\frac{4\pi k L}{\lambda}\right) \quad (2.12)$$

Estimation of free carrier density:

Density of free carriers at different temporal delays will be estimated experimentally from time-resolved optical transmission images based on the relative transmission within several assumptions concerning their collisional and kinetic properties. The following calculations are shown for the carrier density estimation in terms of transmittance. The equation 2.7 for a hosting material of refractive index n_0 can be written in terms of carrier damping time τ and complex refractive index $\tilde{n} = n + ik$ ($\tilde{n} = \sqrt{\epsilon}$) as

$$\tilde{n}^2 = n_0^2 - \left(\frac{N_e}{N_c} \right) \frac{1 - i(\omega\tau)^{-1}}{1 + (\omega\tau)^{-2}} \quad (2.13)$$

Recall again here the complex refractive index $\tilde{n} = n + ik$ and

$$\tilde{n}^2 = n^2 - k^2 + 2ink \quad (2.14)$$

By comparing the equations 2.13 and 2.14 (real and imaginary parts), we obtain an equation of carrier density in terms of transmittance (indirectly k) and normalized to the critical value as:

$$\frac{N_e}{N_c} = -2k^2 (1 + (\omega\tau)^2) \left(1 - \sqrt{1 + (\omega\tau)^{-2} \left[1 + \frac{n_0^2}{k^2} \right]} \right) \quad (2.15)$$

In the above equation, the term $\omega\tau$ defines the plasma damping characteristics. ω is the laser frequency and τ is the carrier momentum scattering time.

2.1.3 Kerr self-focusing and carrier defocusing effects

Intensity dependent refractive index in the presence of third order nonlinearities is expressed as:

$$n = n_0 + n_2 I \quad (2.16)$$

where n_0 is the linear refractive index, I is the intensity of incident light and n_2 is the nonlinear refractive index that characterizes the strength of nonlinearity which is related to the third order nonlinear susceptibility $\chi^{(3)}$ as.

$$n_2 = 3\chi^{(3)} / 2\epsilon_0 c n_0^2 \quad (2.17)$$

One of the processes that can occur due to the intensity dependent refractive index is self-focusing. This process can occur when the high intense laser interacts with transparent materials for which n_2 is positive. Variance in

the spatial profile of the laser intensity lead to the variance in spatial profile of the refractive index with higher refractive index at the center of the beam than on the wings of the spatial intensity profile because of intensity dependent refractive index. This spatial variance in refractive index acts as a positive lens effect that tends to focus the laser beam inside the material. This phenomenon is termed as Kerr self-focusing. Effectively, Kerr-self focusing leads to decrease in the laser pulse diameter and to attaining the high intensities which will lead to the nonlinear photoionization mechanisms. The catastrophic Kerr-self focusing occurs only when power of the laser beam is higher than critical power (P_{cr}) [Boy03, Mar75].

$$P_{cr} = \frac{0.148\lambda^2}{n_0 n_2} \quad (2.18)$$

where λ is the laser wave length.

As photoionization mechanisms generate the free carriers plasma inside the transparent materials, this plasma with a concentration gradient following the laser profile lead to the defocusing effect similar to a negative lens effect. This defocusing effect arises due to the fact that the carrier density is higher at the center than at periphery due to typical laser pulse intensity profile. Presence of high carrier density at the center decreases the refractive index, effectively spatial variance of refractive index act as a negative (diverging) lens which is contrary to the Kerr-self focusing effect.

Balancing between the Kerr-self focusing and plasma defocusing and diffraction processes would lead to the filamentation during the propagation of an intense ultrashort pulse. Here it is to note that Kerr-self focusing and plasma defocusing effects are also still valid for the zeroth-order Bessel beams as their transverse intensity profiles are close to a Gaussian profile.

2.1.4 Relaxation mechanisms

Once the free carriers are generated in the conduction band during the laser exposure, material transformation at later time scales is determined by several transient relaxation processes. In this section we mention the relaxation process which are relevant to our work. Depending on the generated free carrier density and energy deposition or laser pulse characteristics, the following primary relaxation processes can occur in fused silica: free carrier trapping (self-trapped excitons), generation of defect centers and release of shock or pressure waves upon heating in confined conditions.

Formation of self-trapped excitons and defect centers:

Multiphoton absorption in transparent media after the intense laser excitation results in electron transportation from the valence band to the conduction band, leaving a hole in the valence band. An electron and a hole can be bounded together by Coulomb forces, collectively referred as exciton. In materials with a small dielectric constant, the Coulomb interaction between an electron and a hole may be strong and the excitons thus tend to have a small diameter, of the same order as the interatomic distance. These are the so-called Frenkel excitons. In a deformable lattice i.e., with a high polarization of the matrix excitons tend to self-trap equivalent to a mass increase due to the vibrational environment (phonon damping). This leads to charge and energy localization. Since the self-trapped excitons (STEs) are means of channeling electronic excitation, a major source of interest towards them comes from further energy transfer into atomic processes such as network defect formation and refractive index change. The change in refractive index due to the STEs can be expressed according to the Lorentz model [MQG⁺04, KPKK09] as

$$(\Delta n)_{STE} = \sum_k \frac{N_k e^2}{2n_0 \epsilon_0 m_k (\omega_k^2 - \omega^2)} \quad (2.19)$$

where k is the number of localized levels in the direct band gap. N_k is the concentration of electrons trapped at the defect levels. e is the electron charge. n_0 is the refractive index of the unperturbed solid. m_k is the effective mass of the trapped carriers. ω_k is the absorption band of the defect level. ω is the radiation frequency. Mostly carriers trapping lead the increase in refractive index change due to their deep-lying levels. Generation of excitons equally leads to the appearance of additional energy levels below the conduction band, that changes the optical properties of the glass. The schematic of energy level diagram is shown in Fig. 2.2 (a).

The theoretical scenario of formation of STEs [Shl88, FHS90] can be understood as: a hole primarily localized on an oxygen and an electron primarily localized on a neighboring silicon. Localization of the hole results in a small atomic displacement of oxygen atom that deepens the potential well where the carrier is situated. This oxygen being displaced substantially from its regular lattice site, distorts the silica network and weakens the Si–O–Si bond (strain in bonds). Further displacement of the oxygen atoms results in the formation of dangling oxygen and silicon bonds, which represent the non-bridging oxygen hole center (NBOHC) and E'- defect centers. The scenario of formation of STEs, strain in bonds and formation of defect centers is depicted in Fig. 2.2 (b).

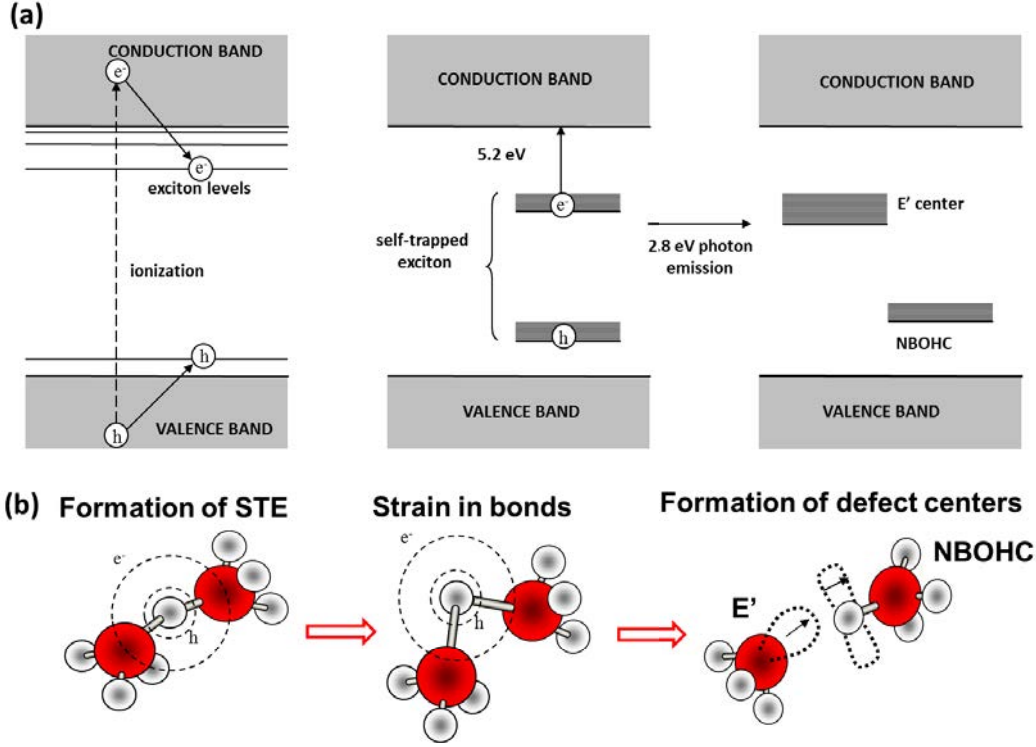


Figure 2.2: (a) Schematic energy level diagram of the self-trapped excitons and related defect centers. (b) Scenario of formation of self-trapped excitons lead to the strain in bonds and defect centers.

Generally free carriers would be trapped after (in the order of) 150 fs of laser excitation [MGD⁺97, SG93]. In our study, we will confirm the formation of STEs and defect centers by time-resolved studies and post irradiated photoluminescence studies.

As we have seen, STE relaxation is the origin for the formation of defect centers (NBOHC and E') in fused silica. It is important to mention that the network reorganization processes in terms of defect centers could be accompanied by the formation of smaller rings. The induced densification is a function of number of breaking bonds which primarily depends on the irradiation source. Such accumulation of breaking bonds leads to change in density or refractive index, particularly densified regions lead to the smooth positive refractive index modifications. Experimentally, densification scenario can be examined by Raman investigation of laser-induced structures [SB02, BBS⁺08, MDV⁺13, Mis12]. The Raman spectra of laser induced positive refractive index region with comparison of pristine sample is shown in Fig. 2.3. The increment of the D_2 band on the modified material evidences

the compaction of a glass matrix via densely packed three-member Si-O rings.

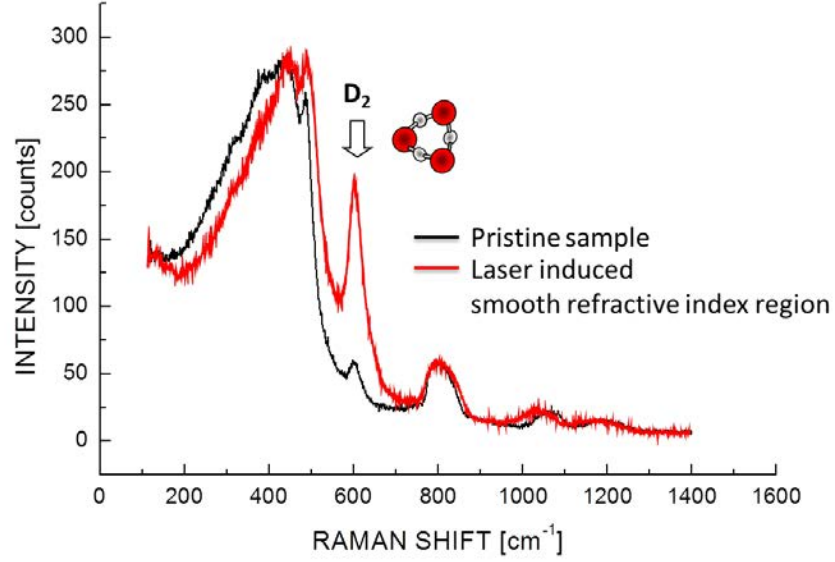


Figure 2.3: Raman spectra of the pristine (black curve) and laser induced refractive region (red curve). The increment of D_2 band related to three membered Si-O rings is highlighted [Mis12].

Release of shock and pressure wave:

This section is an exclusive part of the laser-matter interaction at high intensities or stronger energy deposition confined in a solid. The interaction of a laser with matter above the ionization threshold leads in the first few fs of the laser pulse duration to free carriers generated in and around the focal volume that increases the absorption of energy density over sub-focal volume via nonlinear process. This ensures a fast energy transfer in a very small focal volume. A shock wave is generated in the interaction regime and it propagates into the surrounding cold material. Also, we can understand the generation of the shock wave in other way. The hydrodynamic motion starts after the electrons have transferred their energy to ions. The pressure in a range of TPa builds up, considerably exceeds the Young modulus in most of the materials after the electron-ion energy equilibration. For example the Young modulus for fused silica is ~ 72 GPa [Gam11]. The high pressure generates the shock wave, which propagates from the energy absorption region to surrounding cold media. The shock wave propagation is accompanied by

compression of solid material at the shock wave front and rarefaction behind it, leading to a formation of void inside the material.

Here, it is important to note that the propagating shock wave in a cold material loses its energy due to dissipation, for example due to the work performed against the internal pressure (Young modulus) of the cold material which resists the material compression. The propagation distance at which the shock effectively stops defines the shock wave-affected area. The shock wave converts into an elastic (sound wave) or a pressure wave at the stopping point. The elastic wave propagates further into the material without inducing any permanent changes in the solid. Shock effected region is around 200-500 nm away from the focal volume and depends on the deposited energy [JNT⁺06, JMH⁺06].

2.2 Zeroth-order Bessel beams

First noted by Durin, the non-diffracting (i.e., propagation invariant) beams [DMJE87] retain their intensity during their propagation in free space. Zeroth-order Bessel beams are a special class of non-diffracting beams whose radial profile can be described by a zero-order Bessel function of the first kind. Zeroth order Bessel beams have the unique property that they possess a narrow bright central region surrounded by a series of concentric rings and the central core does not diffract over an appreciable distance. Because of this unique nature, zeroth order Bessel beams have found lot of interest in various fundamental and applied research fields such as 3-D optical tweezers [GCMM⁺02], electron acceleration [LGTL04], higher harmonic generation [ABDL⁺03], continuous plasma channels [FPA⁺00] and microlithography [EHS⁺97]. Sub-micron channel fabrication in transparent materials using Bessel beams was also reported [BCL⁺10b]. In this thesis, we focus on high aspect ratio structures fabrication and their formation dynamics using zeroth order Bessel beams, illuminating aspects of light-matter interaction in novel regimes. Therefore, the following sections are dedicated to give the basic concepts and generation techniques of the zeroth order Bessel beams. We equally discuss the nonlinear interaction with transparent media (mainly fused silica). We present a theoretical model that is developed to understand the phenomena related to intense Bessel core interaction.

2.2.1 Basic concepts and generation techniques of Bessel beams

Electric field distribution of the Bessel beams that can be expressed as follows:

$$E(r, \phi, z) = A_0 J_n(k_r r) \exp(ik_z z) \exp(\pm in\phi) \quad (2.20)$$

where r , ϕ and z are the radial, azimuthal and longitudinal components respectively. A_0 is the amplitude of the electric field, J_n is the n^{th} order Bessel function. k_r (k_\perp) and k_z (k_\parallel) are radial and longitudinal wave vectors respectively that are related to the wave vector is as $k = \sqrt{k_r^2 + k_z^2}$.

For the zeroth-order Bessel beams i.e. $n = 0$, the electric field of zeroth order Bessel function of the first kind (J_0) becomes

$$E(r, \phi, z) = A_0 J_0(k_r r) \exp(ik_z z) \quad (2.21)$$

As ideal Bessel beams would be of infinite transverse extent and carry infinite amount of energy, they can not be generated experimentally because of the fact that the optical systems have only finite apertures. However, over a limited spatial range under finite approximation, such idealized beam can be obtained experimentally and termed as “quasi non-diffracting beam or quasi Bessel beam”. Important to note that these quasi Bessel beams are just mentioned as “Bessel beams” in this thesis. Experimentally, there are many possible ways to generate the Bessel beams. For instance, Durnin et al.[DMJE87] demonstrated the generation of Bessel beams in 1987 with a circular slit located in the focal plane of a lens as shown in the Fig. 2.4.

The conical half angle of a generated zeroth order Bessel beam in this approach is expressed as

$$\theta = \tan^{-1}(d/2f) \quad (2.22)$$

where d is the diameter of the slit and f is the focal length of the imaging lens. Also geometrically we can estimate the propagation distance as

$$z_{max} = \frac{R}{\tan\theta} \quad (2.23)$$

where R is radius of the lens. Although this generation technique is simple, the amplitude of the generated Bessel beam is modulated by the diffraction envelope of the slit. Also the efficiency of the beam intensity transfer from the illuminating beam to the generation of Bessel beam is very low. This reduction in the available energy is unsuitable for applications where high intensities are needed. Thus, for material processing applications, other

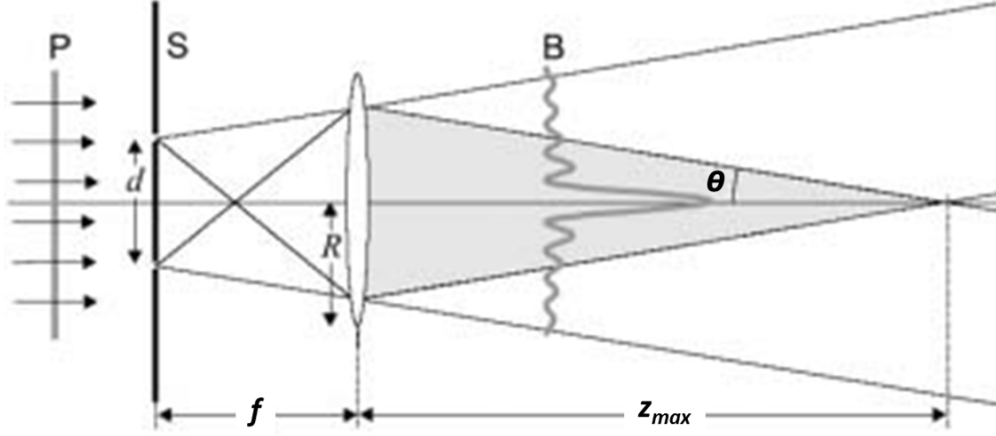


Figure 2.4: Generation of a Bessel beam by using an annular slit S with a diameter d placed in the back focal plane of a lens of radius R and focal length f . The Bessel beam is created from a plane wave P . z_{max} is the propagation distance of the generated Bessel beam. This image is taken from [MD05].

methods are generally more desirable. Holograms can generate Bessel beams with higher diffraction efficiency of $\sim 40\%$ [VTF89, TLY] but the axial profile of the intensity is still diffraction modulated.

An ideal axicon or conical lens is a promising option for generating the optically high efficient Bessel beams compared to other previously discussed methods. Axicon based zeroth order Bessel beam generation technique is shown in Fig. 2.5. The idea behind this generation technique is to manipulate the direction of the wave vectors of the incoming beam in such a way that they are distributed on the surface of the cone. When collimated Gaussian laser beams with flat phase front are incident normally on an axicon of refractive index n with the wedge angle α (sometimes referred as base angle), the beams deviate towards the optical axis i.e. along the propagation direction with an angle θ and overlap, resulting into an interference effect which can be characterized as zeroth order Bessel beams of conical half-angle θ . The transverse profile of this experimentally generated Bessel beam using axicon is shown in right side of the Fig. 2.5. The width of the central core is highlighted in the figure which do not diffract with propagation. With pure geometrical optics considerations, Snell's law at the inclined face of an axicon gives rise to the following expression:

$$\theta = \sin^{-1}(n \sin \alpha) - \alpha \quad (2.24)$$

The Bessel beam propagation distance z_{max} (non-diffracting zone) can

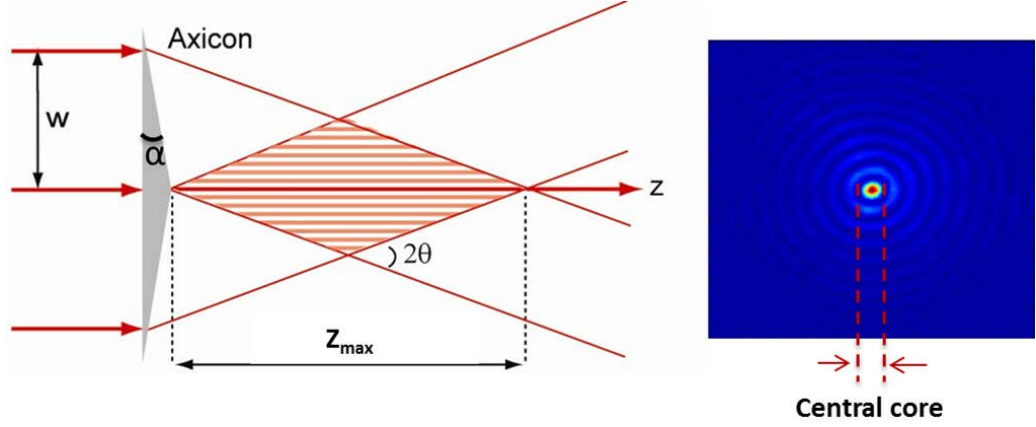


Figure 2.5: Generation of a Bessel beam using an Axicon lens illuminated with a Gaussian beam of waist w . α is the base angle of the axicon and θ is the conical half-angle of the generated Bessel beam. Experimentally generated transverse profile of the zeroth order Bessel beam using Axicon is shown in right.

be expressed as follows:

$$z_{max} = \frac{w}{\tan \theta} \quad (2.25)$$

where w is the beam waist of the incident Gaussian beams. Note here that, in Durnin's approach, finite-aperture effect and plane wave illumination cause modulations in the on-axis intensity of zeroth order Bessel beams. This kind of modulation was also observed in the case of axicon when illuminated with plane waves. Interestingly, illuminating Gaussian beams on an axicon removes the on-axis intensity oscillations and provides a smooth longitudinal intensity variation. The kind of Bessel beams thus generated are known as Bessel-Gauss beams which can be characterized as finite-size, zeroth-order Bessel beams. The length of the non-diffracting zone is limited, although much longer (nearly more than 10 times) than that of the Rayleigh length of Gaussian beams of similar size. The longitudinal profile can be flexibly design by further apodization. The on-axis intensity $I(z)$ of Bessel-Gauss beams produced at a distance z from an axicon tip is expressed as [JPS00]:

$$I(z) = \frac{8\pi P_0 z \sin^2 \theta}{\lambda_0 \omega_0^2} \exp \left[-2 \left(\frac{z \sin \theta}{\omega_0} \right)^2 \right] \quad (2.26)$$

where P_0 is the peak power of the incident laser beam on axicon. θ is the conical half-angle of the generated Bessel-Gauss beam. λ_0 and ω_0 are the wavelength and beam waist of the incident Gaussian beam respectively. Here, it

is important to mention that the nondiffracting length and conical half-angle of Bessel beams are affected by a factor n upon propagation in a medium of refractive index n .

Also in several cases, spatial light modulators (SLMs) were exploited that are capable of mimicking most optical elements (including axicons of any kind) and were adopted widely in the generation of Bessel beams [DCC96a, DCC96b, CRC⁺03]. SLM offers a flexible operation i.e., particularly changing of the conical angle of Bessel beam is straightforward. Although SLM has its unique advantages, we used the axicon to generate the zeroth order Bessel beams. To modulate the size of the beam further, a telescope arrangement [VP03] can be used. This consists in a setup where an axicon is placed before the two fixed lenses (telescopic arrangement) and offers the variation of cone angles. The use of axicon is an efficient way to produce Bessel beams except for the critical optical alignment (off-axis illumination could lead to the aberration in generated beam). We have taken a special care for alignment to avoid the oblique and off axis illumination and spatially filtered the leakage of Gaussian components from an axicon tip which will be discussed clearly in experimental section 3.2.1. Finally few notable properties of the Bessel beams are mentioned below.

- The Bessel beams are generated through the interference of convergent beams when a collimated Gaussian beam transits a cone-shaped lens (axicon).
- The central spot diameter of the Bessel beam is determined by the axicon base angle (θ) and can be of the order of the optical wavelength. The size of the central core at full width half maximum is defined as $2.25/k \sin \theta$. Non-diffracting length is determined by the input beam size and the axicon base angle.
- Remarkable property of Bessel beams is the ability of the central ray to self-reconstruct its profile when disturbed by an obstacle [BWC98].

2.2.2 Nonlinear interaction of Bessel beams

The characteristic property of the zeroth-order Bessel beams is the existence of an intense central core within the beam profile. The linear propagation of the Bessel beams in a medium is well understood [BWC98] and discussed in previous sections. This section is focused on the nonlinear propagation characteristics of the zeroth order Bessel beams. The narrow and strongly peaked intensity distribution over relatively long distance and the composition of many plane waves with a fixed single valued radial wave vector

of Bessel beams exhibit unusual characteristics while interacting nonlinearly with matter. Besides, the cone angle of Bessel beams provides an additional tunable parameter for non-collinear interaction.

When the intense ultrashort Bessel beam propagates through transparent material, nonlinear effects occur mainly within the intense central core of the Bessel beam. The annular region will propagate linearly toward the axis and will suffer nonlinear effects only when it crosses the central core region. There are three different nonlinear interaction regimes of the Bessel beams that have been noticed in transparent media [PFC⁺08].

- Weakly nonlinear Bessel filamentation regime: It is obtained by slightly increasing the power of the input Gaussian beam up to the point where the power in the core is sufficient to induce self-focusing but insufficient to induce the collapse or significant multiphoton ionization [RKMW07].
- Unsteady Bessel filamentation regime: It is obtained when the power in the central portion is sufficient to induce collapse, multiphoton ionization and hence the damage [GVJ⁺06].
- Steady Bessel filamentation: It is obtained when the nonlinear sample is in contact with the axicon, the Gaussian beam smoothly reshapes into a nonlinear unbalanced Bessel beam [PPF⁺04, PCF⁺07]. But if the Gaussian beam propagates through the axicon and reshapes into a Bessel beam before entering the nonlinear sample, strong self-focusing of the central peak of the Bessel beam occurs which in turn triggers multiphoton absorption. Eventually it induces a fast reduction of the peak intensity and the process can occur again while Kerr self-focusing of the external ring periodically brings energy to the core. This would results in unsteady filamentation. The transition from the unsteady Bessel filamentation to steady filamentation can be made possible by increasing the base angle of the axicon [PFC⁺08].

In the following, we qualitatively describe the nonlinear interaction of a Bessel beam with a model transparent material.

Numerical model for the nonlinear interaction of Bessel beams in transparent media:

Several insight phenomena of intense Bessel beam interaction with the transparent dielectrics (e.g. fused silica) are understood using numerical simulations. A model is developed by solving the nonlinear optical Schrödinger equation with additional terms [Gae00, CSF⁺05, BBS⁺07] related to the

excitation. The model is taking into account major nonlinear effects that affect the pulse propagation such as Kerr self-focusing, plasma defocusing, inverse bremsstrahlung, carrier generation via multiphoton ionization (MPI), and avalanche ionization. A proper account of these phenomena help us to figure out the local spatial energy deposition profiles. The extent of the material alteration is linked to the spatial energy distribution and is driven by the delicate balance between focusing and defocusing, accompanied by spatio-temporal pulse distortions. The model applies optimally for moderate energies because of the numerical complexity generated by strong gradients of the excitation at high input energies. Also the paraxial approximation is still being valid within considered energies (until moderate energies). We like to mention that our numerical procedure is based on the split-step Fourier method to calculate iteratively the beam propagation.

Following the formalism in [PFC⁺08], the input linearly polarized Gaussian pulse with cylindrical symmetry passing through an axicon is described by the complex electric field envelope as

$$\epsilon(r, t, 0) = \epsilon_0 \exp \left(-\frac{r^2}{w_0^2} - \frac{t^2}{t_p^2} - ik_0 r \sin \theta \right) \quad (2.27)$$

The input Gaussian pulse $\epsilon(r, t, 0)$ generates a zeroth order pulsed Bessel beam after linear propagation over a distance (passage through the axicon) $z_{ax} = w_0/\tan \theta$ as

$$\epsilon(r, t, z_{ax}) \propto J_0(k_0 r \sin \theta) \quad (2.28)$$

where $k_0 = \omega_0 n(\omega_0)/c$ and w_0 are the wave vector and beam waist of the incident Gaussian pulse. θ is the Bessel conical half angle. The electric field envelope is assumed to be slowly varying in time. It evolves along the propagation axis z according to the nonlinear envelope equation that is taking into account of major nonlinear effects expressed in a moving reference frame as

$$\begin{aligned} \frac{\partial \epsilon}{\partial z} = & \frac{i}{2k_0} T^{-1} \left(\frac{\partial^2}{\partial r^2} + \frac{1}{r} \frac{\partial}{\partial r} \right) \epsilon - \frac{ik''}{2} \frac{\partial^2 \epsilon}{\partial t^2} \\ & + \frac{ik_0 n_2 T}{n_0} \left[(1 - f_R) |\epsilon|^2 + f_R \int_{-\infty}^t R(t - \tau) |\epsilon|^2 d\tau \right] \epsilon \\ & - \frac{\sigma}{2} (1 + i\omega_0 \tau_c) T^{-1} (\rho_e \epsilon) - \frac{1}{2} \frac{W_{PI}(|\epsilon|) E_g}{|\epsilon|^2} \epsilon. \end{aligned} \quad (2.29)$$

The first term in the above equation belongs to the diffraction in transverse plane. Second term is for the group velocity dispersion ($k'' = \frac{\partial^2 k}{\partial \omega^2}$, $k = k(\omega) = n(\omega)\omega/c$ is a frequency dependent wave number) that describes

the dispersive properties of the medium which is necessary to obtain the correct temporal and spatial evolution of the laser pulse. The third term describes the optical Kerr effect and self-steepening with a term corresponding to the delayed Raman-Kerr optical response of the nonlinear material and characterized by the parameter f_R [CSF⁺05]. n_2 is the nonlinear refractive index of fused silica. The operator $T=1+(i/\omega_0)(\partial/\partial t)$ accounts for self-steepening effects and space-time coupling. The fourth term represents the plasma defocusing mainly characterized by the damping factor $\omega_0\tau_c$. σ is the free carrier absorption by inverse bremsstrahlung described by the Drude formalism as

$$\sigma = \frac{k_0 e^2 \omega_0 \tau_c}{n_0^2 \omega_0^2 \epsilon_0 m_e (1 + \omega^2 \tau_c^2)}. \quad (2.30)$$

where τ_c is the electronic momentum scattering time. The last term in the Eqn. 2.29 denotes the energy absorption due to the photoionization but disregards energy loss mechanisms to the lattice. $E_g = E_{g0} + e^2 \epsilon^2 / 2 c n_0 \epsilon_0 m \omega_0^2$ is the effective ionization potential that accounts for the oscillating behavior of the free electrons at the bottom of the conduction band [Ret04] and E_{g0} is the intrinsic energy gap.

Here important comments must be made on physical parameters that affect the nonlinear interaction and they are as follows:

- In fs-laser excited wide band-gap materials, multiphoton ionization (MPI) is one of the major processes to generate seed electrons for further multiplication mechanisms in the conduction band. It is expectable that the free carrier effective and optical mass depends on electron density, energy and temperature [Dri84, YB86]. Ideally, this variance in optical mass derives from nonparabolic bands. In addition distortions in band structure or change in bandgap affect the MPI. In other words, MPI is dependent on bandgap and carrier effective mass. The above discussion imposes a serious caution to choose a fixed value of an optical mass.
- Plasma defocusing is also one of the crucial mechanisms to arrest the catastrophic collapse. The efficiency of the plasma defocusing is defined by the damping factor $\omega_0\tau_c$. Drude damping time is also density, energy and temperature dependent [Ser89, CC87] and implies the same restriction for choosing a constant value of scattering time.

As optical mass and carrier damping time of free carriers are expectably a function of carrier density and temperature, defining and choosing appropriate values is ongoing debate and purely depends on excitation conditions. However, in our model, we consider these parameters to be constant and they

will be chosen to match experimental observations. Drude damping time is estimated experimentally from the instantaneous transmission and is found nearly constant over a considered range of energies. The effect of the dielectric response to the electronic population is not considered to influence the absorption cross section, an assumption which remains valid for moderate electronic densities. The equation for the free-electron density reads as

$$\frac{\partial \rho_e}{\partial t} = \left[W_{PI}(|\epsilon|) + \frac{\sigma \rho_e}{\left(1 + \frac{m}{m_e}\right) E_g} |\epsilon|^2 \right] \frac{\rho_a}{\rho_0} - \frac{\rho_e}{\tau_{tr}}. \quad (2.31)$$

$\rho_a = \rho_0 - \rho_e$ and ρ_0 are the density of neutral and total atoms in the glass matrix respectively. Equation 2.31 describes free electron generation due to photoionization (W_{PI}), defined according to Keldysh formulation [CSF⁺05], avalanche ionization (with an avalanche coefficient simply expressed as $\frac{\sigma}{(E_g)_{corr}}$; $(E_g)_{corr} = \left(1 + \frac{m}{m_e}\right) E_g$, $\frac{m}{m_e}$ is a correction derived from momentum and energy conservation rules [KRVS00]), and free-electron decay in self-induced lattice deformations with a characteristic trapping time $\tau_{tr} = 150$ fs [ADDS⁺94]. Electronic transport is considered to be negligible on the time scale of irradiation. The results with this numerical modeling will be discussed in chapter 4.

2.3 Conclusions

In conclusion, we presented a fundamental description of main nonlinear excitation and relaxation processes in non-diffractive interaction case in the context of presented work. In first section, we have given an overview of the fundamental aspects of laser-matter interaction. Particularly, we mentioned the laser induced physical processes such as primary excitation and relaxation mechanisms. In the later section, we have given an overview of zeroth-order Bessel beams and possible generation techniques. Also we presented the nonlinear interaction of zeroth-order Bessel beams with transparent materials via a numerical model with considering the major nonlinear effects.

Chapter 3

Experimental details

This chapter gives the background and the technical description of the experiments that are employed for the thesis. First part of this chapter is devoted to give a brief idea about the femtosecond laser system which is used for the presented experimental results. Next part of this chapter describes the experimental setups that are used for the generation of zeroth-order Bessel beams using axicon, sub-micron structuring characterization and time-resolved imaging with sub-picosecond temporal resolution. The time-resolved imaging arrangement has dual functions: time resolved microscopy which can be operated either in optical transmission or phase contrast modes and time-resolved spectral imaging. As we used the microscope in optical transmission and phase-contrast mode for capturing the spatial distribution of the refractive index profiles of fabricated structures and time-resolved imaging, we discuss briefly the working principle of optical transmission and phase contrast microscope. Scattering or diffusion effects of the probe beam over small structures on experimentally measured transmission are discussed using FDTD simulations. Post characterization techniques of the fabricated sub-micron structures are also discussed.

3.1 Laser system

A regenerative amplifier Ti:Sapphire laser (Coherent) having 60 fs fundamental pulse duration at the central wavelength of 800 nm and at 1 kHz repetition rate is employed for this work. The first part of the laser system is the oscillator (Mantis) which produces the fs laser pulses of low energy. The pulses are then amplified by a regenerative amplifier (Legend Elite) with the principle of Chirped Pulse Amplification (CPA). The block diagram of the laser describing various stages is shown in Fig. 3.1 and the brief explanation

of each stage is given below.

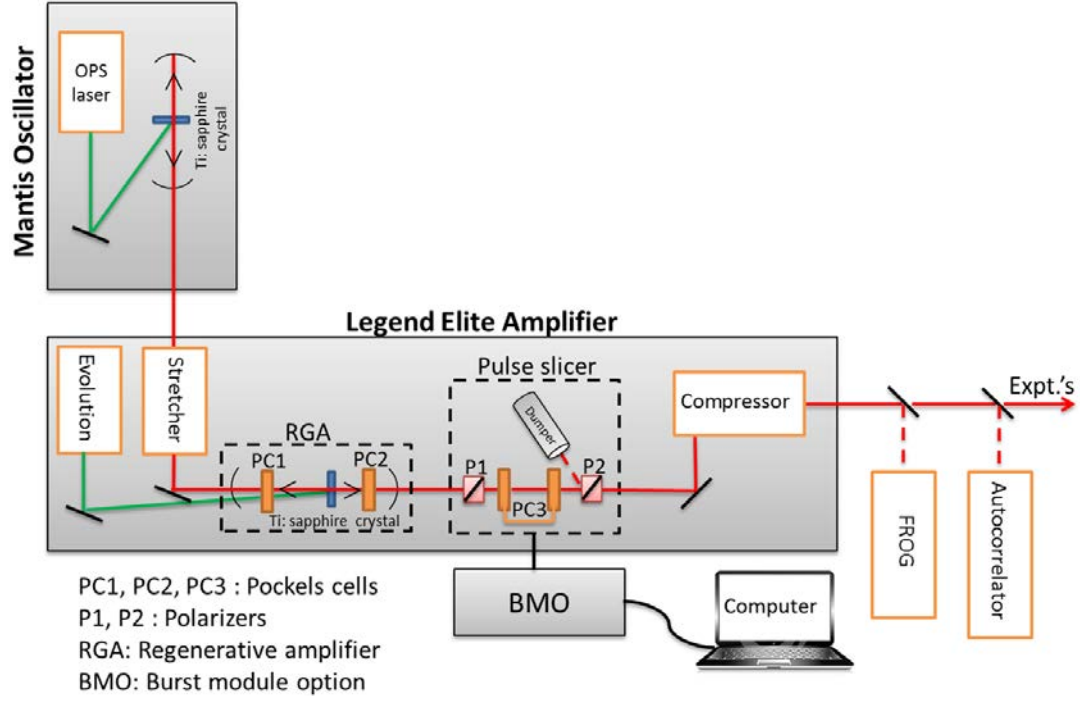


Figure 3.1: Block diagram of the femtosecond laser system

Mantis oscillator is pumped by Optically Pumped Semiconductor (OPS) laser operated at ~ 5 W, 532 nm. The mode-locked oscillator produces ~ 0.5 W output power at a repetition rate of 80 MHz. The output pulses have a bandwidth of 85 nm and a central wavelength of 800 nm. The ultrashort pulse is developed in the cavity by a passive modelocking technique (self adjusting modulator). In order to increase the peak power of the ultrashort pulses, the pulses from the oscillator are seeded into the Legend Elite amplifier system.

The Legend Elite amplifier consists of three parts; the stretcher, amplifier and compressor. The pulse duration is stretched up to 150 ps after passing through a stretcher. Next step is to amplify the stretched laser pulse in the regenerative amplifier (RGA). RGA amplifies the laser pulse to ~ 3 W at 1 kHz repetition rate. The final stage is the compression of the pulse back to fs pulse duration by compressor. Here it is important to note that the compressor gratings are mounted on precision controlled motors such that their position can be changed from outside the cavity in order to optimize the pulse width. The laser pulses can be positively and negatively chirped up to 6 picoseconds (ps) by detuning the compressor. The typical parameters of the laser after the compressor are : average power, 2.7 W, shortest pulse

duration, 60 fs (can be chirped more than 6 ps), repetition rate, 1 kHz and bandwidth, ~ 30 nm.

In order to improve the pulse contrast and control the number of pulses or the repetition rate (1 Hz to 1 KHz), we installed the pulse slicer designed by Coherent. This pulse slicer is controlled by burst module option (BMO) which can offer a selective number of pulses and repetition rate by controlling the pockels cell PC3. The laser pulse characterization was done using FROG GRENOUILLE 8-20 (Swamp Optics) in the fs temporal domain and Pulse Check autocorrelator (APE GmbH, Berlin) in the ps temporal domain. The laser pulse energy is varied using a combination of half-wave plate and polarizer.

3.2 Experimental setup

This section describes the experimental setup that is employed for the presented work and it has following two major functions:

1. Bessel beam generation and sub-micron structuring.
2. Ultrafast time resolved spatial and spectral imaging.

3.2.1 Generation of Bessel beams and sub-micron structuring

We have already discussed the major role of Bessel beams for fabricating the high aspect ratio structures and also various possible generation techniques of Bessel beams in chapter 2. Although there exist several techniques, we used the axicon to generate the zero-order Bessel beams. The generation of Bessel beams and the setup for sub-micron structure fabrication as shown in Fig. 3.2. It depicts the spatial shaping of Gaussian laser pulses emitted from a Ti:Sapphire laser system for the generation of zeroth-order Bessel beams using an axicon lens (apex angle of 179°). The Bessel beams were further imaged into the bulk, 2 mm depth from the entrance surface of a fused silica sample using a telescope composed of a lens (L) and a microscope objective (FO). A controlled demagnification factor is implied. High quality Bessel beams are ensured for our study by using suitable spatial filtering arrangements in the generation setup so that the leakage from the axicon tip, which consists of Gaussian wave vectors, is substantially blocked [BCZ08]. The spatial filter (circular opaque obstacle) is attached to a very thin transparent slide which is placed on the rear focal plane of FO. The spatial filtering arrangement is shown in Fig. 3.2 (marked by the dotted line). Polished parallelepiped fused silica (Corning 7980-5F) samples of dimensions $20 \times 10 \times 3$

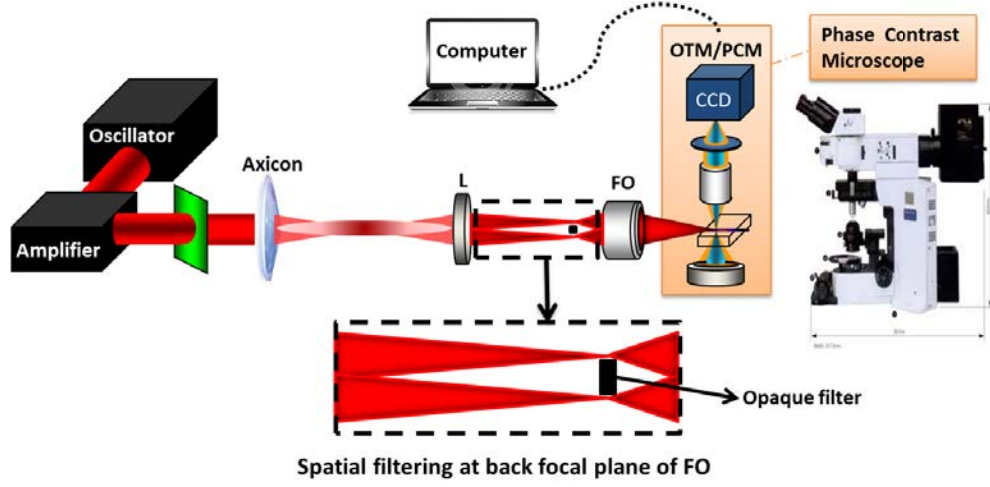


Figure 3.2: Experimental setup of the Bessel beam generation using axicon for sub-micron structure fabrication. In-situ characterization of the fabricated structures can be done using an optical microscope either in phase contrast or optical transmission modes. The leakage from the axicon tip is spatially filtered in the optical path and the arrangement is shown in inset.

mm³ are used for all the experiments described in this thesis. The fabricated structures inside the sample are imaged using Olympus BX-51 microscope assembled as shown in Fig. 3.2. Three dimensional sample movement can be controlled by three translation stages on which sample holder is loaded. Our home built sample holder offers a high quality sample alignment which permits to keep constant the processing depth and the microscopy observing plane during the structuring. The microscope can be operated both in optical transmission and phase contrast mode independently by selecting the appropriate diaphragms before the condenser of the microscope (for phase contrast mode, annular diaphragm is chosen as per the requirement and correction of the collecting objective (PH1/PH2), and no diaphragm is needed for optical transmission). The working principle of the phase contrast microscopy is detailed in the following section 3.3.2.

The experimentally generated Bessel beams are characterized in air by imaging the spatial profiles using a CMOS camera as depicted in Fig. 3.3. In order to image the Bessel beam at our experimental conditions, we have developed a magnifying system which is placed at the focal plane of the Bessel beam. The magnification system consists of a microscope focusing objective (FO2, Mitutoyo 20X, NA=0.42) and a plano-convex lens (L2). The CMOS camera (Thorlabs, DCC 1545C) is placed at the focal plane of the lens L2 having a focal length of 30 cm and camera focus is independent of

the location of focusing objective (FO2). The imaging system is placed on a translation stage to capture the transverse profiles of the Bessel beams at various longitudinal distances.

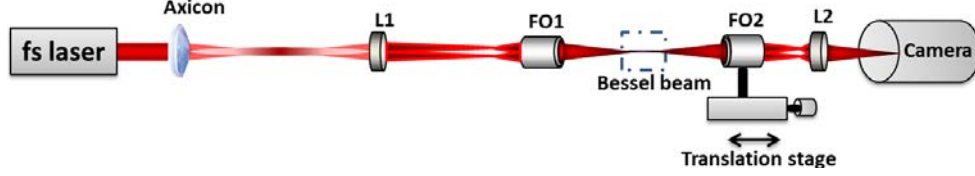


Figure 3.3: Characterization setup of experimentally generated Bessel beams

Geometry of the experimentally generated Bessel beams:

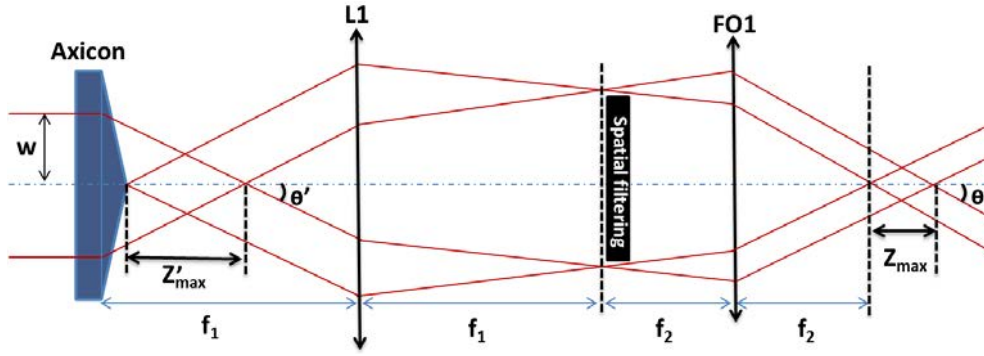


Figure 3.4: Geometry and simplified diagram showing the demagnification of the experimentally generated Bessel beams. w is the beam waist of the incident Gaussian beam (1.3 mm), Z'_{max} and Z_{max} are the non-diffracting propagation distances near the axicon and after the microscopic objective lens (FO1) respectively. θ' and θ are the conical half angles of the Bessel beam near the axicon and after the microscopic objective lens (FO1) respectively.

Fig. 3.4 shows a simplified diagram of the experimental setup used for Bessel beam generation and demagnification; some important parameters are also derived using small-angle approximation. It is observed that for micron size Bessel beams i.e. after demagnification, the important parameters such as conical half-angle θ and the diffraction free propagation distance Z_{max} depend only on the magnifying factor of the telescope. The list of derived Bessel beam parameters using small angle approximation are given in table 3.1.

Parameters	θ'	Z'_{max}	M	θ	Z_{max}
Expression	$\arcsin(n_{ax}\sin\alpha) - \alpha$	$\frac{w}{\tan\theta'}$	$\frac{f_2}{f_1}$	$\arctan(\frac{\tan\theta'}{M})$	$\frac{wM^2}{\tan\theta'}$

Table 3.1: The list of parameters derived from the geometry of the generated Bessel beams in small angle approximation. α is the base angle of the axicon and n_{ax} is the axicon refractive index (1.453). M is the magnification of the telescope.

The spatial characteristics of the experimentally generated Bessel beams are shown in Fig.3.5. The beam profiles are measured in air and obtained parameters are as follows: conical half-angle, $\theta = 12^\circ$, central core FWHM, $r = 1.4 \mu\text{m}$, nondiffracting length FWHM, $Z_{max} = 130 \mu\text{m}$. Here, it is appropriate to note that the nondiffracting length and conical half-angle of Bessel beams are affected by a factor n upon propagation in a medium of refractive index n . Experimentally and analytically (ideal axicon) generated longitudinal profiles are shown in Fig.3.5. If we compare with the longitudinal intensity profile of the ideal axicon generated Bessel beam, modulations in the experimentally generated intensity profile around the leading edge of the beam are due to the leakage of Gaussian components, even though spatial filtering was used to block the leakage from axicon. This has improved the profile but not completely blocked the leakage. Analytically, Bessel beam parameters are estimated as $\theta = 12^\circ$ and $Z_{max} = 131 \mu\text{m}$ for the telescopic conditions $f_1 = 1000 \text{ mm}$ and $f_2 = 20 \text{ mm}$ (same as experimentally generated conditions), which agree well with the experimentally measured parameters.

3.2.2 Ultrafast time resolved imaging

Besides generating the Bessel beams for irradiation purpose, the experimental setup has another important feature, which was employed for the ultrafast imaging of the laser-excited volume in the material. A stroboscopic technique is used. The Bessel beam (acting as pump pulse) excitation of the material was probed at various temporal moments using a part of the incoming laser pulse (acting as probe pulse), illuminating the microscope in diascopy and in synchronization with the pump pulse. The delay between the pump and the probe was set using an optical delay line. Precisely, the laser excitation was performed using a pulse at the central wavelength of 800 nm. Probing was done for most of the presented results with the pulse centered at the wavelength of 400 nm. We equally probed at 800 nm for free carrier damping time estimations where transmission information is needed at two probing

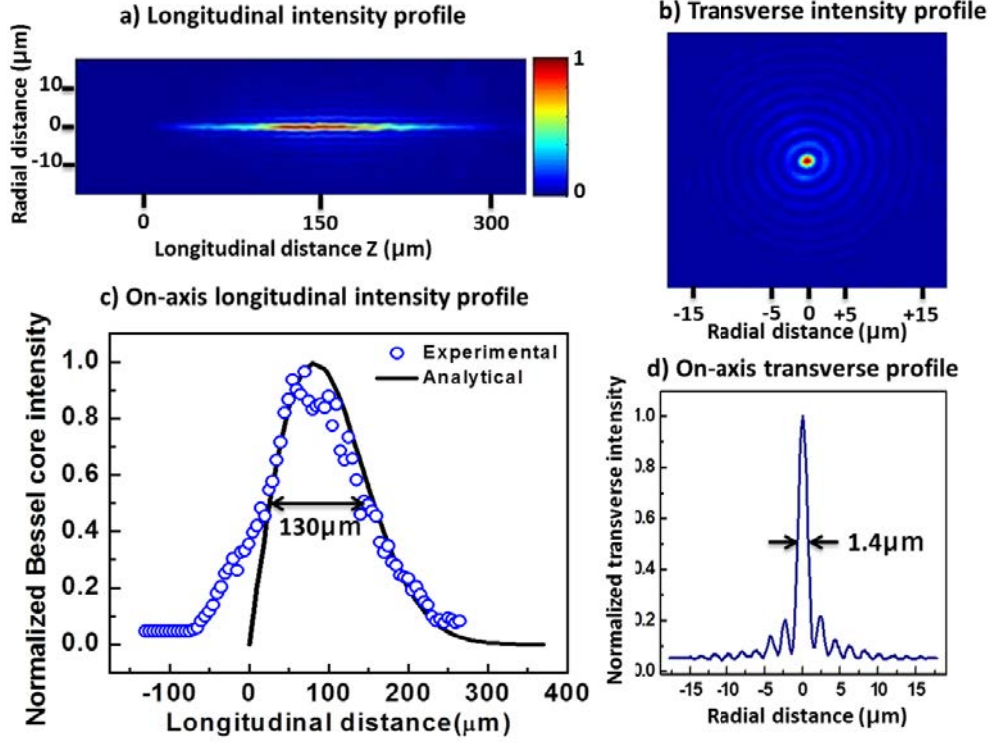


Figure 3.5: Experimentally characterized longitudinal and transverse intensity profiles of the generated zeroth order Bessel beams.

wavelengths. Although the laser system that we used for our study delivers laser pulses of nominal temporal width of 60 fs, their temporal profiles were varied using a compressor as per the requirement of the study to obtain laser pulses both in fs and ps range.

Imaging geometry:

The Bessel beam excited volume of the material was imaged in a perpendicular geometry. The probe, i.e. Gaussian laser pulses, enters the illumination path of the optical microscope which is perpendicular to the Bessel beam propagation axis. An EMCCD (ANDOR iXon Ultra 897 model) camera was used to record the images of the photoexcited region in both optical transmission and phase contrast modes at a finite delay between the pump and the probe pulse. The delay time is defined by the illumination timing. Note here that the optical transmission microscopy (OTM) and phase contrast microscopy (PCM) images represent the spatial mapping of the absorption and phase retardation of the probe pulse by the free-carriers generated by the

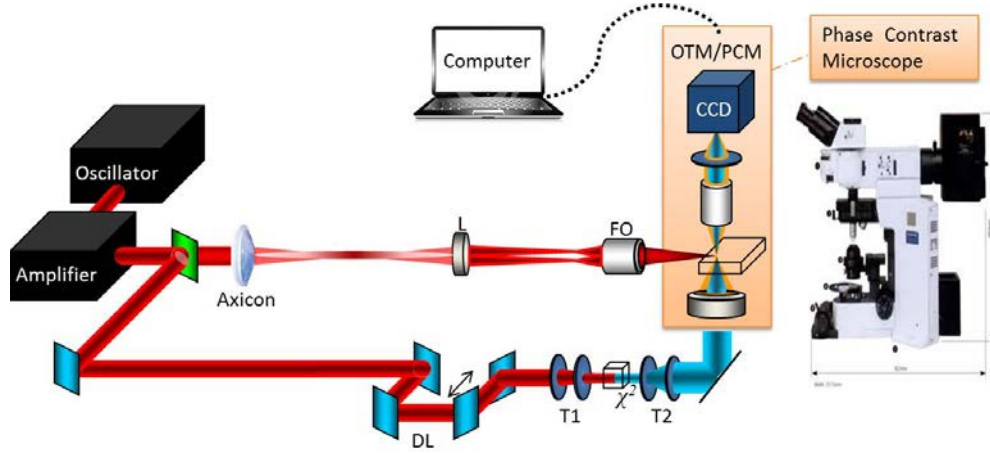


Figure 3.6: Experimental setup of the time resolved ultrafast imaging of the photoexcited volume. Here L is the collimating lens, FO is the focusing objective lens, DL is the variable probe delay line and T1, T2 are the telescopes. A CCD camera is used for image recording. Here we recall that the shown probing path is appropriate for only 400 nm and probing is also done with 800 nm in some cases without having the second harmonic crystal and with the appropriate optics in the probe path.

pump pulse respectively. An additional 10 nm blue bandpass filter was used before the camera to attenuate the parasitic incoherent light emitted by the excited fused silica sample and the scattered pump pulse. The zero-delay between the pump and probe pulse is defined when the pump and probe pulse overlap temporally, maximizing free carrier absorption of the probe pulse. The probe delay can be varied until 6.25 ns by translating the delay stage (PI-511, ~ 300 mm travel range) and adding an extra beam line in between the path of probe line using flipping mirrors. Rotating diffuser plates across the illumination path before the sample were also used to reduce the spatial coherence of the probe pulse, thereby increasing the uniformity of illumination. For better contrast of the image, 60 images were recorded (each one with fresh area of the sample) for a fixed delay between the pump and probe pulse and automatically averaged to obtain a relevant picture. We note here that the limitation in optical resolution and the beam positioning stability will affect the recorded data.

Synchronization:

The synchronization between probe pulse and image acquisition is done using the LabVIEW commands and respective sub-VIs (virtual instruments,

which are developed by the manufacturer to interface the instruments). Our LabVIEW program provides the interface between the laser burst modulator (BMO) (controls the laser shooting) and CCD camera shutter timing (controls the acquisition). The procedure goes on as following. First the command opens the camera shutter and sets ready for the acquisition. The automatic command is given to the BMO to shoot the laser pulse when the camera is ready for the acquisition. Then the probe signal or image is acquired. Here it is important to note that probing experiments were done in dark room environment and the background is subtracted from the acquired data to avoid the background noise during the camera opening and the acquisition. All the probing measurements were done using a single laser pulse similar to that of pump pulse. When the parasitic light of plasma luminescence was observed, the images were corrected for this effect by subtraction.

Resolution:

Experimentally, we estimated the temporal resolution of our time-resolved microscopy setup at sub-ps levels. The temporal duration of the probe pulse in the Bessel excited volume of the sample defines the temporal resolution of the setup. As the probe pulse passes through the major optical components of the microscope like condenser and rotating diffusers before entering the pump (Bessel) excited region, there would be a temporal broadening in the laser pulse duration. This temporal broadening of the pulse mainly due to the above mentioned optical components is estimated using an autocorrelation technique. This temporal broadening is mainly arising because the band width limited ultrashort pulse experiences dispersion when it passes through the optical components. Consequently the initial short pulse broadens in time. One of the major contribution to the pulse broadening in our setup is the condenser lens because of its thickness. If we consider the thick lens effect, there are two kinds of broadening effects that can occur.

- **Propagation time difference effect:** Owing to the difference between the phase and group velocities, the pulse front is delayed with respect to the phase front when light traversing through the thick lens due to its cross section. This delay can be calculated using Fermat's principle [Bor88, Bor89] as

$$\Delta T(r) = \frac{r_0^2 - r^2}{2cf(n-1)} \left(-\lambda \frac{dn}{d\lambda} \right). \quad (3.1)$$

where r and r_0 are the input radii of an arbitrary and the marginal ray respectively. This effect is referred as the propagation time difference effect.

- **Group velocity dispersion:** The dependence of group velocity (v_g) on wavelength, which is called the group velocity dispersion (GVD), causes the broadening of the pulse. The broadening of an unchirped input pulse due to GVD can be calculated as [CL77, Bor88]

$$\Delta T(r) = \frac{\lambda}{c} \frac{d^2 n}{d\lambda^2} L \Delta\lambda. \quad (3.2)$$

where L is the light path length in the lens material.

Experimentally, we measured the laser pulse duration in both optical transmission and phase contrast configurations. In the case of optical transmission, microscope probe beam has to pass through these major optical components leading to a temporal resolution in optical transmission mode of ~ 300 fs for an input laser pulse duration of 60 fs. where as in phase contrast mode i.e., inserting of an annular phase ring in the probe optical path in addition to the optical components, temporal resolution of the setup is improved (~ 200 fs) because of the minimal geometrical distortions as the ring maintains a fixed value of the radius with respect to the axis.

The spatial resolution of the microscope is mainly defined by the microscopic objectives used for the collection of the probe light in addition to the fixed telescopic arrangements or magnification of the microscope. Probing was done mainly using a 20X (NA 0.42) phase contrast Olympus objective. Resolution with this objective yields $0.47 \mu\text{m}$ with a scaling factor of $0.7 \mu\text{m}/\text{pixel}$. To have a precise Bessel excitation volume, in specific cases 100X Olympus (NA 0.9, transmission) objective is used to capture instantaneous plasma absorption as it offers the spatial resolution $\sim 0.25 \mu\text{m}$.

Working principle of the microscopy in optical transmission and phase contrast modes is detailed in following section. Also we recall the microscope offers the integrated information along the illumination path. It delivers thus a projection of the object. We discuss about the image treatment for the correction to the projected captured images with the microscope. After correction, this offers the possibility to retrieve the Bessel radial excitation profiles.

3.3 Working principle of the microscope

This section gives the brief idea about the working principle of the microscope in optical transmission and phase contrast modes. The optical transmission works on the basis of absorption or diffraction of the specimen with respect to surrounding medium which is responsible for contrast in the image whereas

phase contrast microscopy works on the basis of a transparent specimen that has different refractive index than the surrounding medium (different optical path lengths) which after interferential treatment becomes responsible for contrast in image. Detailed principle in each mode is given below.

3.3.1 Optical transmission microscopy

Optical absorption or transmission due to specimen with respect to surrounding medium provides the contrast in optical transmission images. The typical appearance of an absorbing specimen in optical transmission microscopy (OTM) image is a dark shade on a bright background. Typically, the shade contrast depends on the absorbing efficiency of the object. In addition, scattering effects can equally induce a similar effect. For instance, OTM image of an uniform void structures is shown in the Fig. 3.7.

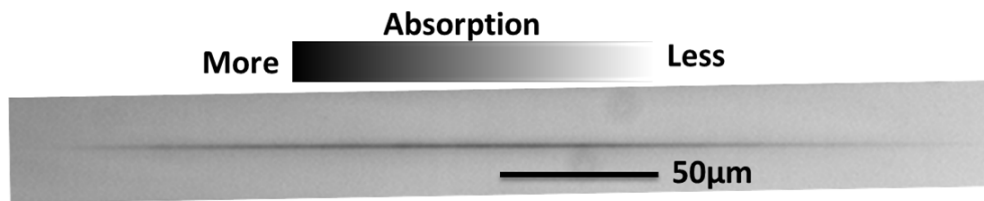


Figure 3.7: Optical transmission image of a uniform void structure.

3.3.2 Phase contrast microscopy

Phase contrast microscopy, first described in 1934 by Frits Zernike [Zer55], is a contrast-enhancing optical technique that can be utilized to produce high-contrast images of transparent specimens. Unstained specimens that do not absorb light are called phase objects because they slightly alter the phase of the light diffracted by the specimen, usually by retarding such light approximately $1/4$ wavelength as compared to the undeviated direct light. These small changes in phase can not be seen by eye but the phase contrast technique employs an optical mechanism to translate minute variations in phase into corresponding changes in amplitude, which can be visualized as differences in image contrast. A schematic illustration of the basic phase contrast microscope configuration is illustrated in Fig. 3.8.

Phase contrast microscopy involves the separation of the direct zeroth order light from the diffracted light at the rear focal plane of the objective. To do this, a ring annulus is placed at the front focal plane of the condenser (under the condenser) in conjugation with the objective rear focal plane.

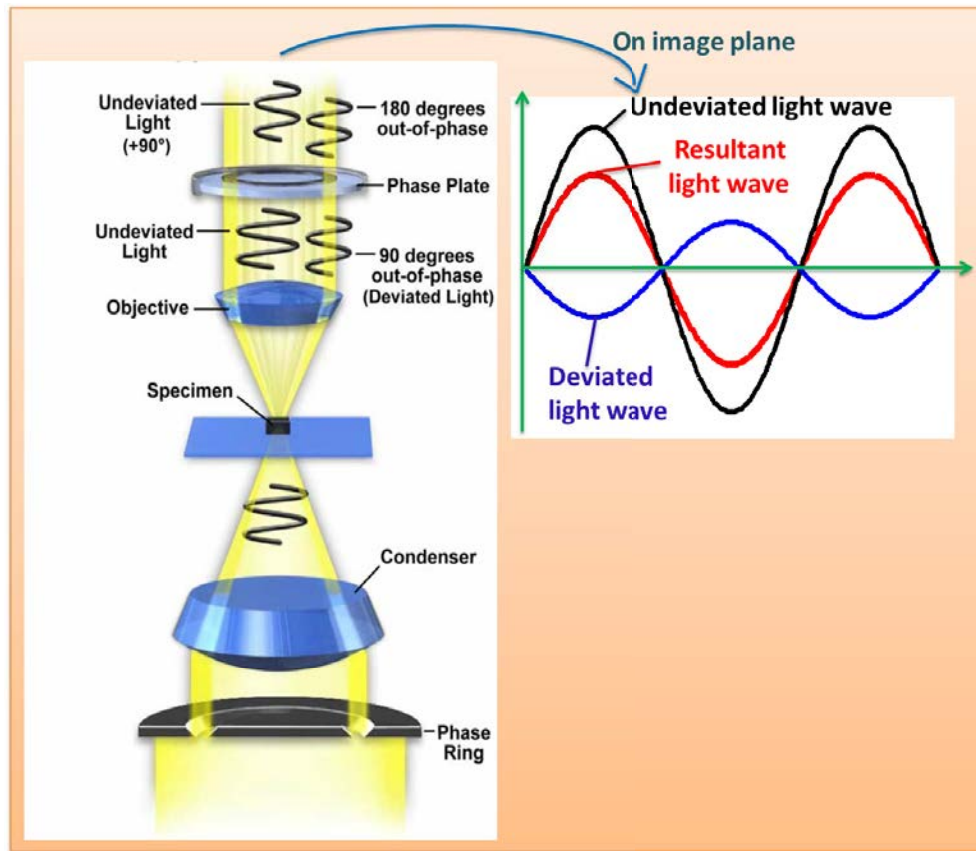


Figure 3.8: Schematic configuration for phase contrast microscopy. Light passing through the phase ring is first concentrated onto the specimen by the condenser. Undeviated light enters the objective and is advanced by the phase plate before interference at the rear focal plane of the objective. The ray diagram shows the destructive interference between the undeviated and deviated light. As the resultant wave is weaker than undeviated light wave, the specimen appears dark [DM, BOJR51].

As the hollow cone of light from the annulus passes through the specimen undeviated, it arrives at the rear focal plane of the objective in the shape of a ring of light. To speed up the direct undeviated zeroth order light, a phase plate is installed with a ring shaped phase shifter (phase annulus) attached to it at the rear focal plane of the objective. The narrow area of the phase annulus is optically thinner than the rest of the plate giving an extra $1/4$ wavelength phase shift. As a result, undeviated light passing through the phase annulus travels a shorter distance in traversing the glass of the objective than the diffracted light. Now, when the direct undeviated light

and the diffracted light proceed to the image plane, they are $1/2$ wavelength out of phase with each other. The diffracted and direct light can now interfere destructively so that the details of the specimen appear dark against a lighter background. The demonstration of this interference in terms of ray diagram on the image plane is shown in Fig. 3.8 being descriptive of a positive or dark phase contrast. For instance, the uniform void structure imaged in positive phase contrast mode is shown in Fig. 3.9 (a).

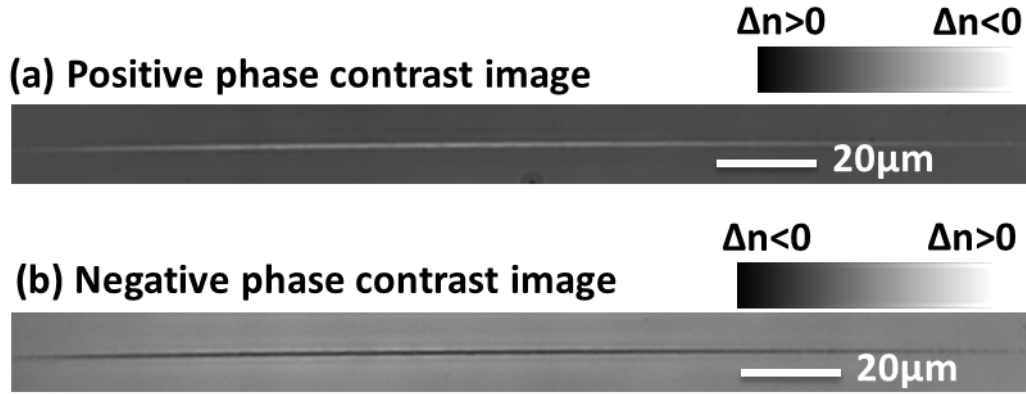


Figure 3.9: Positive and negative phase contrast images of the uniform void structure.

If the ring phase shifter area of the phase plate is made optically thicker than the rest of the plate, direct light is slowed by $1/4$ wavelength. In this case, the zeroth order light arrives at the image plane in step (or in phase) with the diffracted light, and constructive interference takes place. This arrangement results in a bright image of the details of the specimen on a darker background, and is called negative or bright contrast. For example, here, the uniform void structure in negative phase contrast mode is shown in Fig. 3.9 (b). In this thesis, we used the microscope in positive phase contrast mode for the imaging of refractive index profiles (darker regions represent positive index change and brighter regions represent negative index change) with a resolution close to the limit of diffraction of the microscope.

In brief, absorption of the specimen is projected on to the image plane of CCD camera in optical transmission microscopy where as phase retardation by the specimen is projected on to the image plane in phase contrast microscopy. It is important to note that for a non-transparent samples where the amplitude components are stronger, there could be a mixed information of phase and amplitude in PCM images. These projection images are processed using the Abel inverse transform to obtain the accurate details of the original radial profiles. The mathematical background and the used algo-

rithm of the Abel inverse transform are discussed in the appendix A.

An EMCCD (ANDOR iXon Ultra 897 model) camera was used along with the microscope to capture the optical transmission and phase contrast images. It has a back-illuminated 512×512 frame transfer sensor technique and overlocks readout to 17 MHz, pushing speed performance to an outstanding 56 fps (full frame), whilst maintaining quantitative stability throughout.

It is important to note that high sensitivity cameras are very sensitive to illumination conditions and should be operated in a linear regime. That is, the transfer function between the incident photonic signal and the final digitized output should vary linearly with the amount of light incident on the CCD. Particularly in our case, time resolved experiments have to be measured in a linear regime to avoid the overestimation or underestimation of the transmission. Here we recall that the transmission is a crucial parameter to study the dynamics of free carriers and it has to be accurately measured. We have calibrated our CCD camera with probe laser energy and always operated in a linear regime. The variation of the intensity counts (grey value) of the CCD signal with the probe laser energy is shown in Fig. 3.10. The linear regime of the camera has been highlighted.

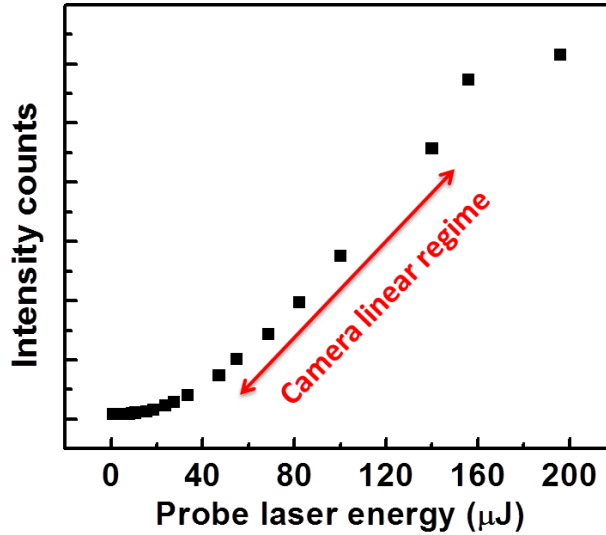


Figure 3.10: Intensity counts (grey values) of the CCD signal with the probe laser energy. The linear regime of the camera is mentioned.

As we mentioned, in our experiments, transmittance is a major parameter that provides the estimation of free carrier density. To understand the variation of transmittance with carrier density and probe wavelength, we

performed the finite-difference time-domain (FDTD) simulations using the Drude formalism. Equally, scattering or diffusion effects of the probe beam over the small structures or in other words size effects on experimentally measured transmittance are also a prime concern.

3.4 FDTD simulations: transmissivity vs electron density

The size of the plasma derived from the high resolution optical transmission imaging using Olympus 100X (NA 0.9) optical transmission microscope objective. Instantaneous optical transmission image is shown in Fig. 3.11 indicating the free carrier or plasma absorption in void fabrication conditions for a laser pulse energy of $8 \mu\text{J}$ and pulse duration of 4.7 ps. The size of the plasma column is found to be $\sim 500 \text{ nm}$. In order to understand the role of



Figure 3.11: High resolution instantaneous optical transmission image indicating the plasma or free carrier absorption in void fabrication conditions ($8 \mu\text{J}/\text{pulse}$, 4.7 ps).

probe scattering effects by the plasma column where the object size is smaller than the wavelength, we estimated theoretically the transmissivity through shapes of the plasma column resembling a rod (as nearly equivalent to our Bessel excitation profile) and a disk. Consideration of these two shapes of plasma column is to show the behavior of small object because of the scattering, where additional photons go around and overestimate the transmittance. Equally, role of probe wavelength and carrier densities on the transmission is validated. Transmissivity as a function of electron density is estimated using FDTD calculations based on Drude formalism. We assumed the electric field that is passing through perpendicularly to the infinitely long rod, diameter of 500 nm (FWHM of Gaussian distribution) and disk of lateral size $9 \mu\text{m}$, with a thickness of 500 nm. These calculations will elucidate the experimentally observed measurements i.e., role of probe wavelength on transmission. Also the role of lateral size of the plasma column on transmission, particularly the scattering effects that are associated with the size of plasma column can be understood. For the transmissivity estimations using the Drude formula, we have considered the parameters: carrier damping time as 1 fs and car-

rier effective mass as $m^* = m_e$. These theoretical estimations may not refer the exact value of the carrier density but qualitatively gives the evolution of transmission with the carrier density.

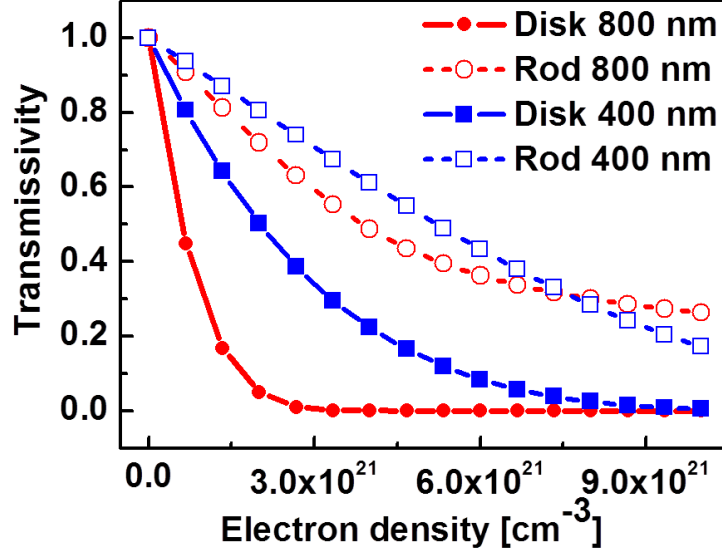


Figure 3.12: Theoretically calculated transmissivity as a function of free carrier density from FDTD calculations based on Drude formalism at 400 nm and 800 nm wavelengths for infinitely long rod of diameter 500 nm and 9 μm wide disk of thickness 500 nm.

Theoretically calculated results of the transmissivity as a function of electron density through a infinitely long rod and through a disk of large lateral size are shown in Fig. 3.12. The results for the rod in plot are shown with the dotted line connection to the data points. It is noticed from the results that transmissivity through the rod is lower for 800 nm compared to 400 nm at moderate electron densities. They both stay above the value of disk transmission. At very high electron densities transmissivity of the rod for 400 nm is decreased compared with the 800 nm. Transmissivity through the disk shaped plasma object at various electron densities is shown in figure by continuous lines for 400 nm and 800 nm with lower values for the 800 nm case, as expected from a Drude model. Transmission through the disk is observed to be lower than the transmission through the rod for both wavelengths. This shows the possibility of scattering effects and the light surpassing through the boundaries of the rod (over a small object). These effects result in overestimating the transmission for the rod. From this point, it can be concluded that the estimation of free carrier densities could be underestimated because of the scattering effects around the plasma

column which will lead to the higher transmittance.

3.5 Post irradiation techniques

The photoluminescence spectra of laser induced structures were recorded with a Horiba Jobin Yvon confocal Raman microspectrometer (ARAMIS). Three laser sources were used for excitation, covering the four excitation wavelengths: HeNe laser at 633 nm (1.96 eV), Argon ion laser at 488 nm (2.54 eV), and HeCd laser at 442 nm (2.81 eV) and 325 nm (3.82 eV). These wavelengths usually cover the excitation bands of NBOHC and ODC defect centers. Scanning Electron Microscopy (SEM) by FEI (model: Nova Nano SEM) was used for the structural (size) characterization i.e., to measure the cross sectional profiles of fabricated sub-micron structures. Focused Ion Beam (FIB) technique is employed for the cleavage of the bulk sample for imaging the side view of fabricated structures which are inside the bulk.

3.6 Conclusions

This chapter has given the description of experimental techniques that are used for zeroth order Bessel beam generation and characterization techniques, sub-micron structuring, and time resolved measurements. A small section was dedicated to give the overview and working principle of the microscopy in optical transmission and phase contrast modes. Also discussed the requirement of image treatment techniques for the correction from projection. We presented the role of scattering effects of the probe beam due to the plasma size on transmittance using FDTD simulations. Other than in-situ measurements, details about post irradiated structural characterization techniques have been given in brief.

Chapter 4

Material processing using single shot ultrafast Bessel beams

This chapter describes the fabrication of high aspect ratio sub-micron permanent structures using single shot ultrafast laser Bessel beams at moderate focusing conditions. It briefly outlines the importance of zeroth order Bessel beams over Gaussian beams for material processing applications. Their potential in nano structuring is emphasized. Role of Bessel cone angle (focusing conditions) is outlined briefly as focusing conditions define the degree of stability of the intense Bessel beam interaction with transparent materials. At similar focusing conditions i.e., same conical half angle of the Bessel beam and at the same laser pulse energy, chirping of the ultrafast Bessel beams has given two unique interaction regimes. Femtosecond laser pulse interaction resulted in smooth refractive index structures whereas picosecond laser pulse interaction resulted in the uniform void structures. Moderate focusing conditions offer the stable interaction over broad range of laser parameters. Hence, we explored the different interaction regimes in moderate focusing conditions with the laser pulse duration and energy and identified the stability regimes of the nonlinear Bessel beam propagation which yields the uniform structures. In order to understand the pulse duration dependent transitional behavior of the interaction, a nonlinear propagation model which is based on nonlinear Schrödinger equation has been applied. The sequential energy deposition of a pulsed beam propagation offers insights into the mechanisms of Bessel interaction in fused silica at different temporal regimes. Also we propose the fabrication of very high aspect ratio structures at loose focusing conditions.

4.1 Overview: importance of zeroth order Bessel beams for high aspect ratio structuring

Femtosecond lasers have unique advantage for material processing of transparent materials, for instance, higher order photoionization mechanisms such as multiphoton ionization (MPI) restricts the interaction volume within the bulk of the material resulting in localized laser induced structures with increased precision. Also quality and precision in laser induced structuring can be done by controlling the several nonlinear excitation and relaxation mechanisms at different time scales depending up on the laser parameters and material characteristics. For all of the physical sequences, nonlinear pulse propagation has a determinant role. Prior to the damage process, depending on the incident peak power, the conventional Gaussian laser beams may undergo filamentation, building up on the dynamics of self-focusing caused by non-uniform profiles and defocusing effect on free carriers generated during the early part of the laser pulse. As a result, the modified interaction volume gets extended in the bulk of the material [CM07]. A wide range of applications using standard Gaussian laser beams in combination with spatial and temporal engineering of the laser pulse have been exploited [SCM⁺14]. However, due to the inherent diffraction characteristics of the Gaussian beams, the laser-based material processing using such beams is less efficient in structuring high aspect ratio (length/diameter) structures as often required for deep drilling and photonic crystal applications. Also numerous challenging applications in nanophotonics and nanofluidics require the fabrication of high aspect ratio nano-channels, a key technological challenge with the Gaussian material processing in dielectrics since their spatio-temporal distortions during the propagation prevents the fine control over the energy deposition. For instance structural modifications using Gaussian beams in single, multiple pulse and dynamic scan conditions are shown in Fig. 4.1. Dark regions in Fig. 4.1 represent the isotropic positive refractive index structures denoted as type-I and bright regions represent the negative index change structures termed as type-II. Single shot modifications using Gaussian pulses are shown in Fig. 4.1 (a). Here the length of structures is in the range of 10 to 30 μm with non-uniform structural modifications. Filamentation of Gaussian beams using moderate focusing geometry can also help in producing long structures in a single-pulse but this would also results in non-uniform structural modifications with index modulations. The multipulse static structures (shown in Fig. 4.1 (b)) can produce quite uniform modifications with compromising the aspect ratio and consumption of time in bulk micro-machining. In such cases, many alternatives have been proposed. For example, irradiation with

laser while continuously moving the material along the desired direction can produce high aspect ratio structures in transparent materials. The typical dynamic structures fabricated in this process are shown in the Fig. 4.1 (b). Their index variation was tested for light transport (waveguiding with good transport) but still with a compromise in the uniformity of the altered material characteristics along the structural length. At higher energies and low scan velocities, the regular nanogratings formation (seen in cross-sectional profiles) perpendicular to the laser field with sub-wavelength periodicities has been observed in fused silica [MDV⁺13].

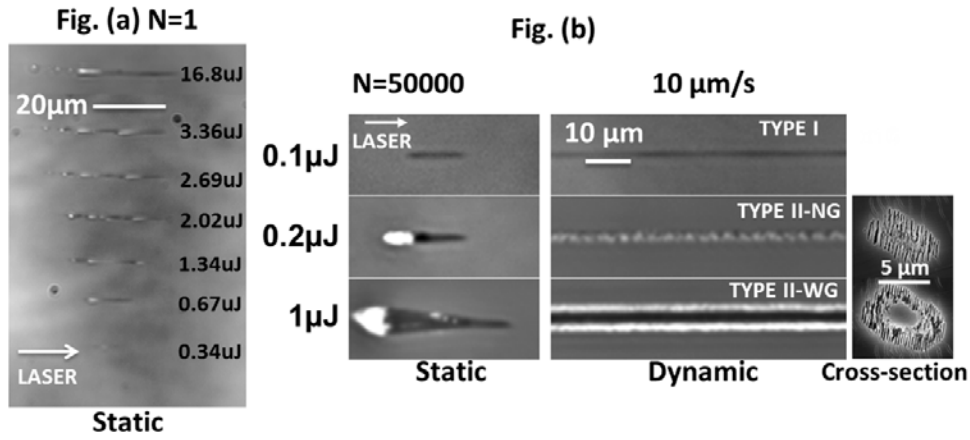


Figure 4.1: Single, multiple shot static and dynamic structures using Gaussian pulses. (a) shows the single shot ($N=1$) structures at different energies; multipulse ($N=50000$) static and longitudinally scanned structures (dynamic) are shown in (b) [MDV⁺13]. White/block colors indicate negative/positive index changes.

Recently, nondiffractive Bessel beams [DMJE87] were proposed to solve this issue; namely high aspect ratio, uniform and sub-micron structuring of transparent materials using single shot fs laser pulse [BCL⁺10b, BCP⁺11]. The important linear characteristic of zeroth-order Bessel beams is the long nondiffracting distance - an order of magnitude higher than an equivalent confocal length of Gaussian beams using nearly similar focusing geometry - over which the laser energy is deposited into the bulk of the materials in a conical fashion. This presents certain advantages for the single shot machining techniques as efficient structuring along long dimensions can be realized. Besides, Bessel beams are also stable against nonlinear losses while propagating in condensed media [PFC⁺08]. The possible Bessel filamentation scenarios depending on focusing conditions and laser parameters were discussed in the section 2.2.2.

Chapters 2 and 3 have given the basic background of the zeroth order Bessel beams and its experimental generation techniques. We recall here the experimental conditions. Generally, use of the Bessel beams of larger conical half-angle $\theta \geq 11^\circ$ (in glass) corresponding to a tight focusing geometry permitted the achievement of structures of length up to $100\ \mu\text{m}$ and diameter in the range of 200 to 800 nm. As for a fixed aperture beam, smaller cone angle corresponds to longer nondiffracting length of Bessel beams, exploring looser focusing geometries is of interest for even higher aspect ratio structuring. This sets a quest of producing longer structures. However when ultrafast Bessel beams of $\theta \sim 7^\circ$ (in glass) were used, single-shot structuring was not possible [BCL⁺10a]. 1000 laser pulses were required to produce a single microchannel ($80\ \mu\text{m}$ long and $2\ \mu\text{m}$ diameter) in borosilicate glass. This is because of the poor stability of nonlinear propagation of ultrafast Bessel beams of low cone angle [PFC⁺08] causing inefficient transfer of laser energy into the material. In this chapter, we demonstrate that low cone angle Bessel beams (moderate focusing conditions, 8.3°) can have significantly higher degree of stability of nonlinear propagation in transparent materials by properly selecting the laser pulse duration and energy. For instance, in the following section, we give a brief idea about how different focusing conditions effect the stability of interaction, eventually the structural modifications.

4.2 Role of Bessel cone angle

The degree of stability of the nonlinear interaction of Bessel beams in transparent media depends on the focusing conditions which are defined by the conical half-angle of the Bessel beam. In this section, we briefly show the different structural modulations signaling the stability of the interaction in different focusing conditions. Particularly, we present the results in loose, moderate and tight focusing conditions corresponding to the conical half-angle of the Bessel beam inside the sample of 4.2° , 8.3° and 15.1° respectively.

Loose focusing conditions:

Phase contrast microscopy images of the single pulse ultrafast Bessel beam induced structural modifications in loose focusing conditions are shown in Fig. 4.2. Note in the figure that dark and bright zones of a positive PCM images correspond to the higher and lower refractive index change zones of the material modifications respectively. Selective structural modifications for 60 fs laser pulse duration are shown in the Fig. 4.2 (a) and (b). In this focusing conditions, we observed the stable smooth refractive index structures

for a fs laser pulse over a small energy range. For example, the structure is as shown in Fig. 4.2 (a) at $7.2 \mu\text{J}/\text{pulse}$. Higher energies in this loose focusing conditions for an ultrashort laser pulse results in structural modulations along the axis. For instance, the modulated structure is shown as in Fig. 4.2 (b) at $20.2 \mu\text{J}/\text{pulse}$ reflecting the unstable interaction in terms of a succession of alternatively positive and negative index domains. The longer period ($\sim 100 - 200 \mu\text{m}$) indicates the focusing-defocusing dynamics as reported in [PFC⁺08]. Increasing pulse duration offers unexpectedly a possibility to determine uniform interaction over the non-diffracting range. Ps laser pulse duration in this focusing conditions offers the long uniform structural modifications with low refractive index change over a small energy range, for example as shown in Fig. 4.2 (c) at 1 ps and $26 \mu\text{J}/\text{pulse}$. This low index (void like) structures have upto $\sim 1 \text{ mm}$ long leading to the very high aspect ratio (exceeding 2000) structures.

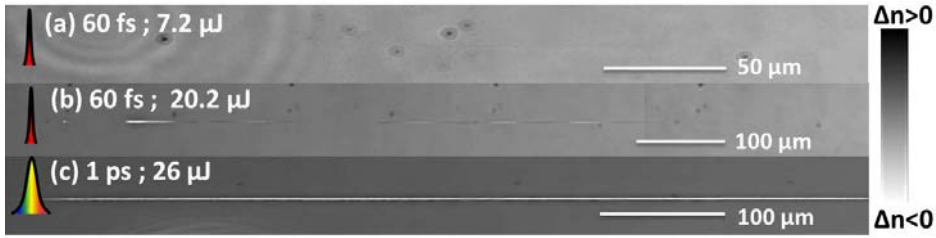


Figure 4.2: Selected phase contrast microscopy images of the structural modifications using single shot ultrafast Bessel beam under loose focusing conditions (conical half-angle of the Bessel in the medium $\sim 4.2^\circ$). (a) Smooth refractive index structure at pulse duration of 60 fs and energy of $7.2 \mu\text{J}/\text{pulse}$. (b) Modulated structure at pulse duration of 60 fs and energy of $20.2 \mu\text{J}/\text{pulse}$. (c) Uniform low index (void like) structure at pulse duration of 1 ps and energy of $26 \mu\text{J}/\text{pulse}$.

Moderate focusing conditions:

In moderate focusing conditions, we noticed the uniform smooth refractive index structures in fs regime and uniform low index (negative index change) structures in ps regime. For example, PCM image of the smooth refractive index structure at $6 \mu\text{J}/\text{pulse}$ for 60 fs pulse duration is as shown in Fig. 4.3 (a). Uniform negative index structure at $6 \mu\text{J}/\text{pulse}$ for 4.7 ps pulse duration is as shown in Fig. 4.3 (b). In this focusing conditions, we noticed the stable interaction regime over a wide range of laser parameters.



Figure 4.3: Selected phase contrast microscopy images of the structural modifications using single shot ultrafast Bessel beam under moderate focusing conditions (conical half-angle of the Bessel in the medium $\sim 8.3^\circ$). (a) Smooth refractive index structure at 60 fs and 6 μJ /pulse. (b) Uniform void structure at 4.7 ps and 6 μJ /pulse

Tight focusing conditions:

Phase contrast microscopy images of the structural modifications in tight focusing conditions are shown in the Fig. 4.4. In these focusing conditions, modulations in the structures have been observed in both fs and ps regimes. For instance, structural modulations for 60 fs pulse duration are as shown in Fig. 4.4 (a) and (b) at 4.2 μJ /pulse and 25 μJ /pulse respectively suggesting mixing of filamentation and fragmentation cycles. The structures in ps regime are shown in Fig. 4.4 (c) and (d) at 7 μJ /pulse and 25 μJ /pulse respectively. These focusing conditions could not lead to the uniform structural modifications with light scattering observed at higher energies. It indicates that the tight focusing conditions in fused silica are leading to the unstable interaction regimes outside a narrow parameter range.

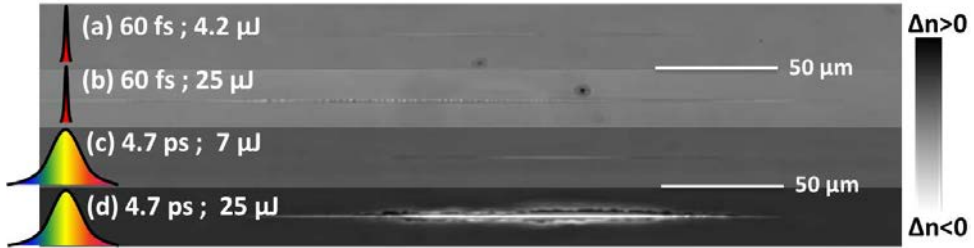


Figure 4.4: Selected phase contrast microscopy images of the structural modifications using single shot ultrafast Bessel beam under tight focusing conditions (conical half-angle of the Bessel in the medium $\sim 15.1^\circ$). Figures (a) and (b) are the PCM images in fs regime (60 fs) at 4.2 μJ /pulse and 25 μJ /pulse respectively. PCM images in ps regime (4.7 ps) are shown in (c) and (d) at 7 μJ /pulse and 25 μJ /pulse respectively.

As we have seen, focusing conditions of the Bessel beam play a major role in stability of the interaction. In other words, Bessel conical-half angle is

a crucial parameter along with the laser parameters to define the stability of interaction. It was noted that the stationary and localized wave propagation in a media with nonlinear losses can be possible only for positive wave vector shift $\delta > 0$ (cone angle $\theta = \sqrt{(2\delta/k_0)}$) [PPF⁺04]. The stability criteria with nonlinear phase terms for a given medium characterized by its Kerr nonlinear index n_2 and nonlinear absorption coefficient $\beta^{(K)}$ given as :

$$\delta > \max\{g_K \beta^{(K)} I_0^{K-1} - k_0 n_2 I_0 / n_0, 0\} \quad (4.1)$$

where g_K only depends on the order of multiphoton processes ($g_K = 1.67, 0.27, 0.19, 0.16, \dots$ for $K = 2, 3, 4, 5, \dots$). Recently it was mentioned that the same criterion is also valid for nonlinear Bessel vortices [JMX⁺14]. The structural modulations (unstable regimes) are due to the complex nonlinear interaction mechanisms. Interpreting the formation mechanisms of this unstable regimes with different cone angle in various transparent materials is an ongoing challenge.

Here it is important to mention that our work is mainly focused on understanding of the formation mechanisms of uniform structures resulting from the stable interaction. We emphasize that loose focusing conditions offer the very high aspect ratio structures with choosing the appropriate laser parameters. As moderate focusing conditions offer the stable interaction regime over a wide range of laser parameters compared to loose and tight focusing conditions, we exploited the different interaction regimes in these focusing conditions with different laser parameters. For instance, in the following sections we present the role of laser pulse duration and detailed material processing features in fs and ps regimes. Also we summarize the different interaction regimes over a wide range of laser pulse durations and energies.

4.3 Role of laser pulse duration

The results of single shot structuring as a function of the laser pulse duration are summarized in Fig. 4.5. The laser pulse duration is varied from 60 fs to 5.2 ps using positive second order dispersion at the same laser energy 4.1 $\mu\text{J}/\text{pulse}$. For the pulse durations of 60 fs and 1.7 ps (until $\sim 2\text{ps}$), structures with increased refractive index (dark regions) have been observed. Pulse durations from 2.6 ps to 5.2 ps lead to the observation of void like low density (bright regions) structures. Increased refractive index structures (increase of the refractive index more than 10^{-4}) are termed as type-I and negative refractive change ($\Delta n \sim 10^{-2}$, upto a maximal $\Delta n = 0.45$), low index structures are called as type-II. A transition from type-I in case of

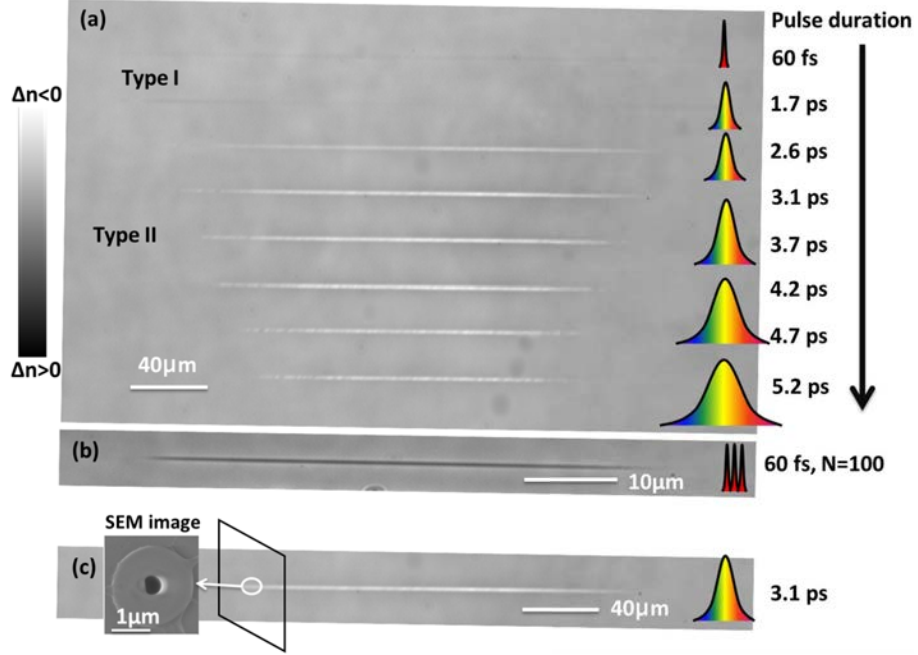


Figure 4.5: (a) Phase contrast microscopy images of the single-shot structures machined inside fused silica using laser energy of $4.1 \mu\text{J}/\text{pulse}$ and pulse duration in the range 60 fs to 5.2 ps revealing the morphological changes corresponding to type-I and type-II regimes. Type-I in multipulse conditions at $1 \mu\text{J}/\text{pulse}$ is shown in (b) to enhance visibility and SEM cross sectional profiles of the uniform void structure is shown in (c) for a 3.1 ps laser pulse.

ultrashort pulse to a pure type-II (only void) structure with increasing laser pulse duration is clearly observable from Fig. 4.5 (a); the transition is nearly independent of laser polarization in the studied range. In the present case, the transition from type-I to type-II occurs around 2 ps and the longest uniform void was observed for 3.1 ps with a remarkable spatial uniformity extending to scales similar to the non-diffracting length of Bessel beams. Further increase in the pulse duration deteriorates the quality and length of the machined structures. From additional experiments, we also observed that the physical characteristics of the Bessel beam induced structures are approximately same when machined using laser pulses with positive and negative chirp.

The smooth refractive index structure with increased contrast is shown in the Fig. 4.5 (b) for the 100 pulses (to enhance visibility), 60 fs and the laser energy of $1 \mu\text{J}/\text{pulse}$. It shows a uniform morphology. The diameter of the fabricated structures was measured using scanning electron microscopy (SEM) for open structures. For instance, uniform void structure at 3.1 ps

laser pulse duration and its cross sectional morphology is shown in Fig. 4.5 (c). The structure diameter is found to be ~ 350 nm. For most of the fabricated structures in single shot and under moderate focusing conditions, the structure diameter is observed to be below the 400 nm. The size can be reduced either by tighter focusing or pulse duration control. For example, cross-sectional SEM images of the low index structures made in this case through the surface at various laser pulse energies in ps and fs pulse durations for moderate and tight focusing conditions are shown in Fig. 4.6. We recall

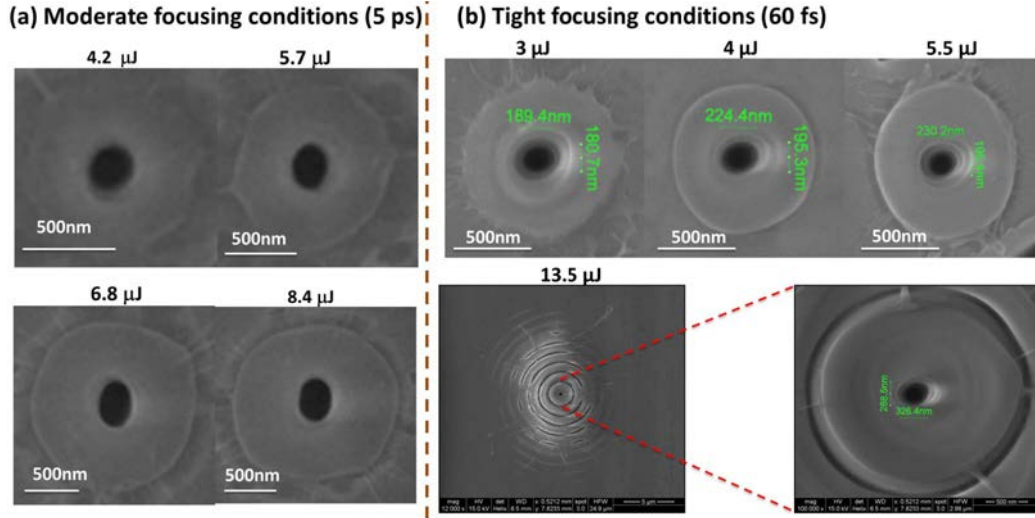


Figure 4.6: SEM cross-sectional images of the void structures at different energies in moderate (a) and tight (b) focusing conditions for structures crossing an interface.

that the in-situ characterization of bulk static structures is mainly done by using the phase contrast microscopy. The dark regions in the positive phase contrast microscopy images indicate the smooth or positive refractive index change structures and bright regions indicates the low index structures. In most of the cases in our study, particularly in ps regime (pulse duration ≥ 2 ps) low index or bright regions in PCM images are the voids. In the following we show the post-processed characterization techniques demonstrating that low index structures are voids.

Confirmation of voids:

Relying on the bright regions in the phase contrast microscope based on the phase or index contrast, concluding them as voids is questionable, as these bright regions could be modulated index regions or just low index regions. To

validate these queries, post-processed characterization techniques have been done to confirm the voids formation. We cleaved the low index structures by Focused Ion Beam (FIB) and these structures have been imaged by SEM. The cleaved SEM images (side-view images) are shown in Fig. 4.7. The formation of voids is clearly evident from the images. Uniform scattering from the low

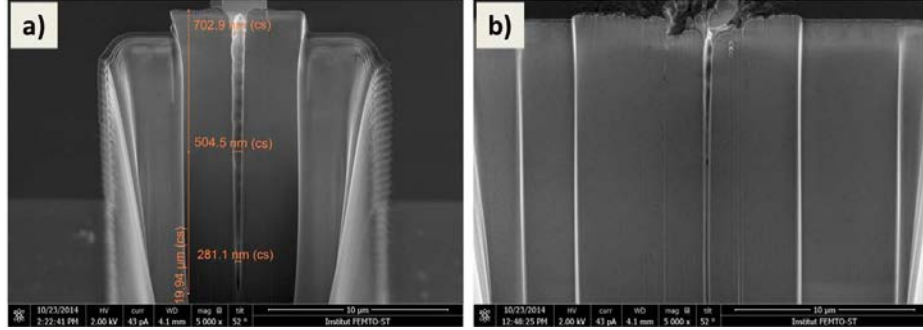


Figure 4.7: SEM images of the two different void structures (a) and (b) after cleaved by the FIB. Images made by the gracious contribution of FEMTO-ST. Note in figure (a) that the different structural diameters are due to non-uniform cleavage of the material.

index structures is observed in optical transmission microscopy (OTM) image as shown in Fig. 4.8 (a). OTM image (scattering) is therefore used as a rapid qualitative confirmation for formation of uniform void structures. Also we dipped the sample containing the terminated channel (the structure is opened at one side) into water and examined the presence of water inside the channel under optical microscopy. The same structure after water filling as shown in Fig. 4.8 (b) evidencing water penetration and therefore the presence of a void space. The above characterizations i.e., SEM, PCM, OTM and water filling indicate the formation of voids and low density regimes in PCM images are proven to be voids. We used the terminology “void” wherever we dealt with similar conditions where the above characterization techniques were done and regimes where uniform voids occur. Elsewhere, we used the word “low index” or “low density” regions. Also here we underline that the bright regions in the positive PCM images in single pulse modification are quite safe to be defined as voids as we can not have sub-wavelength modulated structures (nanogratings) as in the case of multi-pulse regime. For instance, multi-pulse laser irradiation in fused silica produces modulated index modifications i.e., a pattern of low density and dense layers with sub-wavelength periodicity that might appear as white in PCM despite the presence of dense layers. In this case, PCM could reflect the average phase retardation with in the inspected region giving the dominant material modification and reflect the retardation

due to the form birefringence.

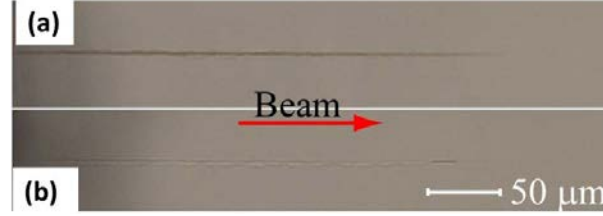


Figure 4.8: OTM images of the uniform void structures with out and with filling of the water are shown in (a) and (b) respectively.

4.4 Material processing in femtosecond regime

In this section, we present the role of laser energy and accumulation effect on Bessel excited material modification for an ultrashort laser pulse duration (60 fs).

4.4.1 Role of energy

As we have seen, single shot Bessel excitation in fs pulse duration regime offer the uniform smooth positive refractive index structures. To explore more about this regime, we varied the laser pulse energy at shortest pulse duration (60 fs) in the single shot mode. The PCM static structures at various energies are shown in Fig. 4.9. As we increase the laser pulse energy from the modification threshold, there is a transition towards slightly more contrasted smooth positive index modifications and further increasing of laser energy leads to the unstable morphological structures. The respective structural modifications can be seen as a refractive index map in phase contrast microscopy images. The smooth refractive index structures are found until the laser pulse energy $\sim 10 \mu\text{J}$. As we increase the energy, the structures become more non uniform in morphology i.e., mixed in the refractive index changes. Higher energies at fs laser pulse duration would lead to complex nonlinear propagation which determine the modulations in refractive index structures. The variation of the modified structural length with laser energy is estimated and it is as shown in the Fig. 4.10. The increasing length versus energy is related to the bell-shape axial intensity profile of the Bessel line beam. The estimated structure length based on the width of bell shaped beam at the threshold peak intensity ($\sim 9 \times 10^{13} \text{W}/\text{cm}^2$) for various energies is also shown in the figure. It is noticed that the experimentally measured

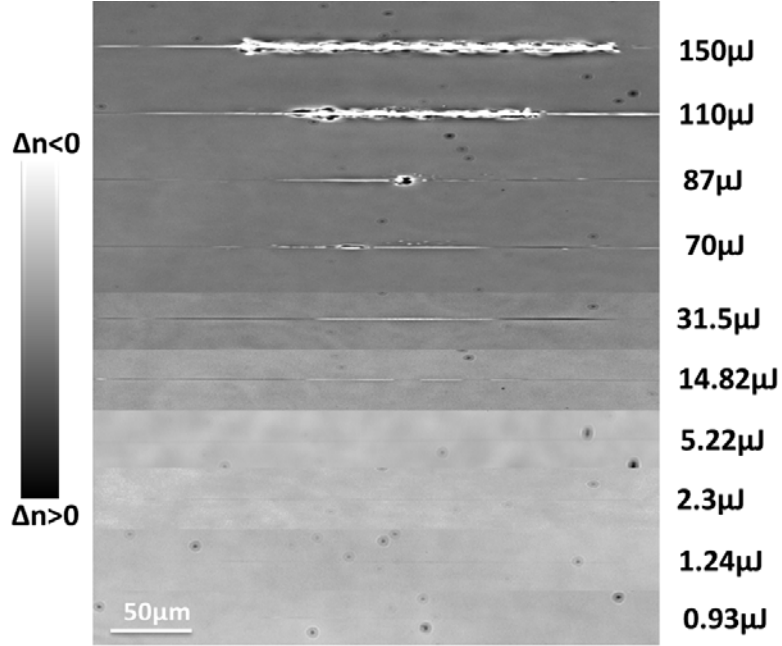


Figure 4.9: Phase contrast microscopy images of the single-shot structures machined inside fused silica using the laser pulse duration 60 fs at various energies per pulse. Here note that only central portion of the modification is only shown as it contains the significant information.

structural length is increased with the energy and structural length is higher than the estimated (linear) length. This indicates a need for accounting of the nonlinear effects that are more pronounced with increasing of the laser energy.

4.4.2 Accumulation effect

At low laser pulse energy (close to modification threshold $\sim 1 \mu\text{J}$, where the static permanent structures in PCM can be visible), we studied the accumulation effect of laser pulses i.e., interaction with multiple laser pulses. The structural morphologies in phase contrast microscopy image at different number of laser pulses are shown in the Fig. 4.11. As we increase the number of laser pulses, the contrast of the positive refractive index has been increased. At this laser energy, only isotropic positive index structures are observed even at higher number of pulses.

The effect of interaction with accumulated laser pulses above the damage threshold is shown in Fig. 4.12. The smooth refractive index structures are observed for lower number of pulses. Structural modulations which are

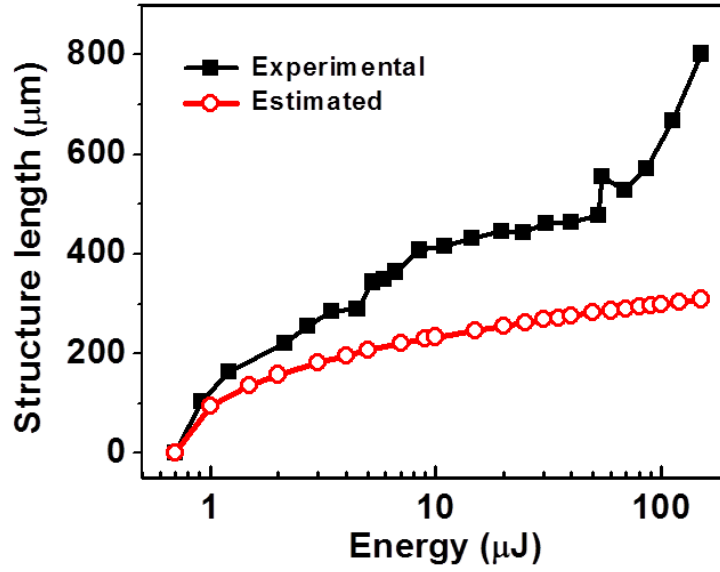


Figure 4.10: Plot of the modified structural length with the variation of laser energy for a laser pulse duration of 60 fs. Note the logarithmic scale of laser energy.

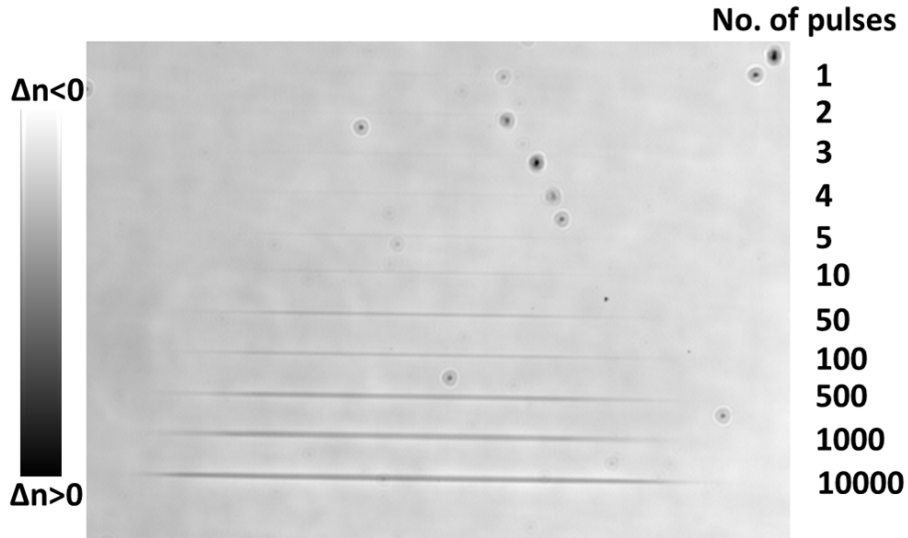


Figure 4.11: Phase contrast microscopy images of the machined structures at various number of pulses inside fused silica using the laser pulse duration of 60 fs and the energy $\sim 1 \mu\text{J}$.

mixed with positive and negative refractive index structures are observed at higher accumulation rate. We note that the appearance and disappearance

of the voids with increasing the number of pulses indicate the possibility of erasing the laser-induced structures by subsequent irradiation. This signals the presence of a soft low viscosity material phase around the voids. Additionally, in their vicinities or in between, regions of compacted material with higher positive index contrast are noticed.

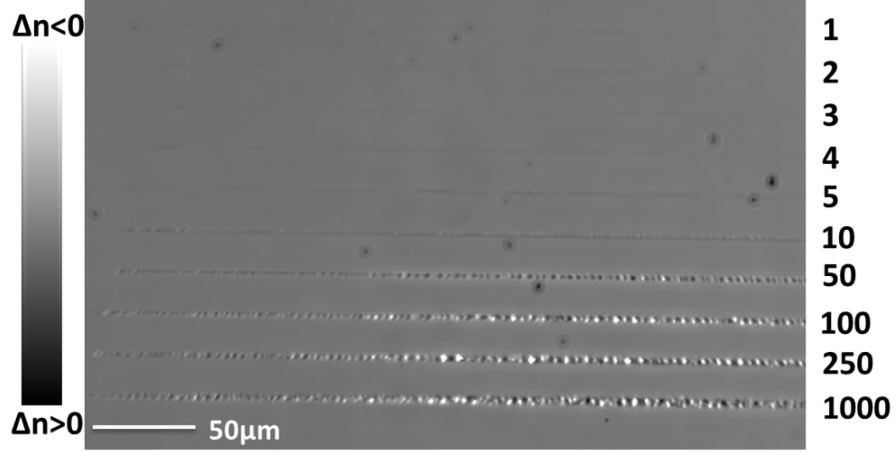


Figure 4.12: Phase contrast microscopy images of the machined structures at various number of pulses inside fused silica using the laser pulse duration of 60 fs and the energy $\sim 6 \mu\text{J}$.

4.5 Material processing in picosecond regime

Bessel interaction in ps pulse duration regime indicates the possibility to obtain the uniform void structures at moderate energies. The various structural modifications with different energies at 5.2 ps laser pulse duration in phase contrast mode are shown in Fig. 4.13 and optical transmission images are shown in Fig. 4.14. At lower pulse energies, we observed the modulated structures and with increasing of the laser pulse energy, the modification effect resulted in uniform void structures. If we increase further the laser pulse energy, this leads to the complex structural modulations. The modulations at lower energy ($2.5 \mu\text{J}/\text{pulse}$) are associated with the instabilities in the interaction because of the low efficiency of nonlinear photo-ionization. The uniform voids are observable in the pulse energy range between ~ 4.5 to $15 \mu\text{J}/\text{pulse}$. The uniform light absorption or scattering from the void structures in OTM images within this energy range is evident in the smooth and clear uniform structures. If we increase the energy further, strong modulations appear in the structure. For instance, for laser pulse energies between the $24 \mu\text{J}$

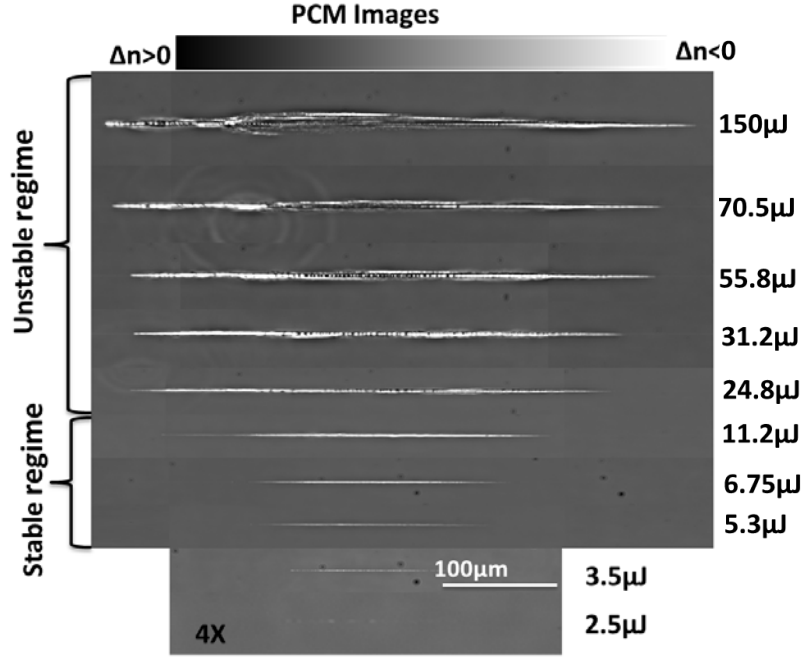


Figure 4.13: Phase contrast microscopy images of the single-shot structures machined inside fused silica using the laser pulse duration of 5.2 ps at various energies per pulse.

to 56 μJ , there is a repetition of voids and increased refractive index domains quasi-periodically with the spacing of ~ 3 to 6 μm . The periodic modulations of these structures are also clearly seen in OTM images. This kind of oscillations are potentially due to the combined action of self-focusing and nonlinear losses in the intense central core of the Bessel beam resulting in the unsteady Bessel filamentation [PFC⁺08]. It is nevertheless worth considering in the view of the small periodicity (less consistent with the filamentation) that hydrodynamic fragmentation effects may playing an important role. At very high energies (above 60 μJ), highly non-uniform structural modifications have been observed and they could be due to the interplay of the nonlinear interactions in intense core region and its nearest rings of the Bessel beam. The screening effect in the center of the core are clearly seen. SEM side view image is shown in the Fig. 4.15 representing the screening effect zone. It can be seen that along the core (center of the propagation axis) there is a narrow opening followed by a large damage away from the axis indicating the limitation of energy deposition on the axis at high energies. Equally, at such high energies, rings of the Bessel beam could also influence the nonlinear interactions. In the PCM and OTM images (Figs. 4.13, 4.14), we highlighted

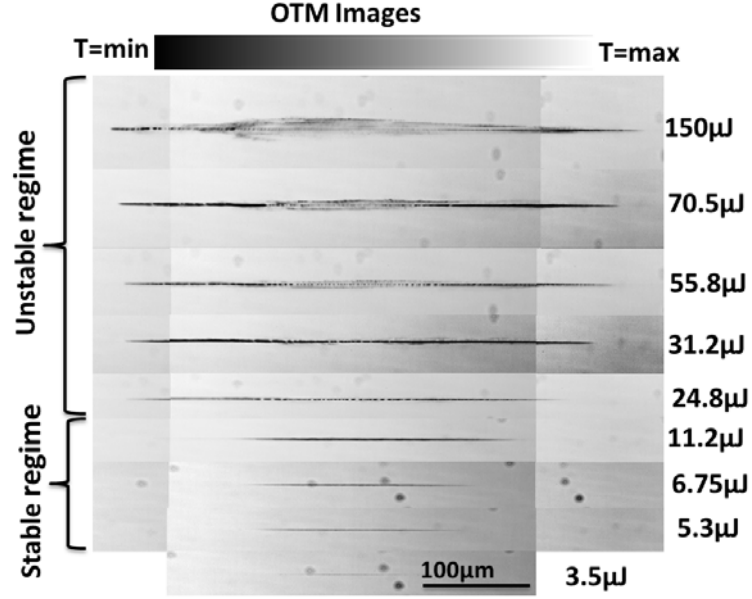


Figure 4.14: Optical transmission microscopy images of the single-shot structures machined inside fused silica using the laser pulse duration of 5.2 ps at various energies per pulse.

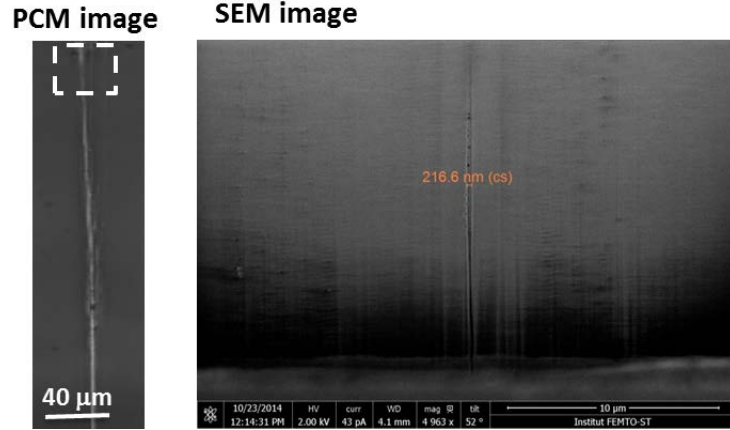


Figure 4.15: PCM and SEM side view images of the structure indicating the screening effect zone on the core at $\sim 150 \mu\text{J}/\text{pulse}$.

the stable and unstable interaction regimes depending on structural modifications. The variation of the modified structural length with the laser pulse energy is measured and it is as shown in the Fig. 4.16. Also the estimated structural length, i.e., width of the longitudinal profile of the Bessel beam at the peak threshold intensity ($\sim 3 \times 10^{12} \text{W}/\text{cm}^2$) with different laser energy is

shown for a laser pulse duration of 5.2 ps. The increment in experimentally observed structure length at higher energies evidence the nonlinear effects which prolong the focal volume.

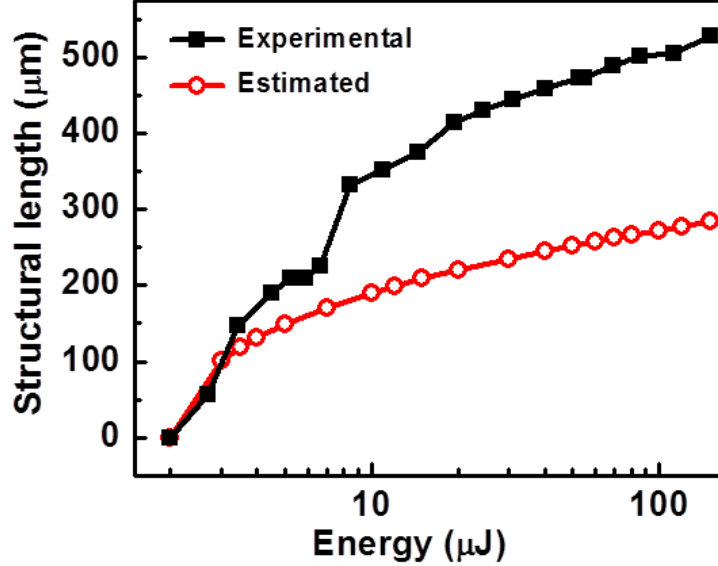


Figure 4.16: Plot of the modified structural length with the variation of laser energy for a laser pulse duration of 5.2 ps. Note the logarithmic scale of laser energy.

4.6 Different interaction regimes with laser pulse duration and energy

As we have seen, different interaction and stability regimes of the Bessel material interaction can be established depending on laser parameters. Here we summarized the different interaction regimes from the experimentally observed morphological changes. The laser energy (E) is varied (shown here up to 30 μJ only), over the range of laser pulse durations τ_P i.e. 60 fs – 5.7 ps and the results are shown in Fig. 4.17 (a), defining the four different regimes of structuring through shaded regions of the graph including measured error bars. Note that the bottom shaded border of Fig. 4.17 (a) represents the variation of laser damage threshold energy with respect to the laser pulse duration. Regime 1 refers to the structuring with short laser pulse duration, $\tau_P = 60$ fs to 1.7 ps, which results in type-I (only positive index modification) structure (see Fig. 4.17 (b) at low energy). For higher laser energies, this

structure develops into a combination of void and refractive index modified zone as nonlinear propagation plays a role. For instance, the structure machined in this regime at $E = 20 \mu\text{J}/\text{pulse}$ is shown in Fig. 4.17 (b) at high energy. It consists of alternatively placed index modification and voids with a periodicity in the range of 20 to 150 μm following unsteady focusing and defocusing cycles. Going to the ps pulse duration, regime 2 spans the energy

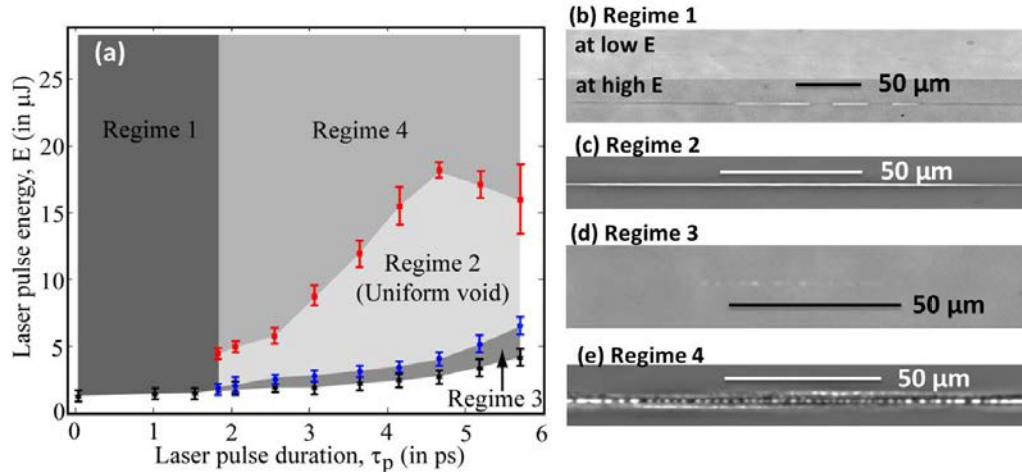


Figure 4.17: Summary of different interaction regimes using single-shot Bessel beams with various laser pulse energies and durations. Four different morphological regimes are highlighted (with shaded regimes) in Fig. (a). Typical structures in each respective regime are also shown in figures (b)–(e).

range $4.1 \mu\text{J} < E < 18 \mu\text{J}$, over which long uniform voids were observed like the one shown in Fig. 4.17 (c). At the low and high end of this energy range the situation changes. For instance, machining using laser pulses of 4.7 ps and in the laser energy range of $2.7 \mu\text{J} < E < 4.1 \mu\text{J}$, which can also be referred as the onset range, results in structures consisting of randomly arranged, non-uniform voids without having observable positive index modified zone; PCM image of a typical structure in this range is shown in Fig.4.17 (d). Such energy ranges corresponding to the considered laser pulse durations i.e. $1.7 \text{ ps} < \tau_p < 5.7 \text{ ps}$ are covered under Regime 3. Upon further increasing the laser energy i.e. $E > 18.0 \mu\text{J}$ (energies above the regime 2), a non-ordinary morphological characteristic was observed along the long axis of the structure; fragmented voids with a high quasi-periodicity (~ 3 to $6 \mu\text{m}$) at the middle of the structure, preceded and followed by long uniform voids were observed (see Fig. 4.17 (e), shown for $E \sim 54 \mu\text{J}/\text{pulse}$). Formation of such unique structures can be attributed to the interplay between complex nonlinear Bessel beam propagation and subsequent rapid material

relaxation dynamics in fused silica at relatively high laser energy, where hydrodynamic movement can interfere with the laser exposure. The energy ranges showing these kind of structures for all the considered pulse durations are covered under Regime 4. This detailed study give an overview of the stability conditions of the interaction at this moderate focusing conditions. For example, regime 2 is the stable interaction regime for ps pulse duration where we can have the uniform void structures. In the fs regime i.e, regime 1, stable interaction is possible until moderate energies ($E \sim 10 \mu\text{J}$) which results in uniform smooth refractive index type-I structures. Even if these results are permanent for a relatively moderate cone angle, major features can be encountered for other focusing conditions as well.

4.7 Nonlinear simulation results

When the ultrafast laser pulse traverses through the transparent media, pulse tends to be collapsed inside the media wherever the laser pulse energy exceeds the self focusing conditions and that mostly produces damage due to the nonlinear absorption. The electron population generated along the interaction volume in the first moments of the interaction may arrest the trailing edge of the pulse and redistribute the energy from propagation axis. Particularly, this interaction using non-diffractive (zeroth order Bessel) beams in fused silica is modeled using nonlinear envelope equation with details which were mentioned in the section 2.2.2. As we have seen earlier, unique material modifications are taking place depending on the laser pulse duration. The fundamental aspects of these interaction are studied numerically by taking into account basic processes occurring in the presence of a high laser field such as photoionization, free-carrier absorption, carrier-carrier interaction, as well as self-induced effects such as self-phase modulation or self-focusing, and plasma defocusing, which can dramatically effect the pulse propagation. Here, we discuss the numerical results of sequential energy deposition for femto and picosecond laser pulse durations at the same laser pulse energy. The sequential energy deposition inside the sample at different temporal slices of the pulse gives the insight into excitation processes concerning to the laser induced damage in both regimes. We considered the parameters which are involved in the equation 2.29 as: second-order group velocity dispersion in $a - \text{SiO}_2$, $k'' = 361 \text{ fs}^2/\text{cm}$; nonlinear refractive index as $n_2 = 2.48 \times 10^{-16} \text{ cm}^2/\text{W}$; intrinsic energy gap $E_{g0} = 9 \text{ eV}$; reduced mass of the electron and hole $m = 0.5 m_e$ [Ret04]; delayed Raman-Kerr optical response $f_R = 0.18$ [CSF⁺05]; carrier damping time $\tau_c = 0.5 \text{ fs}$. We note that particularly in the frame of a Drude model the momentum scattering time is a source of large

uncertainty and we will discuss the impact.

4.7.1 Simulation results in femtosecond regime

Figure 4.18 shows the dynamics of energy deposition into the electronic system i.e., the total energy deposited from the laser pulse in the Bessel interaction region for an ultrashort pulse duration of 60 fs at an input energy of 4.7 μJ . The laser pulse is divided into temporal slices (graphical representation is shown in figure) according to the integration times marked on the figure. The first approximation is that the simulations follow the manner in which the slices are sequentially deposited despite the fact that the simulations are made in a moving frame connected to the laser pulse. Additionally, part of the energy may already be transferred to the glass matrix on subpicosecond scales, determined by the fast electron trapping in SiO_2 . This effect is considered to be negligible during the fs exposure. The energy deposition in each temporal slice is as shown in Fig. 4.18 (a). From the energy deposition during each temporal slice, it is noticed that the maximum energy is deposited during the presence of leading edge of the pulse (first half of the pulse) and confined along the core of the Bessel beam. Notice that the efficiency of energy deposition on the propagation axis is decreased once the pulse of temporal slices crossing $\tau = 0$ (i.e., the passage of trailing edge) and energy is being defocused from on-axis. In Fig. 4.18 (b) it is shown the integrated deposited energy at the end of irradiation sequence of a laser pulse and defocusing of the deposited energy is clearly evident. The relative electron density at the end of the laser pulse is shown in Fig. 4.18 (c). The above simulation results indicate that the defocusing effect is a major phenomenon that leads to a lower energy deposition on the axis. The strength of defocusing depends on the radial carrier density profile, the level of electronic density and critically on the mass and scattering times for carriers. To understand qualitatively the role this defocusing effect over other nonlinear effects (eg. avalanche ionization), in the following we examine the role of these processes by cancelling part of the contributions.

Role of avalanche and plasma defocusing effects:

In fs regime, we try to understand the role of avalanche ionization and plasma defocusing for the effective energy deposition and free carrier generation which are responsible for the material modification. To examine the role of these effects, we avoided one of the terms (defocusing or avalanche ionization) in our nonlinear envelope equation 2.29 with including all other nonlinear effects. Simulation results with considering all the major nonlinear

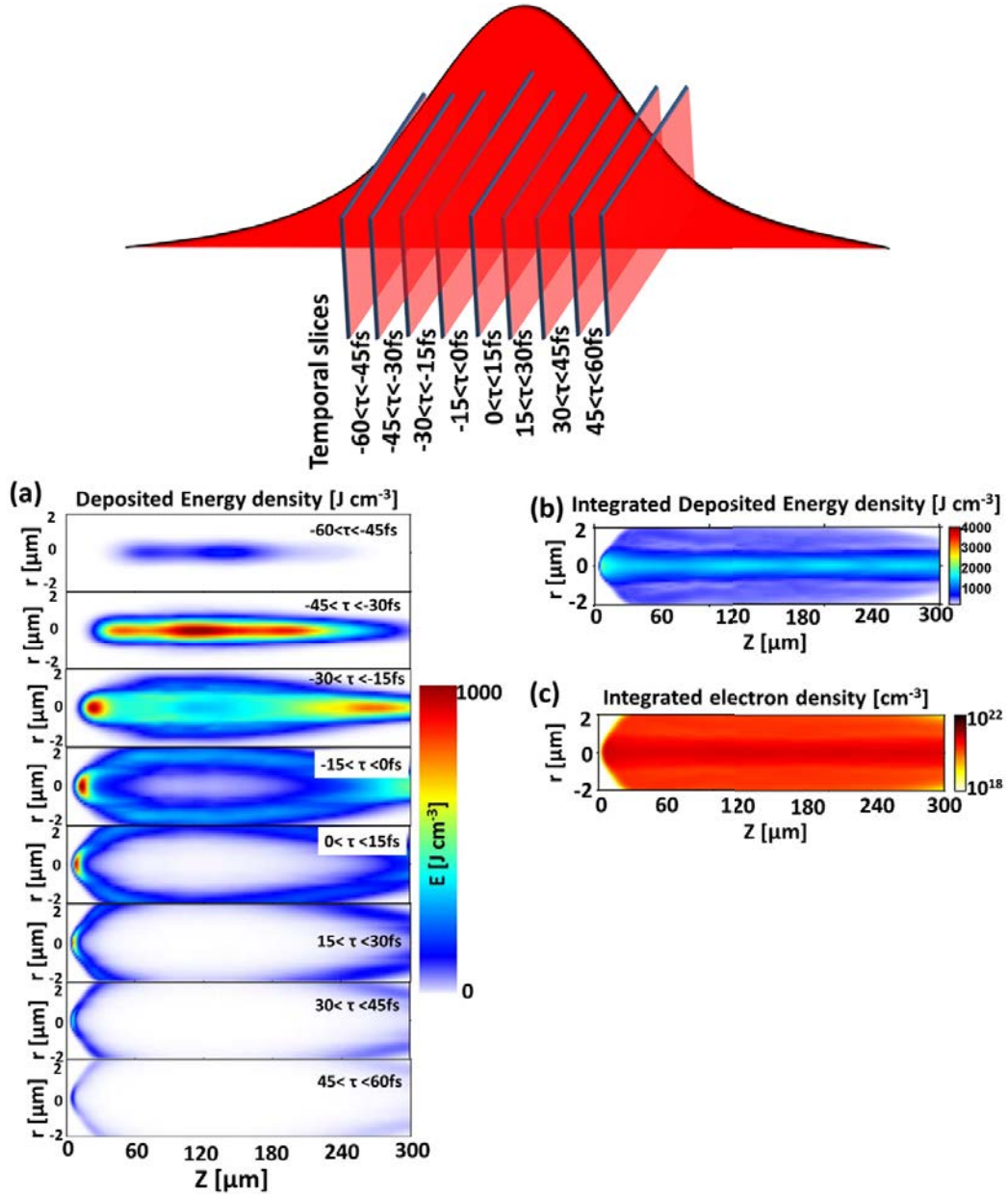


Figure 4.18: Simulation results of energy deposition at various temporal slices (shown in (a)) of the laser pulse duration of 60 fs and energy of $4.7 \mu\text{J}$. Also the integrated deposited energy and free carrier density at the end of pulse are shown in (b) and (c) respectively.

terms (including plasma defocusing and avalanche ionization) are shown in Fig. 4.19 (a). Simulation results without having the avalanche ionization

term are shown in Fig. 4.19 (b). Here the major role of plasma defocusing can be seen in spatial spread. It is worth noting though that all these effects are inter-related (e.g. via electronic density) and not independent. Simulation results without having the plasma defocusing term are shown in Fig. 4.19 (c). In this case, major role of avalanche ionization can be seen. We can draw some important conclusions and the role of avalanche ionization and plasma defocusing can be understood if we compare the results of integrated energy deposition and free carrier density in figures 4.19 (b) and 4.19 (c) with respect to Fig. 4.19 (a). The average energy deposition of the central core along the propagation axis for simulations with considering all the nonlinear effects is found to be lower (1400 J/cm^3) than without avalanche ionization (5360 J/cm^3) and plasma defocusing (5410 J/cm^3). This lower energy deposition in the case of considering the all nonlinear effects is due to the involving all nonlinear effects i.e., probably avalanche ionization could be also promoting efficiently the defocusing effects by multiplying the free carrier density. If there is no avalanche ionization i.e., considering only the presence of plasma defocusing effects lead to the lower energy deposition when compared with the neglecting plasma defocusing effects. From this measurements, role of plasma defocusing effect is clearly evident for an ultrashort laser pulse duration.

The effect of avalanche ionization on free carrier density can be also seen from the simulation results. If there is no avalanche ionization, the electron density is found to be low ($1.6 \times 10^{20}/\text{cm}^3$) even though there is a stronger energy deposition. If we do not consider the plasma defocusing, the carrier density found to be high ($1.74 \times 10^{21}/\text{cm}^3$). This higher carrier generation is due to the energy confinement (absence of defocusing effects) and the avalanche ionization. Here we recall again that the carrier densities found in our calculations may not give the accurate values because of the limitation of defining accurate band structure (the assumption of optical mass over the excitation range) and plasma damping characteristics but gives the indicative estimations. From the above theoretical investigations, it is found that two effects, plasma defocusing and avalanche ionization play a major role in energy deposition and carrier generation for an ultrashort laser pulse duration.

4.7.2 Simulation results in picosecond regime

Dynamics of energy deposition into the electronic system, integrated deposited energy and electron density at the end of laser pulse are shown in Fig. 4.20 in the Bessel interaction region for a ps laser pulse duration of 3.1 ps at an input energy of $4.7 \mu\text{J}$. To obtain the ps laser pulse duration,

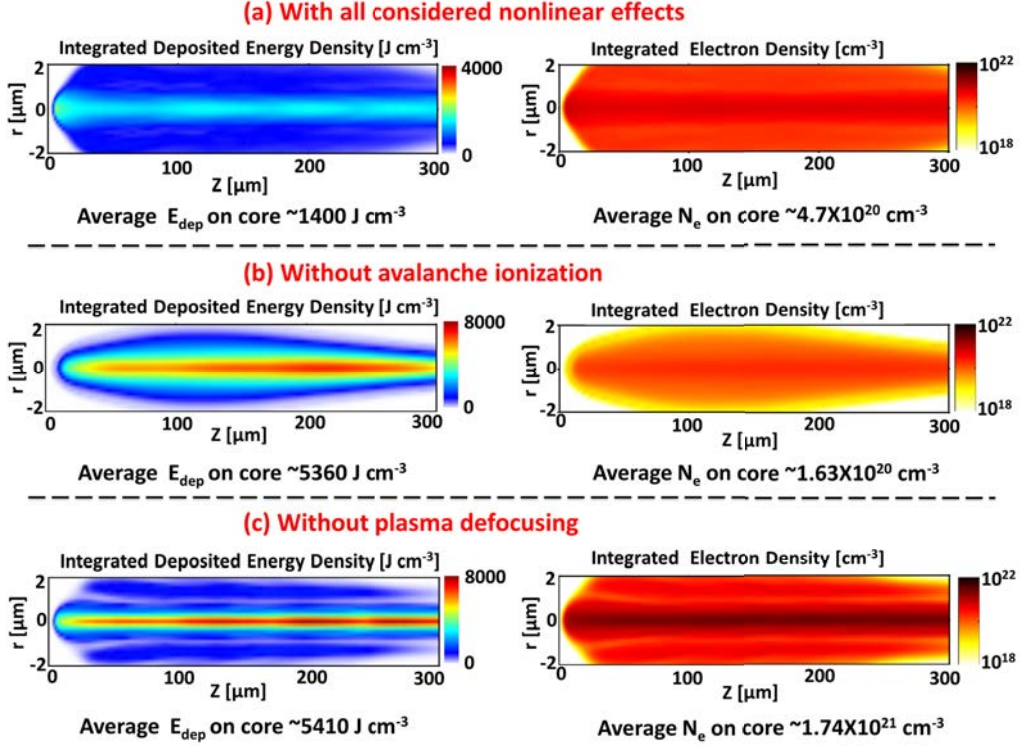


Figure 4.19: Role of the plasma defocusing and avalanche ionization on energy deposition and electron density integrated over all the temporal slices by end of the laser pulse duration of 60 fs and energy of $4.7 \mu\text{J}$. Figures in (a) show the simulation results with considering all the nonlinear effects. Figures in (b) show the simulation results without having the effect of avalanche ionization. Figures in (c) show the simulation results with out having the effect of plasma defocusing. Average energy deposition (E_{dep}) and free carrier density (N_e) values axially on the core are also shown. Note that in our simulations particularly in (b) and (c), we avoided chosen nonlinear effects: plasma defocusing or avalanche ionization as indicated in figure while all other nonlinear effects were considered.

the additional chirp was accounted for in the form proposed in [CFM⁺06]. The sequence of the processes that are followed for the energy deposition (energy deposition at each temporal slices) is as shown in Fig. 4.20 (a). We noticed that the energy is being deposited effectively around the center of the interaction volume during the first half of the pulse. As temporal slices of the trailing edge of the pulse are passing through the interaction volume, energy is being deposited effectively on edges of the interaction volume. The strength of the defocusing is found to be negligible in this case and a stronger

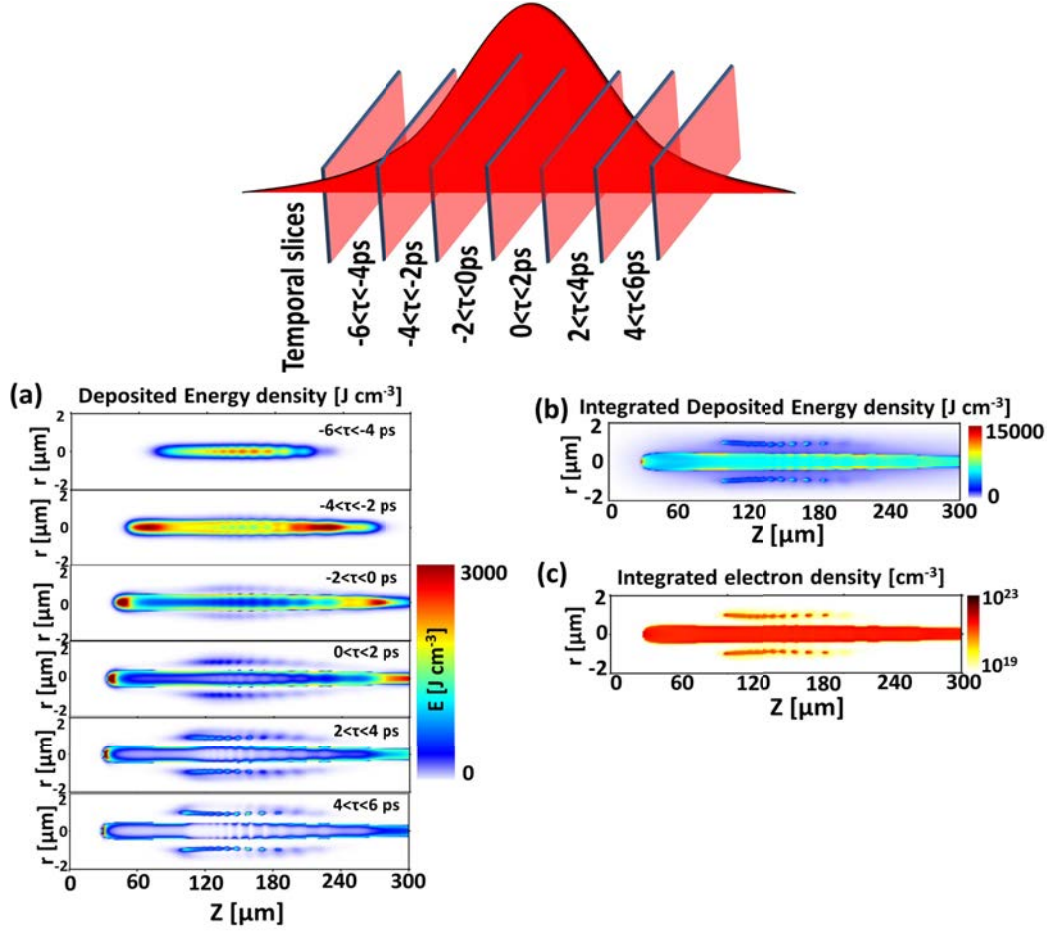


Figure 4.20: Simulation results of energy deposition at various temporal slices of the laser pulse duration of 3.1 ps and energy of 4.7 μJ are shown in (a). Integrated deposited energy and free carrier density at the end of pulse are also shown in (b) and (c) respectively.

confinement of the energy deposition is observed. The integrated energy deposition at the end of the laser pulse (integrated over all temporal slices) is as shown in Fig. 4.20 (b). Confinement of the deposited energy at the end of pulse is clearly evident and results in higher energy deposition. Corresponding integrated electron density at the end of the laser pulse (3.1 ps) is shown in Fig. 4.20 (c). As compared to the ultrashort pulse situation (60 fs), the deposited energy is more confined along the propagation axis and which consequently leads to a higher concentration of energy. Delayed photoionization mechanisms may offer the lower efficiency of the defocusing which leads to the stronger energy deposition and eventually lead to the higher car-

rier densities on the core. But here it is puzzling why high carrier densities though generated by delayed ionization mechanisms are not triggering the defocusing effects as in the case of fs. This is probably due to the ps pulse supporting an avalanche-like collisional carrier multiplication processes and resulting in highly peaked carrier densities on the axis. Thus the region over which light defocusing effects are at work might be restricted. We note that the influence of an eventual matrix heating and distortion during exposure is not accounted for in the transient optical properties. The main optical response is considered to be given by the electronic contribution. Nevertheless, the efficiency of the energy coupling may be further increased by eventual matrix distortions during the ps exposure. In the following, we examine the role of avalanche ionization for a ps laser pulse duration.

Role of avalanche ionization:

As we have seen, the efficiency of plasma defocusing in ps regime is low and leads to the energy confinement along the the core. In this regime, also it is important to know the role of avalanche ionization. To examine the role of avalanche ionization, we avoided the avalanche ionization term in our nonlinear envelope equation 2.29 with including all other nonlinear effects. Simulation results with considering all the major nonlinear terms (including plasma defocusing and avalanche ionization) are shown in Fig. 4.21 (a). Simulation results without having the avalanche ionization term are shown in Fig. 4.21 (b). The average energy deposition in the central core along the propagation axis for simulations with considering all the nonlinear effects is found to be higher (5800 J/cm^3) than without considering avalanche ionization (800 J/cm^3). The effect of avalanche ionization on free carrier density can be seen and major role in determining sufficient enough electronic populations to support carrier heating. If there is no avalanche ionization, the electron density is found to be very low ($2.5 \times 10^{16}/\text{cm}^3$) compared to the case of including all nonlinear effects ($2.2 \times 10^{21}/\text{cm}^3$). It can be noticed that the absence of avalanche ionization is leading to lower carrier generation. This result gives an evidence that in ps regime, avalanche ionization could be potentially playing a major role to produce the higher carrier density, as MPI is weak in this case because of poor intensities. The direct role is self-explaining seeded collisional multiplication, but the indirect control is equally important by influencing carrier light defocusing and carrier profiles.

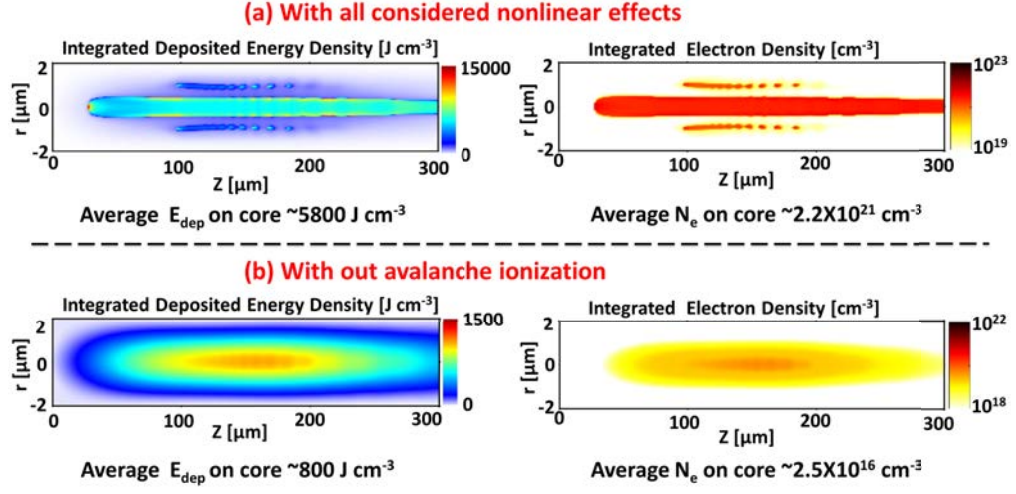


Figure 4.21: Role of the avalanche ionization on energy deposition and electron density integrated over all the temporal slices by end of the laser pulse duration of 3.1 ps and energy of 4.7 μJ . Figures in (a) show the simulation results with considering all the nonlinear effects. Figures in (b) show the simulation results with out having the effect of avalanche ionization. Average energy deposition (E_{dep}) and free carrier density (N_e) values on core are also shown. Note that in our simulations particularly in (b), we avoided the effect of avalanche ionization as indicated in figure and all other nonlinear effects were considered.

4.7.3 Energy deposition per electron

Electron densities generated by various photoionization mechanisms at first instant of the pulse consequently define the rest of the pulse interaction. It will be interesting to know the energy deposition per electron which provide the initial stages of the interaction. We estimated the energy deposition per electron on the core for both fs and ps pulse duration from simulation results. Fig. 4.22 (a) and (b) shows the energy deposition per electron on core along the longitudinal distance for 60 fs and 3.1 ps respectively. We noticed that the slightly more energy deposition per electron occurs in fs case (varied around 18 eV) compared to the ps case (varied around 17 eV). This is indicating that per electron, the efficiency of instant photoionization mechanisms are slightly more prominent in fs pulse duration compared to the ps regime. As we have seen, fs regime imposed to defocusing effects which lead to the inefficient energy deposition with the growing carrier density. In ps regime, even though energy deposition per electron is lower of ~ 1 eV compared to the fs case, inefficient defocusing effects lead to the stronger

energy deposition.

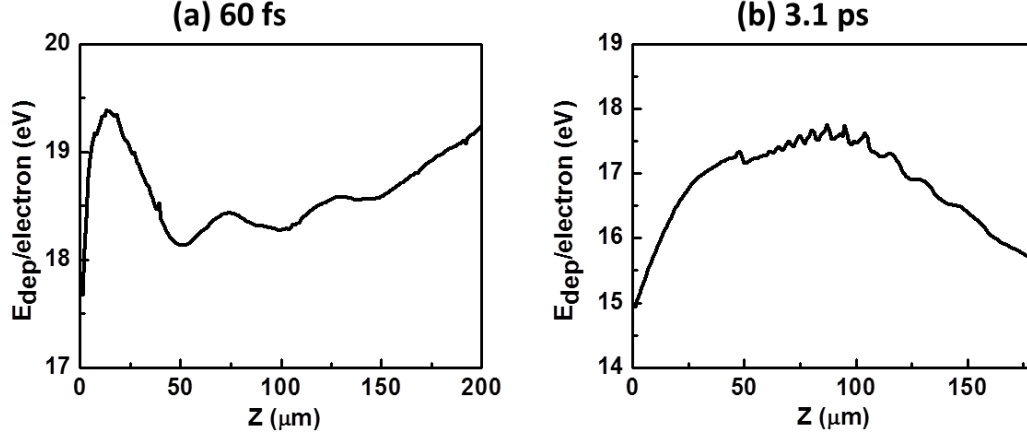


Figure 4.22: Simulation results of energy deposition (E_{dep}) per electron for the laser pulse durations (a) 60 fs and (b) 3.1 ps at laser pulse energy of $4.7 \mu\text{J}$

4.7.4 Role of free carrier damping time

As free carrier damping time is one of the major parameters that define the damping characteristics of the free carriers, choosing an appropriate value is a challenging task. Consequently, carrier damping time play a major role in estimation of energy deposition and free carrier density. In this section, we show the role of carrier damping time on energy deposition and related carrier density. The values of energy deposition (E_{dep}) and carrier density (N_e) are averaged along the core. The variation of E_{dep} and N_e as a function of the damping time for a laser pulse duration of 60 fs and energy of $6 \mu\text{J}$ is shown in Fig. 4.23 (a) and (b) respectively. The variation of E_{dep} and N_e as a function of damping time for a laser pulse duration of 3.1 ps and $6 \mu\text{J}$ is shown in Fig. 4.24 (a) and (b) respectively. We observed for the both pulse durations, a decrement in E_{dep} and N_e with increasing the damping time excepts τ at 0.01 fs for ps laser pulse duration.

4.7.5 Discussion: simulation results

The above simulation results in fs and ps regimes offer insights in understanding of the formation scenarios of positive index and void structures respectively. A steep increase in the laser energy density deposited along the central core (i.e., on-axis) of the Bessel beam inside fused silica is observed

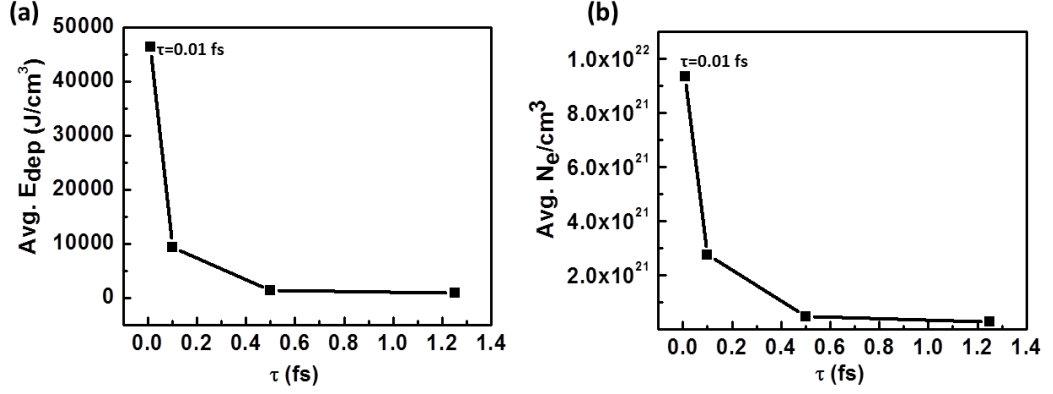


Figure 4.23: Simulation results of average energy deposition (a) and carrier density (b) on the core as a function of carrier damping time (τ) for a laser pulse duration of 60 fs and energy of 6 μJ . τ values are highlighted where the values are unclear.

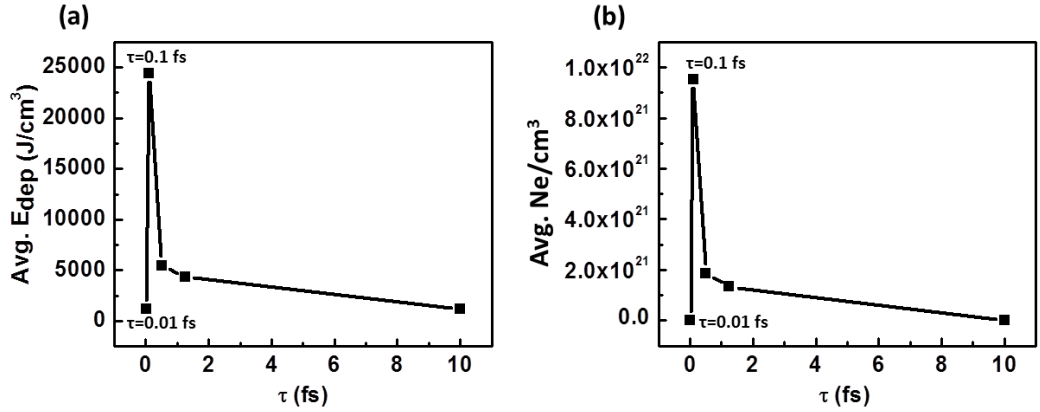


Figure 4.24: Simulation results of average energy deposition (a) and carrier density (b) on the core as a function of carrier damping time (τ) for a laser pulse duration of 3.1 ps and energy of 6 μJ . τ values are highlighted where the values are unclear.

when using a laser pulse of a relatively longer temporal duration (i.e., 3.1 ps) compared to the Fourier transform-limited pulse (i.e., 60 fs). Precisely we observed that the energy deposition in ps case (average E_{dep} on core $\sim 5800 \text{ J/cm}^3$) is four times higher than the fs laser pulse (average E_{dep} on core $\sim 1400 \text{ J/cm}^3$) at similar conditions. Also noticed nearly one order magnitude of higher electron density in the case of ps (average N_e on core $2.2 \times 10^{21}/\text{cm}^3$) compared to fs case (average N_e on core $4.7 \times 10^{20}/\text{cm}^3$). Here we anticipate that the laser pulse of short temporal duration can trig-

ger significant MPI, generating free electrons at the beginning of the pulse, which would ultimately defocus the rest of the laser pulse, suppressing the income of laser energy along the axis. Indeed, many focusing-defocusing cycles have been observed earlier in the case of Bessel beam interaction with condensed media [PFC⁺08, GVJ⁺06] with a defocusing strength depending on the damping characteristics of the carrier plasma. On the contrary, for laser pulse of longer temporal duration, as the carrier generation is less swift and it is radially peaked on the axis, the relatively low efficiency of plasma defocusing allows concentrating axial energy, leading to a strong accumulation of excitation density. Even though the quantitative effects are effected by the choice of τ , it is instructive to calculate energy transfer as it reflect the follow-up experimental observations. The rise in temperature (ΔT) in the photoexcited volume can be estimated from the deposited energy density as $\Delta T = E_{dep}/C_p\rho$, where E_{dep} is the deposited laser energy density, ρ and C_p are the solid density (2200 kg/m^3) and specific heat capacity (740 J/kg/K) of fused silica, respectively. In the case fs laser pulse, the rise in temperature is in the focal volume found to be $\sim 800\text{ K}$, which is well below the softening temperature of the fused silica ($\sim 1500\text{--}1700\text{ K}$). This indicates that the non-thermal driven mechanisms are leading to formation of smooth refractive index structures. The rise in temperature for ps laser pulse duration found to be ($\sim 3600\text{ K}$) higher than softening value. This indicates that thermodynamically driven mechanisms lead to the formation of voids by steering phase transitions. The strong confinement of the laser deposited energy on the axis leads to the hydrodynamic movement in the excited region; a pressure wave due to high pressure and temperature is released out of the excited volume. The subsequent rarefaction leads to a cavitation and leaves behind a low density zone.

4.8 Conclusions

In conclusion, we have presented a study on fabrication of high aspect ratio sub-micron structuring in fused silica using ultrafast laser Bessel beams. Role of focusing conditions on stability of the interaction in terms of structural modification is evaluated. For a fixed focusing geometry, the laser pulse duration was observed to play a key role in the process of nonlinear propagation of Bessel beams, depositing the laser energy axially in the medium with controllable efficiency. Two peculiar photoinscription regimes, resulting in uniform positive refractive index modified structures and high aspect ratio void structures in fused silica, have been identified. We have explored the different interaction regimes by changing the laser parameters (pulse duration

and energy) at same focusing conditions. Stable propagation of the Bessel beams has been found over a range of laser pulse duration and energy, resulting in uniform structural modifications. Also, we performed the simulation results to understand the propagation in fused silica in terms of sequential energy deposition. The confinement of the energy deposition in picosecond regime leads to the higher energy density on the propagation axis. This stronger energy deposition leads to the hydrodynamic expansion resulting in uniform voids where as the scattering-limited energy deposition leads to the formation of smooth positive refractive index structures via presumably non-thermal structural transitions in the femtosecond case.

Chapter 5

Role of instantaneous (peak) Bessel excitation for material modification

As we have seen in the last chapter, material modification depends on the laser pulse duration and the energy at a fixed cone angle. To understand the formation of the different structural morphologies, this chapter is focused on the role of instantaneous maximal Bessel excitation on the material modification with respect to the laser parameters using instantaneous pump-probe microscopy. In this chapter, first we briefly outline the overview of time-resolved (pump-probe) studies for laser material processing. Then we explore the role of pulse duration on instantaneous maximal carrier generation for formation of smooth index and void structures. Also the role of laser energy on instantaneous carrier generation in both femtosecond and picosecond regimes is investigated. Next, we present the integrated plasma luminescence imaging as a function of laser energy in both pulse duration regimes which offers indirectly the spatially resolved electron energy distribution in different interaction conditions. Finally, we investigate the role of probe wavelength and polarization on instantaneous transmission. Probing the instantaneous transmission due to free carriers at two different wavelengths provides the additional information on plasma damping characteristics.

5.1 Overview: Time-resolved studies for laser material processing

Since last two decades, fs lasers have found special attention in laser-material processing applications because of its confinement and localization even be-

yond the diffraction limit by nonlinear means. This unique signature offers a strong potential for structuring materials on micro and nano scales for several applications including future lab-on-a chip based 3-D photonic devices [TBLS⁺11, CRO⁺11, SSV⁺12, SSV⁺10]. As we discussed already in chapter 4, the importance of zeroth-order Bessel beams over Gaussian laser beams is obvious for rapid and high aspect ratio sub-micron structuring. Understanding of the dynamics and formation mechanisms of laser induced structures in non-propagative regimes are necessary to achieve better control over energy deposition, improving process quality and precision in laser induced volume structuring at the resolution limit. We study the role of instantaneous excitation and relaxation dynamics using non-diffractive ultrafast laser beams and the consequences on the morphology of material modification in bulk a-SiO₂. The amplitude and phase characteristics of the excited regions with sub-picosecond temporal and sub-micrometer spatial resolution, address the questions related to potential relaxation paths via structural transitions around local defect generation, or macroscopic thermodynamic events. These studies are split into two chapters (Chapter-5 and Chapter-6). This chapter (Chapter-5) describes the role of instantaneous excitation (carrier density) at the peak and plasma luminescence studies. Next chapter (Chapter-6) addresses the complete relaxation dynamics following the excitation and outlines the formation mechanisms of high-aspect ratio sub-micron structures.

Chapter-5 and chapter-6 provide a new set of experiments for the first time to attempt the understanding of material interaction dynamics on ultrafast scales in non-diffractive interaction regime related to high aspect ratio sub-micron structures. Previously, majority of the experiments have studied the transient dynamics of material modification using pump-probe setup with fs laser Gaussian beams. Particularly, collinear pump-probe beams have been successfully employed. For instance, transmission and reflection based techniques [WBS⁺06, MSZR05, CXW05] and transient lens method [ST05] are used. Moving to the more complex setups, spectral interferometry is used to obtain relative transient phase changes based on interference patterns of reference and probe pulses with and without having excitation in collinear and also possibility with perpendicular geometries [Mou13]. In this collinear geometry, major advantage of the setup is temporal resolution (nearly same as laser pulse duration) but the transient information is integrated over the probe propagation along the entire sample thickness. To improve the spatial resolution, off-axis digital holography techniques [BMTS08] and other perpendicular geometry based techniques (pump and probe beams propagate perpendicularly at the interaction volume) have been proposed [SJL⁺05, Hor03, KHP05, HKP04, PZT07]. In this thesis, we use a microscopy technique in perpendicular geometry (similar to [Mau10, MB07])

that allows the time-resolved observations in optical transmission as well as in phase contrast with a spatial resolution limited by characteristics of our microscope and a sub-picosecond temporal resolution. Experimental details of the pump-probe microscopy are discussed in the section 3.2.2.

As we already mention that this chapter discusses the role of instantaneous excitation, we first examine the role of pulse duration dependent material modification in terms of instantaneous excitation at the peak. In the following section, we present the effectiveness of free carrier generation versus laser pulse duration in non-diffractive conditions which significantly defines the type of material modification at same laser pulse energy.

5.2 Role of laser pulse duration on free carrier generation

As we have seen in the section 4.3, the laser pulse duration is a key in deciding the type of structural modification at same focusing geometry and laser pulse energy. Bessel excitation with the fs laser pulse results in smooth positive refractive index structures while the ps laser pulse results in void-like structures. Fig. 5.1 (a) shows PCM images of typical single-pulse structures produced in fused silica using laser pulse energy (E) = 6 μ J and different pulse durations, characterizing the onset of two modification regimes, positive index type-I and negative index type-II. Transformation of the machined structure from uniform positive refractive index zone to a low refractive index zone (void-like domains) when linearly chirping the laser pulse from fs to ps duration is clearly evident from Fig. 5.1 (a). In the present case, the transition from a type-I to a type-II structure occurs at laser pulse duration of ~ 1.8 ps for an energy of 6 μ J/pulse. In order to understand the mechanisms behind laser pulse duration dependent transitional behavior of the structures i.e., the transformation from positive to negative refractive index modified zones and the further deterioration in their structural uniformity, time resolved studies were performed. Particularly, in this subsection, results of instantaneous (peak) excitation characteristics are discussed.

Fig. 5.1 (b) shows the instantaneous optical transmission microscopy images of the Bessel beam excited region of the material at zero delay i.e. where pump and probe temporally overlap, resulting in maximum free carrier absorption, for selected laser pulse durations and $E = 6$ μ J/pulse. For the sake of simplicity, only central portions of the excited region of the material are imaged and shown as representative to reveal the ultrafast profiles. The contribution of the free carriers to the transient optical transmission

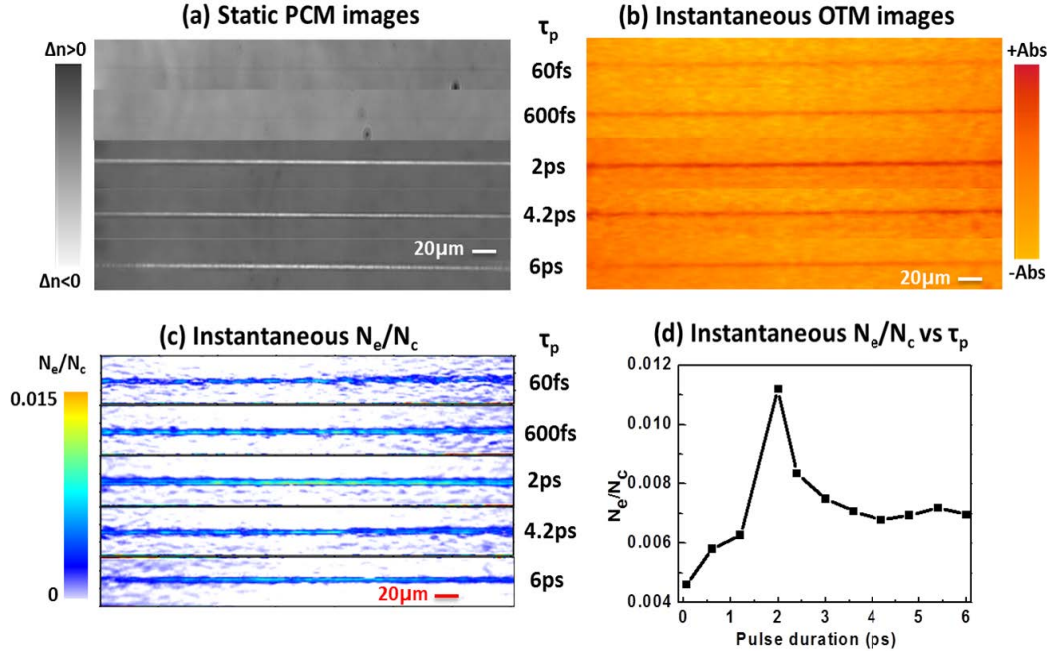


Figure 5.1: Phase contrast microscopy (PCM) images of Bessel beam induced high aspect ratio permanent structures in fused silica using single laser pulses of energy $E = 6 \mu\text{J}$ at different pulse durations are shown in (a). Their corresponding instantaneous optical transmission, peak free carrier density (normalized to critical density) estimation with projection correction and variation of carrier density normalized to critical density with laser pulse duration (τ_p) are shown in (b), (c) and (d) respectively. Note here that only central portions of the excited region are shown in images as a representative.

can be estimated using the Eqn. 2.15 based on the transmission at each pulse duration. In real practice, the captured OTM images are the projected images of non-monotonous radial profiles on to the image plane. Therefore, it is necessary to reconstruct the excitation profiles from the projected images for the evaluation of precise free carrier density. This reconstruction can be done numerically by means of inverse Abel transform. We used the Fourier expansion based algorithm for inverse Abel transform and the formalism is discussed in Appendix A. The relative density $\frac{N_e}{N_c}$ distribution (where N_c represent the critical density at the probing wavelength i.e., 400 nm) along the structure length is estimated and carrier density profiles are shown in Fig. 5.1 (c). We recall that ambiguities in carrier properties associated with defining the accurate values of carrier optical mass and damping time with energy, probe scattering effects, allow only an approximate, indicative, estimation within an order of magnitude tolerance. It is observable from the figures 5.1 (b) and (c) that the matter excited with the laser pulse (pump pulse, $E = 6 \mu\text{J}$) of shortest pulse duration ($\tau_p = 60 \text{ fs}$) only weakly absorbs the probe pulse compared to the case of excitation with pump pulse of $\tau_p = 2 \text{ ps}$. This indicates the generation of larger number of free carriers (or generally a higher excitation quantity) in the ps laser excitation process.

The results of a systematic study on the laser-induced carrier generation inside fused silica as a function of laser pulse duration in the range $60 \text{ fs} - 6 \text{ ps}$ are summarized in Fig. 5.1 (d). It appears from the figure that the excitation density goes up with increasing laser pulse duration until its maximum value at $\tau_p = 2 \text{ ps}$. Upon further increase in the laser pulse duration, the carrier density starts to decrease. These results can be usefully compared to the results presented in Fig. 5.1 (a); the regimes where carrier number density is observed to be minimum and maximum produce uniform positive and negative refractive index structures respectively. Clearly, type-I structures are observed when the free carrier density (see Fig. 5.1 (c) for $\tau_p = 60 \text{ fs}$ and 600 fs) is minimal whereas void-like i.e., type-II structures are observed for maximal carrier density. A deterioration in the quality of the structure in terms of the uniformity of void-like domains was observed when machining using laser pulses of relatively longer duration. For example, a structure machined using $\tau_p = 6 \text{ ps}$ as depicted in Fig. 5.1 (a) shows a spatial modulation, specially towards their edges due to a decrease of ionization efficiency and resulting lower free carrier density compared to the uniform void at 2 ps . This is evident from the instantaneous carrier density (from the Fig. 5.1 (c) for 6 ps laser pulse duration). These results provide an indication that the carrier number density and the associated energy deposition may define the kind of material relaxation path and therefore the ultimate material phase transformation.

5.3 Role of laser energy on free carrier generation

As we have seen from the simulation results (in section 4.7), pulse duration plays a major role in depositing the laser energy axially. We recall here, plasma defocusing effect in fs regime leads to the lower energy deposition whereas low efficiency of plasma defocusing in ps regime leads to the confinement of energy on axis resulting in higher energy deposition. In ultrafast laser-matter interactions, particularly with transparent materials, the laser energy is being deposited to the matter through the generation of free carriers by nonlinear means and then transportation of energy from free carriers to matrix is taking place at later times of the interaction. Therefore study of the free carrier generation, its growth and behavior with laser energy in both fs and ps regimes is necessary to understand the fundamental aspect of the interaction such as energy deposition which is a crucial mechanism for structural modifications.

In the following, we estimate the generated instantaneous free carrier density and study the role of laser energy on free carrier generation in both fs and ps regimes. We captured the instantaneous transmission images (at zero delay where pump and probe overlap and resulting in maximum plasma absorption) at various laser pulse energies and estimated the free carrier density based on transmission data treated in the frame of a Drude formalism.

Femtosecond regime

The instantaneous optical transmission images (at zero delay) for fs laser pulse duration (60 fs) at various laser pulse energies (up to $\sim 100 \mu\text{J}$) are shown in Fig. 5.2. In the OTM images, darker regions indicate the free carrier absorption regions. The instantaneous absorption increases with the laser pulse energy and saturates at higher energies. It can be noticed from OTM images that the scattering/absorption away from propagation axis is increased with the laser energy. This scattering away from the propagation axis is attributed to the defocusing effects or excitation on the wings of conical beam and these effects can be clearly seen at higher energies because of their higher efficiency. Also here it is important to note that the size (cross-section) of the plasma including the scattered region is higher than the cross-section of static structural modifications, evidencing the possibility of defocusing effects. The transmittance and absorbance curves are shown in Fig. 5.3 (a). Also the relative free carrier density is estimated and variation of free carrier density normalized to a critical density with energy is as shown in 5.3 (b). From these figures, increase in absorption or carrier density (decrease of

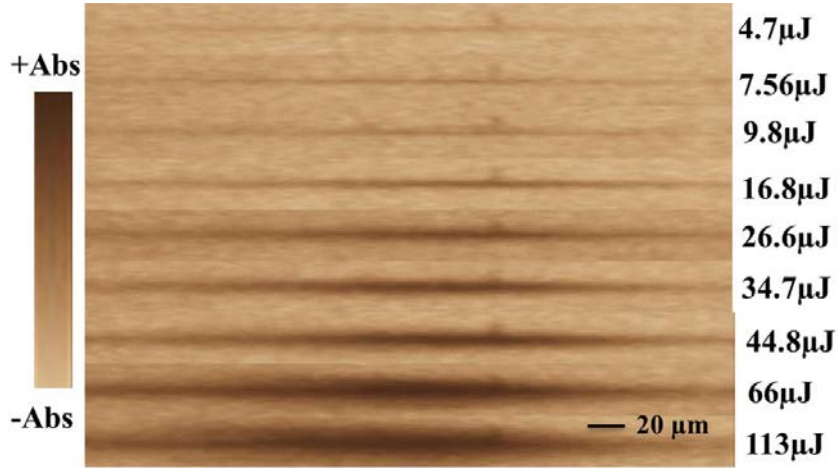


Figure 5.2: Instantaneous optical transmission images at selective laser pulse energies for a single laser pulse duration of 60 fs.

transmission) is clearly evident until $\sim 60 \mu\text{J}$ and a saturation regime follows.

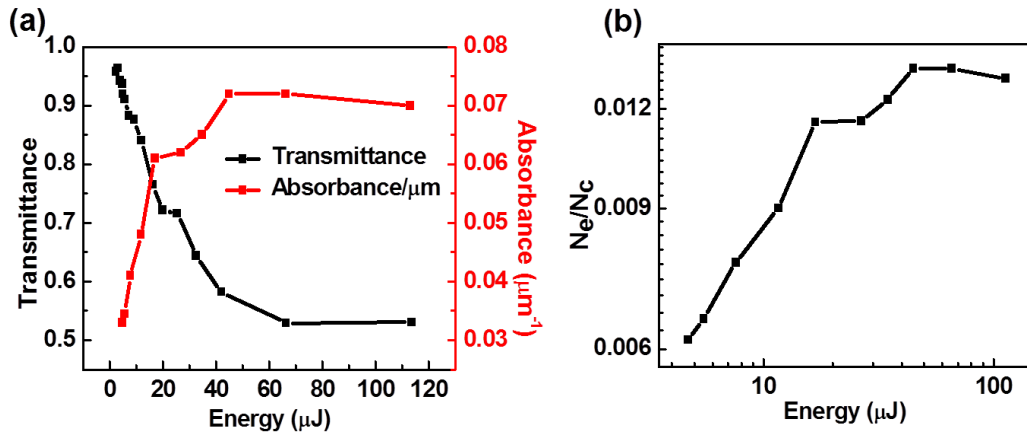


Figure 5.3: (a) Instantaneous transmission (left scale) and absorbance (right scale) as a function of laser energy, (b) The relative free carrier density variation with laser energy for a single laser pulse duration of 60 fs. Note the logarithmic scale.

Picosecond regime

The instantaneous OTM images for a ps laser pulse duration (4.2 ps) at different energies are shown in Fig. 5.4. Gradual increase in absorption due to

the free carriers has been observed with the laser energy. Also confinement of the plasma absorption along the propagation axis is observed. Transmission

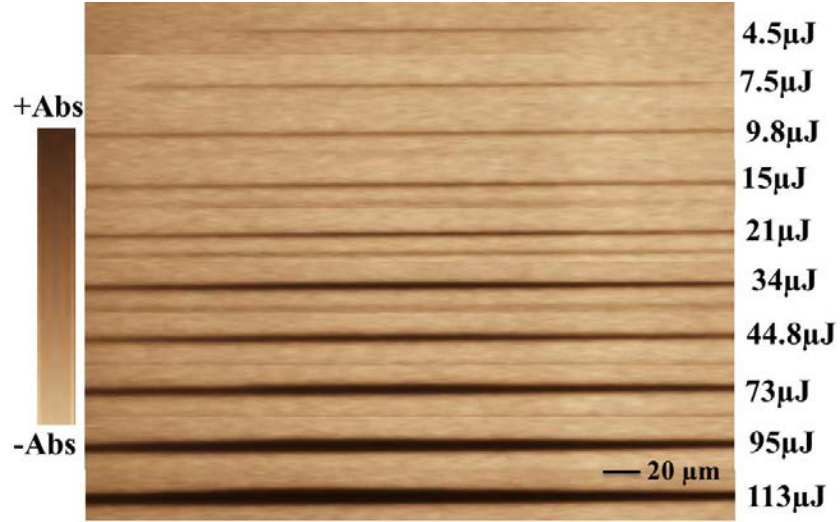


Figure 5.4: Instantaneous optical transmission images at various laser pulse energies for a single laser pulse duration of 4.2 ps.

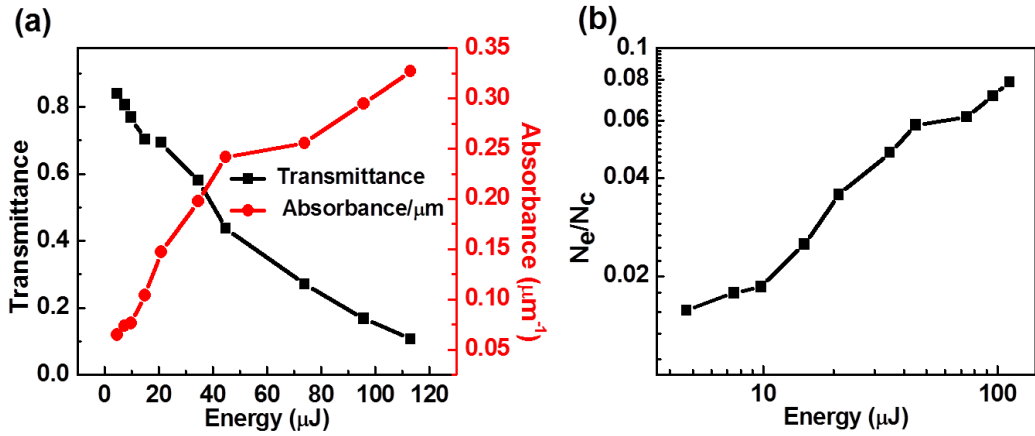


Figure 5.5: (a) Instantaneous peak transmission (left scale) and absorbance (right scale) as a function of laser energy, (b) The relative free carrier density variation with laser energy for a laser pulse duration of 4.2 ps. Note the logarithmic scale.

and absorbance plots are shown in Fig. 5.5 (a). The increase in absorbance (decrease in transmission) can be seen even at higher energies. The respective free carrier density is estimated in ps regime and variation of carrier density

over a critical density (N_e/N_c) is shown in Fig. 5.5 (b). Also from this plot, growth in free carrier density with energy is also evident.

Monitoring the relative behavior, the excitation density is observed to be higher in the case of ps than in the case of fs Bessel beam excitation process. The difference between the fs and ps cases in carrier generation with energy can be clearly seen from the Fig. 5.6. In particular, a power law growth of carrier density is observable at lower laser energies in both fs and ps excitation processes. On the other hand, while the carrier density starts to be saturated in the fs regime (i.e. $\tau_p = 60 \text{ fs}$) due to intensity clamping, growth in carrier density is still maintained in the case of ps excitation (i.e. $\tau_p = 4.2 \text{ ps}$) at higher laser energies. This behavior can be explained in

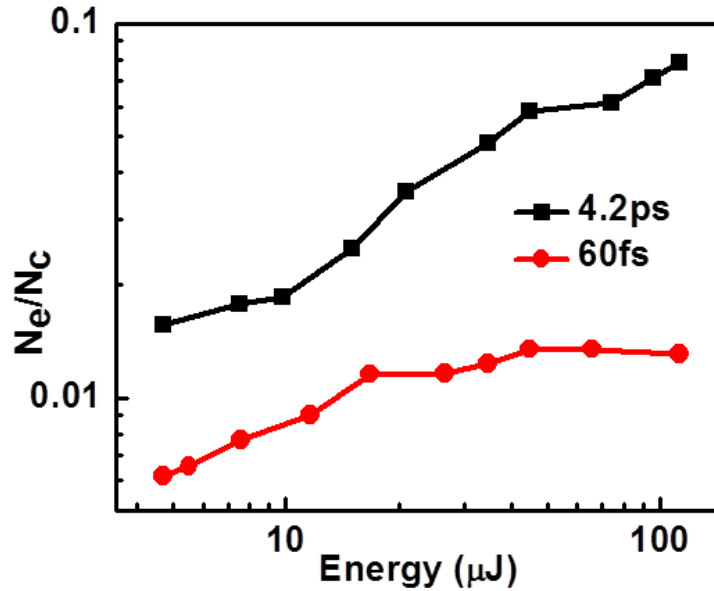


Figure 5.6: Variation of instantaneous free carrier density normalized to the critical density at 400 nm for various laser pulse energies in both pulse duration regimes 60 fs and 4.2 ps. Note the logarithmic scale. Comparison in generation of free carrier density between in each case is clearly evident.

terms of the defocusing strength of the laser-induced free carriers in the material. We recall here, in the case of fs laser pulse excitation, a significant amount of free carriers, mainly due to MPI, can be generated in the first part of the laser pulse, which would defocus the rest of the pulse. Indeed, our instantaneous OTM profiles evidence the defocusing effect in fs regime in agreement with the simulation results (see the section 4.7) which show the consequence of such carrier diffusion effect, restricting the on-axis laser energy deposition inside the material. As the laser energy is increased, free

carriers are generated earlier in time than in the case of excitation at low laser energy, which would diffuse the rest of the pulse as usual. As a result, the carrier number density remains nearly constant with the input energy even in case of matter excitation with very high laser energy ($E \geq 100 \mu J/pulse$). On the contrary, in the case of ps laser excitation, despite a lower efficiency of MPI in generating free carriers, the energy is not diffused away and is used to further promote the ionization process. The onset of collisional multiplication creating narrow excitation profiles is equally contributing to lower defocusing effect. Therefore, due to delayed ionization processes and low defocusing, free carrier densities are increasing with laser energy over our considered range. Also simulation results evidenced the confinement of the laser energy along the propagation axis in ps regime.

5.4 Plasma luminescence studies

We discuss here a preliminary view on excitation using plasma luminescence studies. In dense collisional plasma produced by the intense laser excitation, the free electrons exchange photons with the laser field. When energetic free electrons are accelerated in the Coulomb field of the ions, they emit photons, by a Bremsstrahlung process. Since the acceleration is not uniform and affected by collision, the emitted spectrum is large. Effectively, plasma results in broad luminescence (in our case $\sim 400 - 700 \text{ nm}$) and the characteristics of this luminescence is depending on the free electron or carrier density and temperature. Plasma luminescence measurements indirectly provide the information of the electron energy distribution in the excitation volume. The electron energy distribution in plasma can be estimated simply from a kinetic theory using Maxwell-Boltzmann distribution. The distribution function in terms of electron kinetic energy (E_K) can be expressed as:

$$f(E_k) = 2n \sqrt{\frac{E_K}{\pi(kT)^3}} \exp\left(-\frac{E_K}{kT}\right) \quad (5.1)$$

The above distribution function is characterized by two parameters: electron density n and temperature T .

As relative plasma luminescence with the laser energy is a consequence of the free carrier generation and energy deposition to the electronic gas, we measured the single pulse plasma luminescence due to the Bessel excitation to have view on the results of excitation. The integrated spectrally unresolved plasma luminescence (integrated over 1 ms of exposure time of EMCCD camera larger than the expected life-time of the plasma) studies in fs and

ps pulse duration interaction regimes with the function of laser energy are presented in the following sections.

5.4.1 Femtosecond regime

Single pulse plasma luminescence studies in fs regime (60 fs) are shown in Fig. 5.7. The spatial profiles of the plasma luminescence along the structural length are shown in Fig. 5.7 (a). Only the center part of plasma luminescence profiles are shown. Stable plasma luminescence is observed at lower energies, until the energies ($\sim 12 \mu\text{J}$) where we have the uniform smooth refractive index structures (as we discussed in chapter 4). This uniform plasma luminescence could be due to the stable filament. As we increase the laser pulse energy ($\geq 20 \mu\text{J}$), we noticed the non-uniformity in plasma luminescence. This could be due to with high probability the onset of instability in filamentation. For instance, relative structural morphology (PCM image) for an unstable regime at $32.7 \mu\text{J}$ is shown in Fig. 5.7 (b). It can be noticed that the maximum plasma luminescence regions result in void-like structural modification regions. Modulations in plasma luminescence such as consecutive bright and dark regions indicates the nonuniform distribution of carrier densities with probably the different relaxation paths resulting in modulated contrast in integrated plasma luminescence profiles. We recall here again, at higher energies, only the center part of excitation profiles are covered in the image. With increasing of laser energy, the intensity counts of the plasma luminescence increases. The variation of peak intensity counts of the plasma luminescence with energy is depicted in Fig. 5.7 (c). We note here an unsaturated behavior in contrast to the expected leveling in electron concentration suggesting local energy gains and a need for spectral imaging.

Longitudinal profiles (line-profiles) along the central core of the plasma luminescence are shown in Fig. 5.8. The spatial modulations in the plasma luminescence profiles are clearly evident with the laser energy. The longitudinal profiles around the lower energies are shown in right side in the inset enlarging the minute variations. The Bessel profile is shown with dotted lines. Increasing of repetitive modulations with laser energy can be also clearly seen which probably due to the enhancement of instabilities in filamentation. We equally observe, without giving an explanation, regions with low luminescence still giving permanent modifications. A full explanation would involve dynamic photoluminescence studies, a perspective for this work.

In order to understand the instabilities in plasma luminescence with increasing of laser energy, we compare the plasma luminescence profiles with longitudinal profiles of the estimated instantaneous carrier density derived from instantaneous OTM images. Longitudinal carrier density profiles along

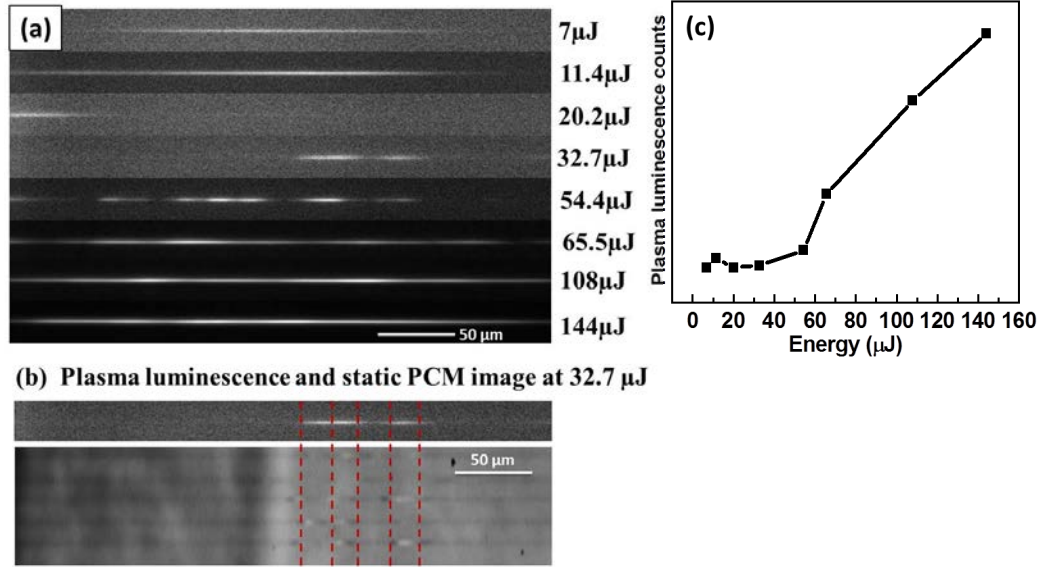


Figure 5.7: Plasma luminescence studies inside the fused silica using a single pulse with duration of 60 fs. (a) Plasma luminescence profiles at selective laser pulse energies. Relative brightness in the images indicates the contrast of plasma luminescence. (b) Plasma luminescence and static PCM structures at 32.7 μJ indicating the structural morphology related to the shown plasma luminescence. (c) Variation of plasma luminescence in terms of the intensity counts with the laser pulse energy.

the core at specific energies are shown in Fig. 5.9. As compared with longitudinal profiles of plasma luminescence, we did not observe any modulations in instantaneous carrier generation along the core. Saturation in carrier density at higher energies can be clearly seen which is evidencing the intensity clamping in fs regime.

Even in the absence of spectrally resolved, dynamic luminescence studies; comparison of integrated plasma luminescence profiles with the instantaneous carrier density in fs regime can reveal the interesting conclusions. Particularly, repetitive modulations in plasma luminescence are observed in fs case. This modulations could be due to the higher defocusing effects which are leading to the unstable filaments with increasing energy. We note however that the instantaneous free carriers profiles with energy are found to be smoother. This difference between the plasma luminescence and instantaneous free carrier distribution can be understood by the following involved possible mechanisms:

- Slight nonuniform carrier density regimes with a different characteristic

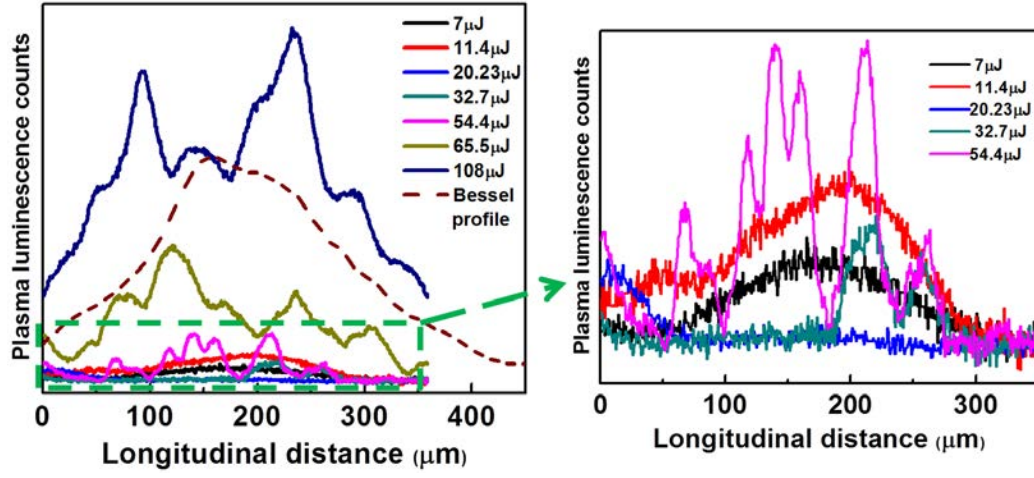


Figure 5.8: Longitudinal profiles along core of the plasma at different energies for a laser pulse duration of 60 fs. Dotted line indicates the Bessel profile inside the sample. Plot in right side is shown at lower energies to highlight the invisible features in the inset.

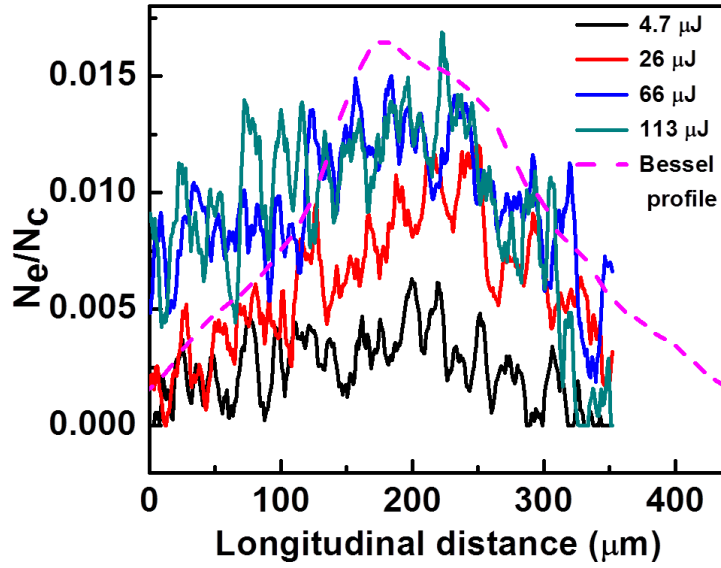


Figure 5.9: Longitudinal profiles of the instantaneous carrier density normalized to the critical density at 400 nm (N_e/N_c) along the core at selective energies for a laser pulse duration of 60 fs. Dotted line indicates the longitudinal Bessel profile inside the sample.

decay times lead to modulations in the integrated plasma luminescence whereas instantaneous carrier density profiles can be smooth.

- The modulations in plasma luminescence can be due to the complex filamentation mechanisms (consecutive focusing and defocusing cycles) in non-diffracting interaction regimes. There could be an interplay between bremsstrahlung (emission) and inverse bremsstrahlung (absorption) that could result in modulations in the plasma luminescence compared to instantaneous carrier density profiles. This process can be probable at higher energies.
- Non-saturated behavior in the plasma luminescence with laser energy which is contrast to the carrier density, could be due to the enhancement of free carrier energy gain with the laser energy even for saturated carrier generation.

5.4.2 Picosecond regime

Single pulse plasma luminescence studies in ps regime (2.8 ps) as a function of laser energy are shown in Fig. 5.10. The spatial profiles of the plasma luminescence along the structural length are shown in Fig. 5.10 (a). Also here note that only the center part of the plasma luminescence profiles have been shown in the figure. Uniformity in plasma luminescence is observed at lower energies, below $\sim 35 \mu\text{J}$ even though there exist small permanent structural modulations in the material after $\sim 12 \mu\text{J}$ (as we discussed in chapter 4). As we increase the laser pulse energy ($\geq 35 \mu\text{J}$), non-uniformity around the center of plasma luminescence is observed. At very high energies (in the order of $100 \mu\text{J}$), the plasma luminescence is found to be weak around the center of interaction volume suggesting a screening mechanism. The variation of plasma luminescence counts measured as a function of energy (considering only the center part of the interaction) is shown in Fig. 5.10 (b). Also it can be noticed from this plot that the efficiency of plasma luminescence around the center of interaction volume is decreased at higher energies.

Longitudinal profiles along the core of the plasma luminescence at selective energies are shown in the Fig. 5.11. The non-uniformity in the plasma luminescence profiles is evidenced around the center of the interaction volume for higher energies. The modulations of the plasma at different energies with respect to the Bessel beam profile (shown as dotted line) can be seen in the plot. It can be clearly noticed that with increasing of the laser energy, efficiency of the luminescence has been reduced at the center and followed at the edges of the interaction volume.

As in the case of fs regime, we correlate the plasma luminescence results with the line profiles of estimated instantaneous carrier density. Longitudinal carrier density profiles along the core at specific energies are shown in Fig.

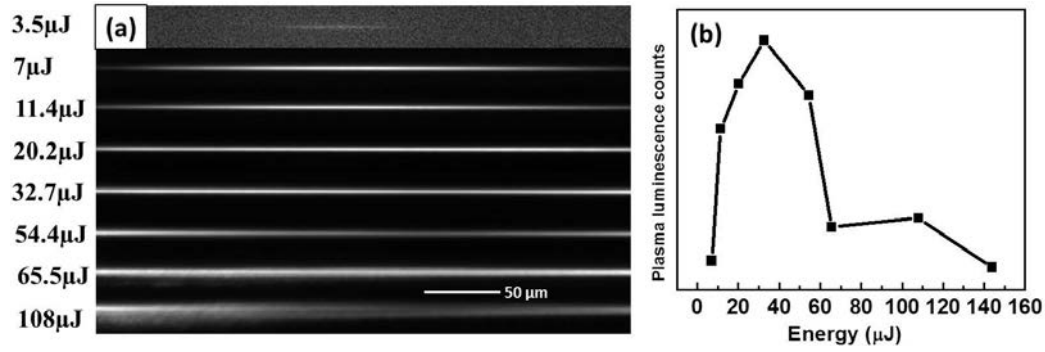


Figure 5.10: Plasma luminescence studies inside the fused silica using a single pulse with duration of 2.8 ps. (a) Plasma luminescence profiles with the function of laser energy. Relative brightness in the images indicates the contrast of plasma luminescence. (b) Variation of plasma luminescence in terms of intensity counts as a function of laser energy.

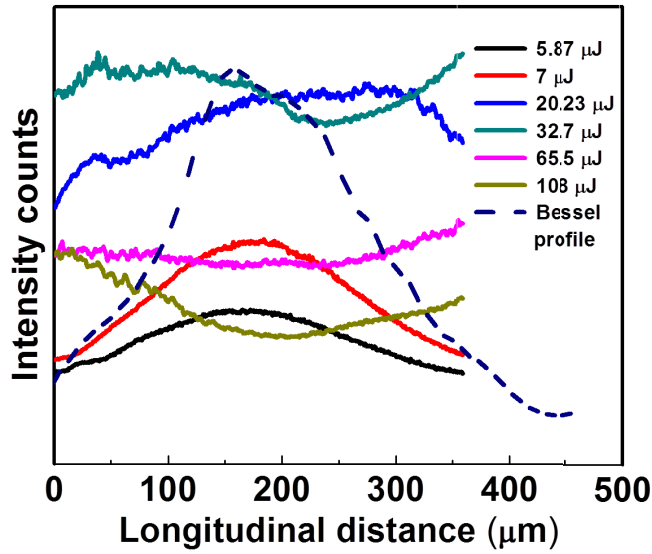


Figure 5.11: Longitudinal profiles along core of the plasma at different energies for laser pulse duration of 2.8 ps. Dotted line indicates the Bessel profile inside the sample.

5.12. As compared with longitudinal profiles of plasma luminescence, in this case also we could not observe the non-uniformity in profiles of instantaneous carrier generation along the core. Also from the figure, growth in carrier density with energy is clearly evident.

This disputation between the plasma luminescence and instantaneous

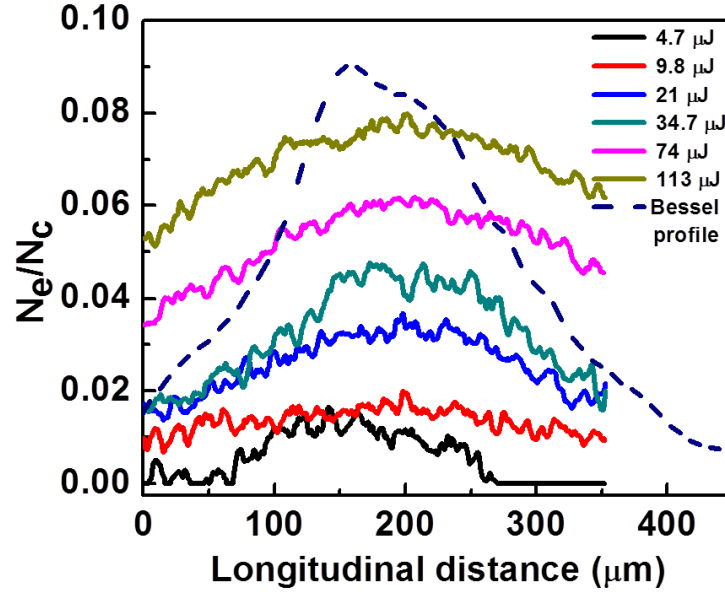


Figure 5.12: Longitudinal profiles of the instantaneous carrier density (N_e/N_c) along the core at selective energies for a laser pulse duration of 4.2 ps. Dotted line indicates the longitudinal Bessel profile inside the sample.

free carrier distribution can be understood in ps excitation conditions by the following involved possible mechanisms:

- In ps regime the non-uniformity in plasma luminescence around the center can be understood as: reabsorption by the higher carrier densities at the center by inverse bremsstrahlung as carrier densities are expected to be high at the center of the interaction volume. Resultantly, we could observe the lower integrated plasma luminescence at the center of interaction volume while the peak free carrier absorption profiles can be smoother.
- Slight non-uniform electron distribution in the excitation volume may be involved with different relaxation paths or energy gains.

In both fs and ps excitation conditions, plasma luminescence results particularly at higher laser energies indicated the distribution of non-uniform electron energy and incipient non-uniform electron densities affecting the structural modulations.

5.5 Role of probe wavelength

In order to understand the role of wavelength on transmission and absorption of the free carriers, additionally we probed with the 800 nm. In this section we compare selective results with both probing wavelengths 400 nm and 800 nm in fs and ps regimes. Probing at two wavelengths can yield additional information on plasma damping characteristics. In this section, we focus on the instantaneous carrier transmittance or absorbance with laser energy in fs and ps regimes and probed at two wavelengths.

5.5.1 Femtosecond regime

The instantaneous transmittance and absorbance due to the free carriers at peak excitation with the two probing wavelengths (blue and IR) are measured as a function of laser energy in fs regime. The variation of instantaneous transmission and relative absorbance with the laser energy for two probing wavelengths are shown in Fig. 5.13 (a) and (b) respectively. The lower transmittance (higher absorbance) for 800 nm is observed compared to the 400 nm probing until the moderate energies ($\sim 30 \mu\text{J}$). This is expectable from a Drude-like behavior as resonance carrier density values are lying higher at 400 nm. At higher energies we noticed the lower transmittance for 400

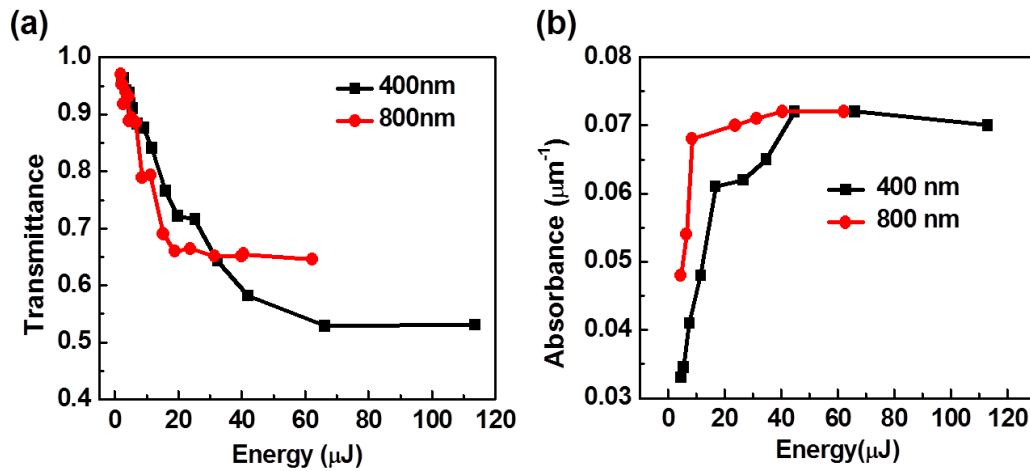


Figure 5.13: (a) Variation of instantaneous transmittance and (b) absorbance due to the free carriers as a function of laser energy at 400 nm and 800 nm probing wavelengths for a laser pulse duration of 60 fs. Note the absorbance is extracted after the projection correction using Abel inverse transform.

nm. This lower transmittance is probably due to the scattering effects of the

probe from the plasma column as scattering effects are more significant for 400 nm compared to the 800 nm. The same scattering scenario was observed using FDTD simulations (see the section 3.4). But the absorbance at higher energies is nearly same for both probe wavelengths.

5.5.2 Picosecond regime

The instantaneous transmittance and absorbance due to the free carriers with the two probing wavelengths are measured as a function of laser energy in the ps regime. The variation of instantaneous peak transmittance with the laser energy for two probing wavelengths is shown in Fig. 5.14 (a). The relative instantaneous peak absorption for the both probing wavelengths is also estimated after the Abel inverse transform. The variance of free carrier absorbance with energy is shown in Fig. 5.14(b). The lower transmittance (higher absorbance) for 800 nm is observed compared to the 400 nm probing. In ps regime also, at higher energies, scattering effects of the probe due to plasma are evident in the transmittance.

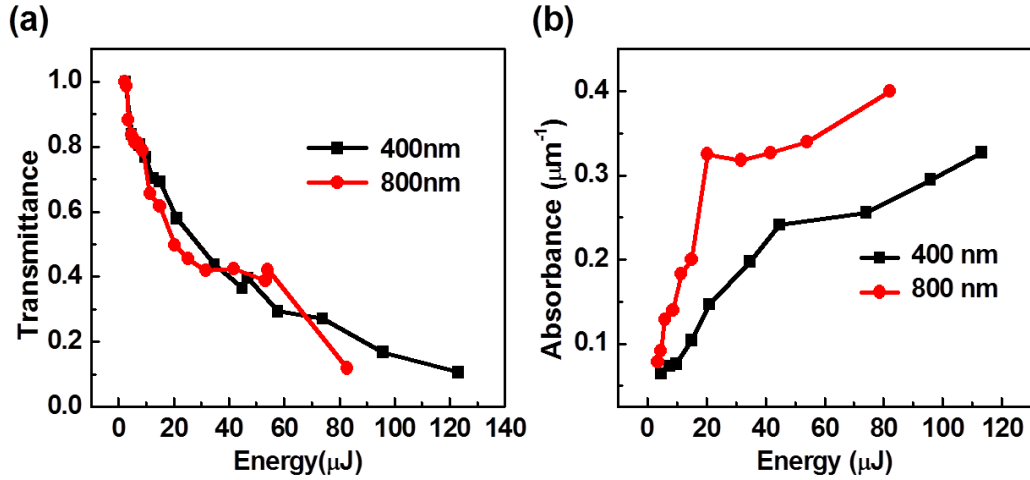


Figure 5.14: Variation of instantaneous transmittance (a) and (b) absorbance due to free carriers at peak as a function of laser energy at 400 nm and 800 nm probing wavelengths for a laser pulse duration of 4.2 ps. Note the absorbance is extracted after the projection correction using Abel inverse transform.

5.5.3 Estimation of free carrier damping time

Based on the instantaneous transmission due to free carriers at two probing wavelengths 400 nm and 800 nm, we estimated the free carrier damping

time using the formula which is derived from the Drude formalism. The free carrier scattering time can be expressed in terms of the transmittance at 800 nm (T_{800}) and 400 nm (T_{400}) as

$$\tau_c = \frac{1}{\omega_{800}} \sqrt{\frac{\ln(T_{800}) - \ln(T_{400})}{4 \ln(T_{400}) - \ln(T_{800})}} \quad (5.2)$$

We estimated the free carrier damping time for the smooth refractive structures (type-I) and uniform voids (type-II) within the stability range of structures at various energies. The variation of scattering time with the laser pulse energy in fs and ps regime is shown in Fig. 5.15 (a). Free carrier damping time is found to be varied around 0.2 fs within the considered energy range for both pulse duration regimes. For estimating the carrier density profiles experimentally from the OTM images, we considered therefore the scattering time as 0.2 fs. The small variance of transmittance in experimentally obtained OTM images for both probe wavelengths could lead to the fluctuations in carrier damping time. Therefore, we estimated the carrier damping time along the structure for a specific energy and it is shown in Fig. 5.15 (b). We found that the tolerance in carrier damping time is around 100 % of the estimated values. Note that estimated values in Fig. 5.15 (a) are obtained by considering the peak average transmittance as Bessel excitation profile is close to a bell shape. Also here it is important to mention that the error for carrier damping time estimation could be also add from the diffusion effects of the probe beam over small structures which would lead to over estimation of transmission particularly for 800 nm (see the section 3.4). Therefore if we consider the lower transmission for 800 nm, it can result in a higher carrier damping time.

5.6 Role of probe polarization

As we have seen from FDTD simulations (see the section 3.4), diffusion or scattering effects over the small structure overestimate the transmission. In order to know the role of probe scattering effects around the plasma column, we varied the probe polarization and recorded the instantaneous transmittance at 400 nm probing wavelength. The variance in transmittance with energy for probe polarization parallel and perpendicular to the plasma column in fs regime is shown in Fig. 5.16. The higher transmittance is observed for the parallel polarization where we have the lower scattering effects compared to the perpendicular polarization. Also the same trend in transmission for both polarizations with ps laser pulse duration is observed (not shown here)

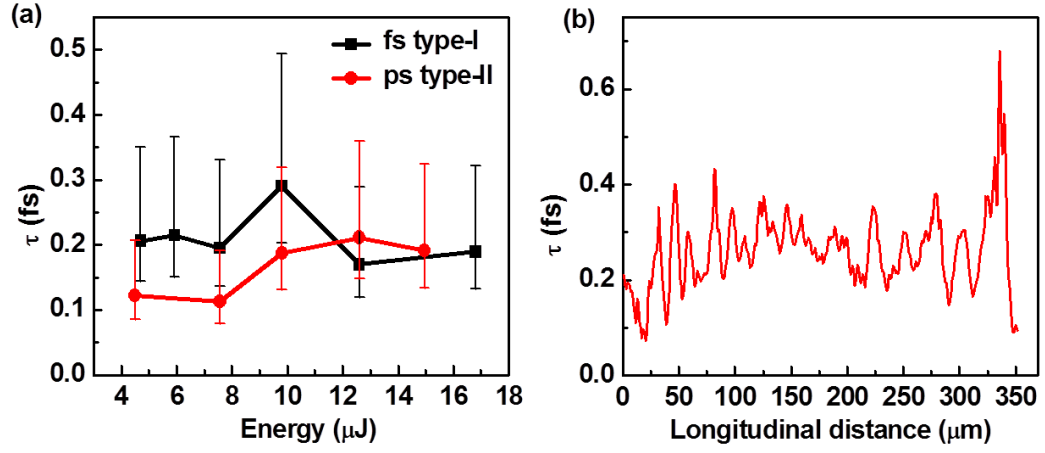


Figure 5.15: (a) Estimation of the free carrier damping time in the conditions of generalizing smooth refractive structures (type-I) in femtosecond regime and uniform voids (type-II) in picosecond regime. (b) Variation in free carrier damping time due to the fluctuations in transmission along the structure.

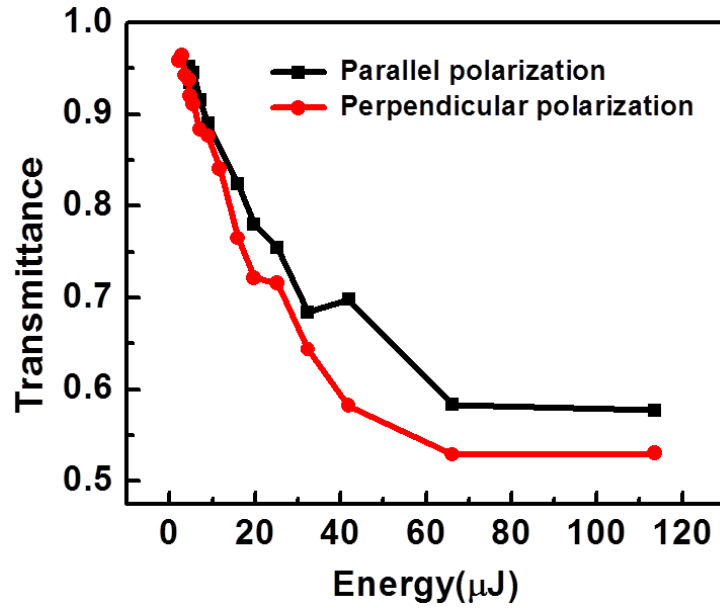


Figure 5.16: Variation of instantaneous transmission due to free carriers with the function of laser energy at different 400 nm probing wavelength polarizations for a laser pulse duration of 60 fs.

as in the case of fs regime. This measurements also confirmed the presence of probe scattering effects and the dimensional influence of the object.

5.7 Comments on estimated free carrier density

As we have seen the energy deposition efficiency in focal volume is mainly responsible for the different structural modifications. The variance in energy deposition in different pulse duration regimes can trigger the different carrier density. Defining the criteria as critical energy deposition or electron density for material damage is still ongoing debate. This uncertainty is also due to the challenge of estimating exact carrier density by experiments as ambiguities persist in defining the properties of excited carriers (for instance damping characteristics and optical mass with energy). To avoid this dilemma, we estimated one of the major parameter i.e., carrier damping time experimentally within stability range of interaction, particularly in the conditions of smooth refractive index structures and uniform voids. Experimentally estimated carrier densities for the material damage in non-diffracting regimes for both fs and ps pulse durations are found to be around two orders of magnitude lower than the critical density. Here it is important to note that for a most realistic damping time 0.5 fs i.e., considering the fluctuations and scattering effects in τ estimation, the experimentally estimated carrier densities can be 1.4 times higher than the mentioned values. As intense laser matter interaction in air is well understood and electron densities for an ultrafast laser breakdown in air are in the order of $10^{18} - 10^{19}/\text{cm}^3$, we compare the plasma luminescence of air and inside the fused silica. This comparison can give the approximate indication of carrier densities inside the bulk based on the fact that bremsstrahlung depends on the carrier density (note worthy it also depends on temperature).

Single pulse air plasma luminescence excited by ultrafast Bessel beams for fs laser pulse duration at two different pulse energies 108 μJ and 144 μJ is shown in Fig. 5.17 (a) and (b) respectively. Single pulse Bessel plasma luminescence inside the fused silica for smooth refractive index and uniform void structuring conditions is shown in Fig. 5.17 (c) and (d) respectively. The relative intensity counts of plasma luminescence according to color-map is shown for each image separately. The stronger plasma luminescence inside the bulk for ps pulse compare to the fs pulse shows that the stronger energy deposition eventually leads to a higher carrier generation for the ps laser pulse. Also it is noticed that the efficiency of plasma luminescence inside the bulk is nearly equivalent to the air plasma luminescence (here at maximum energy). These measurements indirectly signaling that our experimentally estimated values using the Drude formalism and by using the experimentally estimated carrier scattering time are realistic.

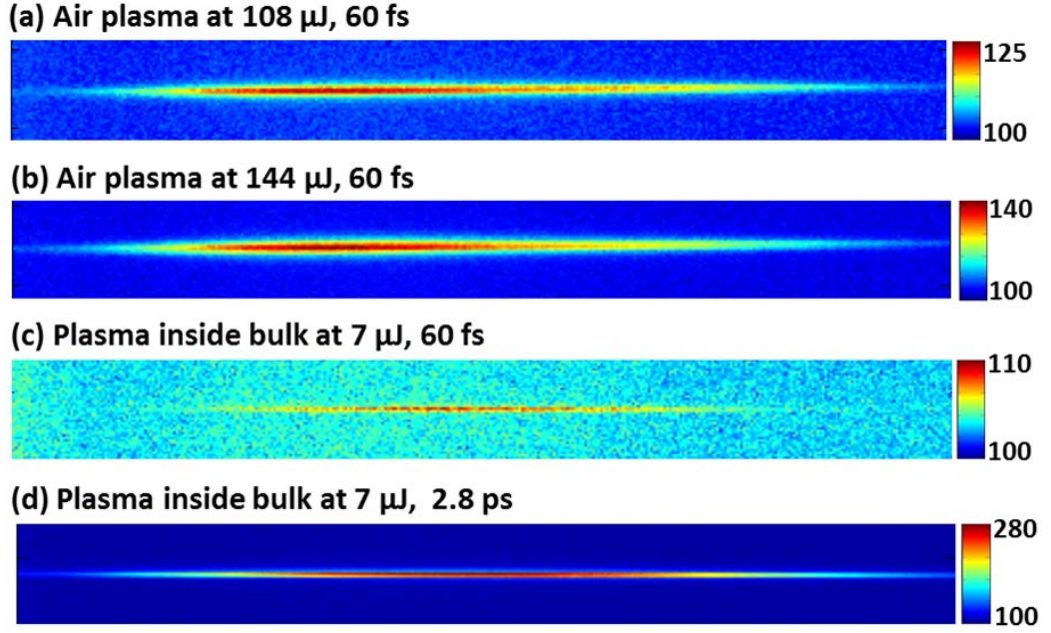


Figure 5.17: Comparison of air and inside bulk plasma luminescence (time integrated) using single Bessel ultrafast pulses. Air plasma luminescence for 60 fs laser pulse at 108 $\mu\text{J}/\text{pulse}$ and 144 $\mu\text{J}/\text{pulse}$ shown in (a) and (b) respectively. Plasma luminescence inside the fused silica is shown for 60 fs and 2.8 ps laser pulse durations at 7 $\mu\text{J}/\text{pulse}$ in (c) and (d) respectively. The relative intensity counts for each image is shown in color-map.

5.8 Conclusions

In this chapter, we presented the role of Bessel excitation using single pulse ultrafast laser Bessel beams from the instantaneous microscopy images at the peak of excitation. We estimated the instantaneous free carrier density from the optical transmission images using the simple Drude formalism. Role of instantaneous free carrier generation with laser pulse duration has been highlighted and this defines the type of structural modifications. Difference in an instantaneous free carrier density and hence in energy deposition leads to the different structural modifications. For instance higher instantaneous carrier generation in picosecond regime leads to the uniform void structure whereas lower carrier density in femtosecond regime results in smooth refractive index structure. Also we examined the role of laser excitation energy on free carrier generation in both fs and ps pulse duration regimes indicating increased self-limiting (saturation) effects in the fs case. Plasma luminescence studies have been studied to understand the electron energy distribution in the excitation

volume. At higher energies, non-uniform carrier density or energy distribution resulting in modulations in structural morphology. We also presented the role of probe wavelength and polarization on free carrier transmission. In order to have the accurate free carrier density information using Drude formalism, experimentally we estimated the most ambiguous quantity i.e., carrier damping time within the stability regimes of the interaction where we can have uniform smooth refractive index and void structures.

Chapter 6

Ultrafast dynamics of Bessel excited material modification

This chapter describes the underlying dynamics of physical mechanisms that lead to different structural modifications in fused silica using the excitation with non-diffractive Bessel beams. As we have seen in the earlier chapters, this peculiar interaction determines the high aspect ratio sub-micron structures with different structural morphology depending on the laser pulse duration i.e., smooth positive refractive index structures in femtosecond pulse duration regime and uniform voids in picosecond regime and different instantaneous carrier densities generation in these regimes. We report here the dynamics and formation mechanisms of the high aspect ratio structures in these two contrast regimes using time-resolved two color pump probe microscopy with sub-picosecond temporal resolution. Time resolved optical transmission images gives the transient optical transmission (or absorption) which enable us to estimate the relative free carrier density. Time resolved phase contrast microscopy images give the retardation of the transient phase change either by free carriers or excitons. Finally, based on these time-resolved results, with the additional supporting information from simulations and static photoluminescence studies, we formulate the formation mechanisms of smooth refractive index and uniform void structures.

6.1 Introduction

As we have seen, previous chapters were highlighting the different interaction regimes using single shot ultrafast Bessel beam which are primarily depending on the laser pulse duration and relative instantaneous free carrier generation at same laser pulse energy and focusing conditions. We recall here, in fs pulse

duration regime, lower instantaneous carrier generation leads to the smooth refractive index structures whereas ps regime generates the higher instantaneous carrier density resulting in low index structures. Now the question is how these different instantaneous carrier densities decay into different structural morphologies? What are the underlying physical processes that are involved in the formation of these structures? As already mentioned in the overview of time resolved studies, we recall here that, obviously understanding of above mentioned questions particularly in non-diffractive interaction regimes are necessary to achieve better control over the laser induced structuring. Therefore, this chapter discusses the dynamics of non-diffractive ultrafast excitation and the consequences on the morphology of material modification in bulk a-SiO₂. Particularly the carrier relaxation dynamics in both fs and ps pulse duration regimes is probed based on transient optical transmission and phase contrast images at various temporal probe delays with respect to the pump pulse. The amplitude and phase characteristics of the excited regions with sub-picosecond temporal and sub-micrometer spatial resolution address the involved relaxation paths via structural transitions around local defect generation, or macroscopic thermodynamic events.

Generation of free carrier density and the associated energy deposition define the kind of material relaxation path and therefore the ultimate material phase transformation. Including peak excitation profiles of optical transmission and free carriers, their complete dynamics exclusively in each regime is discussed in following sections i.e., the dynamics of smooth refractive index and uniform void structures. In this chapter, we mostly present the dynamics with 400 nm probe wavelength as scattering effects over the small structures are less for 400 nm compared to the 800 nm.

6.2 Dynamics of type-I positive refractive index structures

In this section, we present the spatial and time-resolved dynamics of smooth refractive index structures based on time resolved optical transmission and phase contrast images. Particularly we report the free carrier dynamics. As type-I structures are starting to be formed around the modification threshold energy, we investigated the dynamics of type-I structures around, above and below the modification threshold of the material. The objective of these studies around the threshold is to elucidate the precursor role of free carriers around the modification threshold and examine the growth of free carriers with increasing the laser energy that would be leading to the permanent

change in refractive index or material damage. For instance, single pulse static PCM structures around the damage threshold are shown in Fig. 6.1. The threshold energy was considered as the energy where the permanent static structures were starting to be visible in the phase contrast microscopy (for instance as shown image at $1.25 \mu\text{J}$) with increasing the laser energy.



Figure 6.1: Single pulse static phase contrast images of the smooth refractive index structure are shown around the modification threshold. The structures at $0.75 \mu\text{J}$, $1.25 \mu\text{J}$ and $1.72 \mu\text{J}$ are corresponding to the below, around and above the modification threshold respectively.

6.2.1 Around the damage threshold

Time resolved optical transmission microscopy (OTM) and phase contrast microscopy (PCM) images, around the damage threshold, i.e., at $1.25 \mu\text{J}/\text{pulse}$ are shown in Fig. 6.2. The zero delay was considered as the temporal overlapping of pump and probe, therefore resulting in maximum absorption. OTM images at various temporal delays are shown in Fig. 6.2 (a). The relative darkness in the OTM images corresponds to the contrast in absorption. It can be seen from the figure that an absorption signature is maximum around the zero delay and it persists until few picoseconds. This corresponds to the free carrier generation. The relative time-resolved PCM images are shown in Fig. 6.2 (b). PCM images show the transient phase change in the laser excited regime. The darker regions in the PCM image correspond to the positive phase shift with respect to the background. Remarkably the transient positive phase change has been observed until longer delays where there is no signature of the optical absorption.

The contribution of the free carriers to the transient optical absorption is estimated based on the relative transmission at each temporal delay. Transient absorbance and free carrier density profiles after the reconstruction of excitation profiles are shown in Fig. 6.3 (a) and (b) respectively. The fast decay in the absorbance and consequently the faster decay in free carrier density is observed for the Bessel excitation around the damage threshold in



Figure 6.2: Transient optical transmission and phase contrast images in conditions corresponding to formation of smooth refractive index structure are shown in (a) and (b) respectively at various probe delays around the damage threshold at laser pulse energy of $1.25 \mu\text{J}$ and pulse duration of 60 fs.

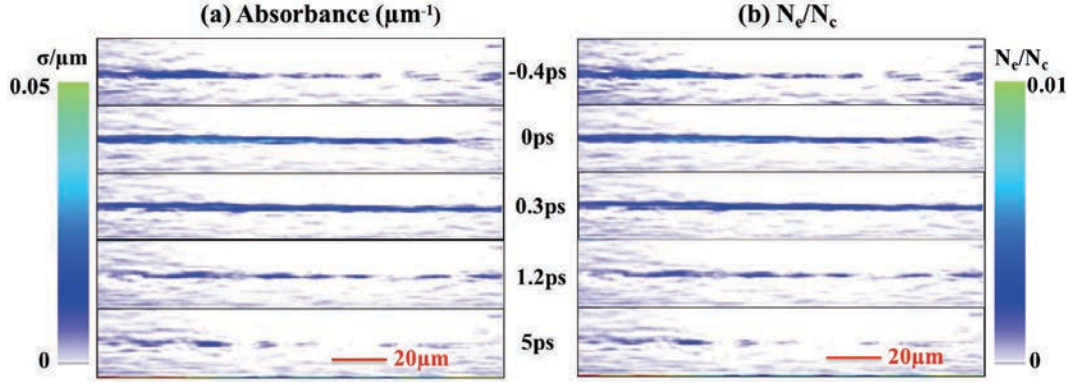


Figure 6.3: Time resolved absorbance and carrier density dynamics after extracting the excitation radial profiles from the projected OTM profiles by inverse Abel transform. Figures (a) and (b) shows the dynamics of absorbance and carrier density at various probe delays respectively around the damage threshold at $1.25 \mu\text{J}/\text{pulse}$ and 60 fs pulse duration.

the fs laser pulse duration regime. The calculated free carrier density over critical density with the probe delay is shown in Fig. 6.4. Around the damage threshold, it is observed that fast decaying of the free carriers occurs in few picoseconds of probe delay. This carrier trapping in fused silica is related to the transformation of electrons and holes pair into excitons that self-trap in self-induced matrix deformations, which are termed as self-trapped excitons (STEs). In addition, this trapping is also evidenced by positive phase change at longer delays in PCM images (see Fig.6.2) when there is no free carrier absorption. Here, we like to recall that the kind of trapping mechanism depends on the material characteristics and was observed in few materials.

For instance, in NaCl, where the free holes self-trap first and to allow the subsequent trapping of electrons by the self-trapped holes [MGD⁺97]. In the

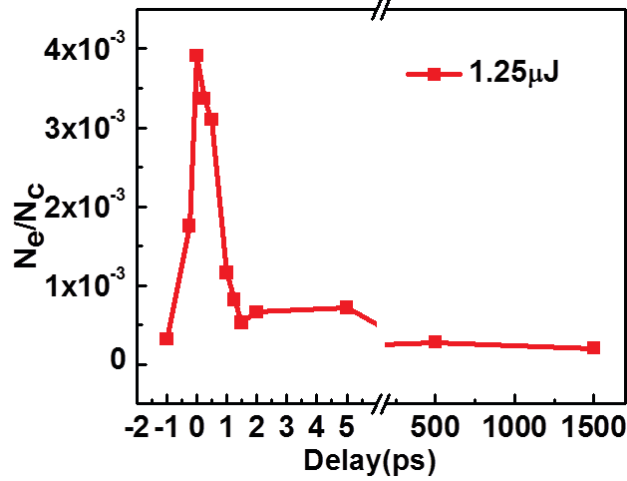


Figure 6.4: Evaluation of the relative carrier density with temporal delay around the damage threshold ($1.25 \mu\text{J}/\text{pulse}$) using the Bessel excitation at 60 fs pulse duration.

following, we present the free carrier dynamics above and below the damage threshold.

6.2.2 Above and below the damage threshold

Transient OTM and PCM images at various delays above the damage threshold i.e., at $1.75 \mu\text{J}/\text{pulse}$ are shown in the Fig. 6.5. OTM images indicate a fast decaying of carrier absorption (corresponding to free carrier trapping) similar to the dynamics around the threshold and followed by a small residual absorption at longer delays. As similar to the results around the damage threshold, transient positive phase shift is observed until longer delays and also it is noticed that there is no transient absorption in OTM images at longer delays. These results also evidence the carrier trapping as their energetic position is equivalent of a positive phase shift [MGD⁺97, QGM⁺99]. Here it is important to note that, phase shift around the zero delay in PCM images that corresponds to the free carriers (negative phase shift) is not observed. It could be due to the limitation of our phase contrast microscope which is arising from a free carrier population with a phase shift that can not be measured. This results from the limitation in the number of 400 nm probing photons passing through the circular aperture of the condenser and the mixed amplitude and phase information in the probed object. However, we

like to mention that the negative phase shift around zero delay corresponds to the free carrier generation at higher free carrier densities (at higher laser pulse energies) is observed. For instance, it is shown in Fig. 6.5 (c), where the free carrier density is estimated to be $\sim 0.01N_c$ and this can be considered as the limitation of our phase contrast microscopy. The variation

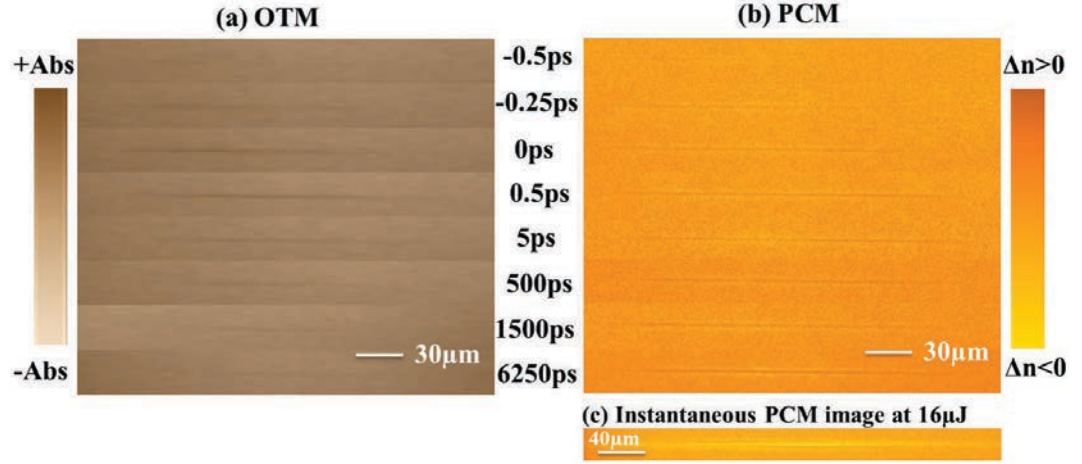


Figure 6.5: Transient optical transmission and phase contrast images of the smooth refractive index structure are shown in (a) and (b) respectively at various probe delays above the damage threshold at laser energy of $1.75 \mu\text{J}/\text{pulse}$ and 60 fs pulse duration. (c) Instantaneous PCM image at $16 \mu\text{J}/\text{pulse}$ indicating the negative phase shift associated with the free carriers.

of free carrier density at various delays is shown in Fig. 6.6. It is noticed that there is a fast decaying of free carriers associated with small amount of residual absorption at longer delays. The increase of the laser energy far from the damage threshold while remaining in type-I conditions is also resulting in fast carrier decaying in $200\text{--}400 \text{ fs}$ of temporal delay and increased free carrier density with the laser energy but with moderate efficiency due to intensity clamping.

Also we probed the dynamics below the damage threshold (chosen as an energy where the material modification can not be visible in phase contrast microscopy). Below the damage threshold, we observed the low free carrier generation compared to above and around the damage threshold. The variation of free carrier density with probe delay below the damage threshold ($0.75 \mu\text{J}/\text{pulse}$) is shown in Fig. 6.7. The trapping of the free carriers also evident from the figure in spite of that the errors are higher due to the low level of signal. The tail part of carrier densities curve shows apparently a slower dynamics. We believe that this error could be arising from the uncer-

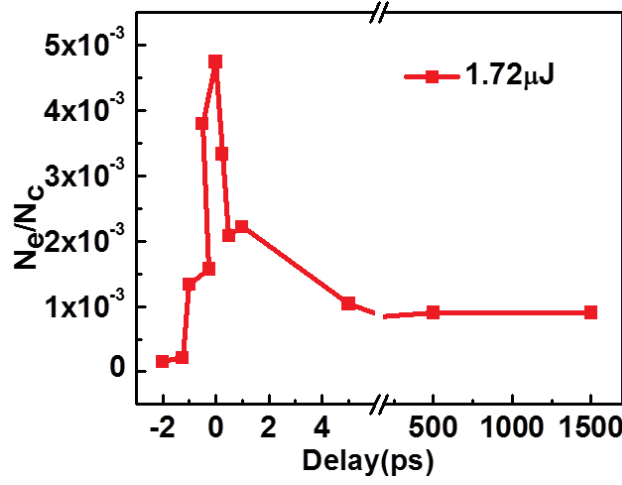


Figure 6.6: Evaluation of the relative carrier density with temporal delay around the damage threshold ($1.75 \mu J/\text{pulse}$) using the Bessel excitation at 60 fs pulse duration.

tainties in distinguishing between the signal and background in image as free carrier absorption below the modification threshold is very weak. Here we recall that the efficiency of trapping i.e., formation of self-trapped excitons is independent of the pump intensity or free carrier density [MGD⁺97].

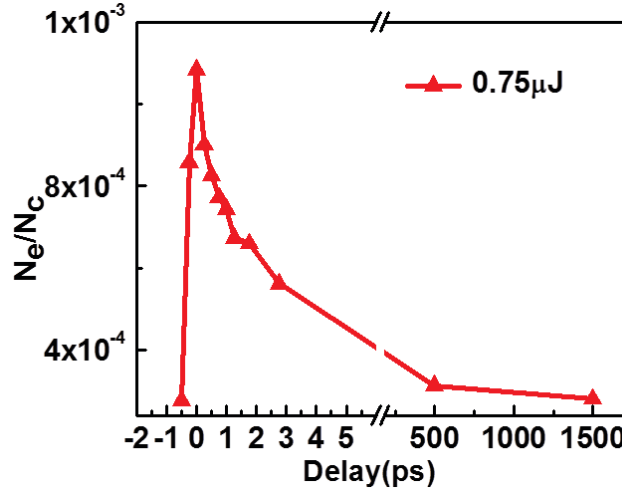


Figure 6.7: Evaluation of the relative carrier density evolution with temporal delay at energy levels below the damage threshold ($0.75 \mu J/\text{pulse}$) using the Bessel excitation at pulse duration of 60 fs.

6.2.3 At higher energy

In this section we present the dynamics of increased refractive index structures at high energy ($7 \mu\text{J}/\text{pulse}$) still in type-I conditions. For the phase contrast microscopy, already we discussed that the probe light could be a limitation as we use the phase annuls before the condenser which cut the most of the light intensity and also we are losing probe energy at 400 nm by converting to second harmonic. For instance, here we present the dynamics of type-I structures at two probing wavelengths 400 nm and 800 nm to explore our probe energy limitation particularly in phase contrast mode. Transient optical transmission and phase contrast images are shown at 400 nm probing wavelength in Fig. 6.8. As we said, to improve the probe light

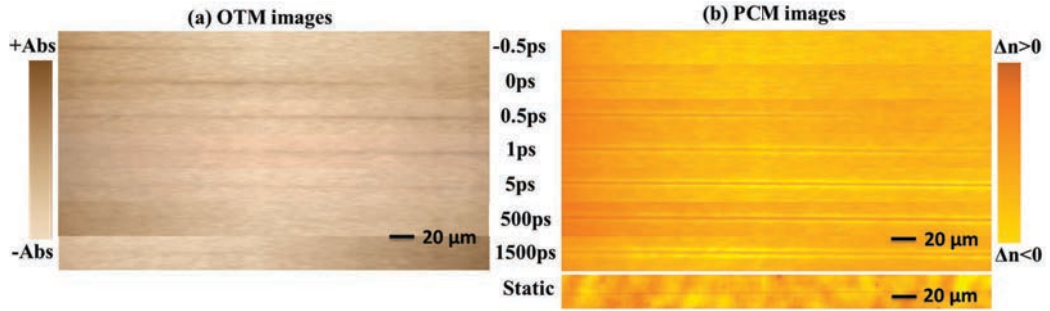


Figure 6.8: Transient optical transmission and phase contrast images of the smooth refractive index structure are shown in (a) and (b) respectively at various probe delays for laser energy of $7 \mu\text{J}/\text{pulse}$ and 60 fs pulse duration using 400 nm probing wavelength.

for the PCM, we probed the dynamics of type-I structures at higher energies with 800 nm probe light, where we found some interesting physical aspects of the interaction. Transient optical transmission and phase contrast images are shown in Fig. 6.9 (a) and (b) respectively at 800 nm probing conditions.

From the optical transmission images for both probing wavelengths, it can be noticed the fast decay in carrier absorption as we observed for all the cases in type-I conditions. But around the zero delay, we noticed the movement in peak absorption with probe delay. This movement can be also partially seen in previously mentioned type-I dynamics. In this case, at higher energies, the movement is clearly evident and corresponds to excitation driven by the conical interference front. The relative phase contrast images at 800 nm probing wavelength (see Fig. 6.9 (b)) shown a negative phase shift in front of the excitation which is also moved with the probe delay according to the front excitation. But the negative phase shift could not be observed

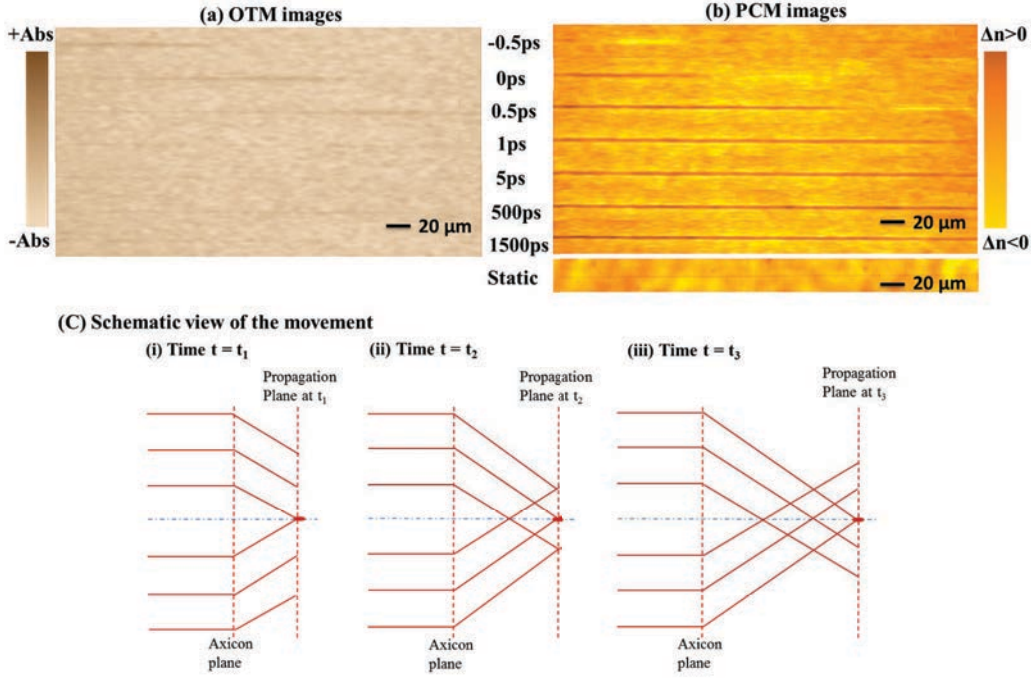


Figure 6.9: Transient optical transmission and phase contrast images of the smooth refractive index structure are shown in (a) and (b) respectively at various probe delays for laser energy of $7 \mu\text{J}/\text{pulse}$ and 60 fs pulse duration at 800 nm probing wavelength. (c) Schematic view of the Bessel beam formation (conical interference) at given three sequential time intervals $t = t_1, t_2$ and t_3 , as captured experimentally in transient OTM and PCM images.

in 400 nm probing conditions where the weak probe light could not suffer the phase retardation due to presence of lower carrier density. This negative phase shift (in 800 nm probing conditions) is due to the free carriers where the sufficient probe light can trigger the phase information. The negative phase shift around the zero delay is due to free carriers and at later time scales, the positive phase shift represents carrier trapping; the same behavior was also observed through interferometric experiments [MGD⁺97]. Here it is important to understand the movement of peak excitation as it eventually provide the significant information. This movement is due to the time lag between the Bessel beam formation by conical beam interference from the head to tail part of the beam. For a clear understanding of this movement, we shown a schematic view of the Bessel beam formation (conical interference) in Fig. 6.9 (c) at given three sequential time intervals. The proceeding of the Bessel beam formation at given time interval (at instant propagation planes t_1, t_2 and t_3) is shown clearly. From this movement, velocity of a

Bessel formation front inside the material is found to be 2.3×10^8 m/s, which is close to estimated velocity projected on the axis 2.03×10^8 m/s ($v = c/n \cos \theta$; c/n is the velocity of light in a medium of refractive index n and θ is the Bessel conical half angle). A time to space mapping is thus realized. Equally, here it is possible to estimate the life time of free carriers (from the negative phase due to peak free carrier excitation in PCM images and its spacial extent). The life time of free carriers is found to be ~ 240 fs which is close to a time required for formation of self-trapped excitons (carrier trapping). Also it is important to mention here that this movement is not resolved for ps pulse excitation dynamics (will be discussed in next section) because of the limitation of temporal resolution.

6.3 Dynamics of type-II uniform void structures

This section describes the transient dynamics of excitation in conditions leading to uniform void structures from time resolved optical transmission and phase contrast images. Time resolved OTM images of excitation corresponding to uniform voids using the laser pump energy at $7 \mu\text{J}/\text{pulse}$, 4.7 ps pulse duration for various temporal probe delays are shown in the Fig. 6.10 (a). Here it is important to mention that the probe laser pulse duration was same as the pump laser pulse duration. We recorded the transient images until the maximum probe delay, possible with our current experimental setup, of 6.25 ns. The dark regions in OTM indicate the higher absorbance regions. From the optical transmission images, gradual increase in optical absorption has been noticed around the zero delay that persisted until few nanoseconds, unlikely the dynamics observed for increased refractive index structures. The OTM structure at infinity represents the static permanent uniform void structure imaged as a scattering object. The relative free carrier density, responsible for the optical absorption is estimated. The estimated free carrier density profiles (assuming that the absorption is generated by free carriers) are shown in Fig. 6.10 (b). It is noticed that higher carrier densities are observed for type-II structures compared to type-I.

Transient phase change induced by the free carriers has been observed using time resolved phase contrast imaging at 800 nm probing. This information is however mixed with the response at the level of the matrix. Transient positive PCM images during the formation of the uniform void structure are shown in the Fig. 6.11 (a) at different temporal delays. The bright regions in the positive phase contrast images indicate the negative phase shift while

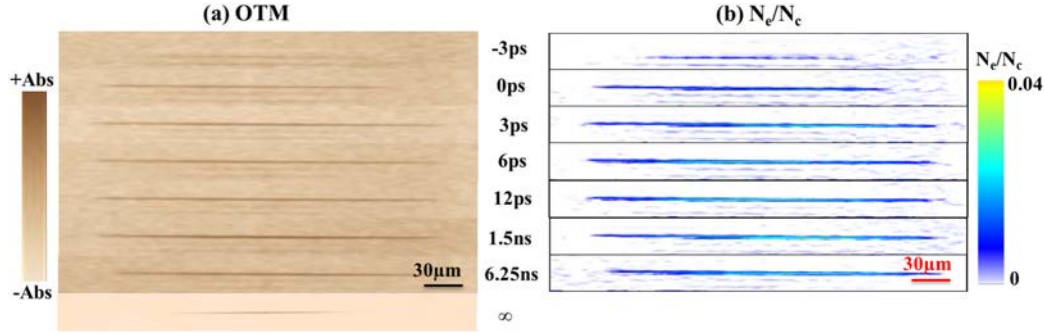


Figure 6.10: Time resolved optical transmission images are shown at various temporal delays of the probe in (a) and corresponding carrier density estimation after the projection correction using Abel inverse transform are shown in (b) for excitation leading to uniform void structures ($7 \mu\text{J}/\text{pulse}$, 4.7 ps). OTM image at infinity corresponds to the static OTM structure of the uniform void.

the dark regions represent the positive phase shift in the interaction volume. It can be noticed from the figure that the negative phase shift in PCM images corresponds to the presence of free carriers. Long living free carriers are evident from the images. At longer delays, positive phase shift is observed probably due to the compression zone around the cavitation. So it may be related to the onset of a different material phase with high carrier density and temperature. This positive phase change is also confirmed from the negative phase contrast images, for instance, image is shown at 1.5 ns probe delay in Fig. 6.11 (b). Note here that the bright zones indicate the positive phase shift. The positive and negative PCM measurements at longer probe delays indicate the positive phase shift and no significant amplitude information is presented in phase contrast images. For the probe delays 1.5 ns and 6.25 ns , symmetrical positive phase shift has been observed below and above the structural phase change and the movement of this transient phase with the probe delay has been observed. This symmetrical transient phase is associated to the propagation of pressure or elastic wave at the speed of sound. The structure after infinitely longer time i.e., static structure in same probing conditions is shown at infinity. Evolution of the free carrier density which is responsible for transient optical absorption (assuming that the absorption is arising from the free carriers) with a function of temporal delay is shown in Fig. 6.12. It can be noticed from the plot that there is a growth in free carrier density around the zero delay and nearly saturated at higher delays. We believe that this absorption is due to the free carriers that are associated with glass matrix which is in liquid phase. Particularly

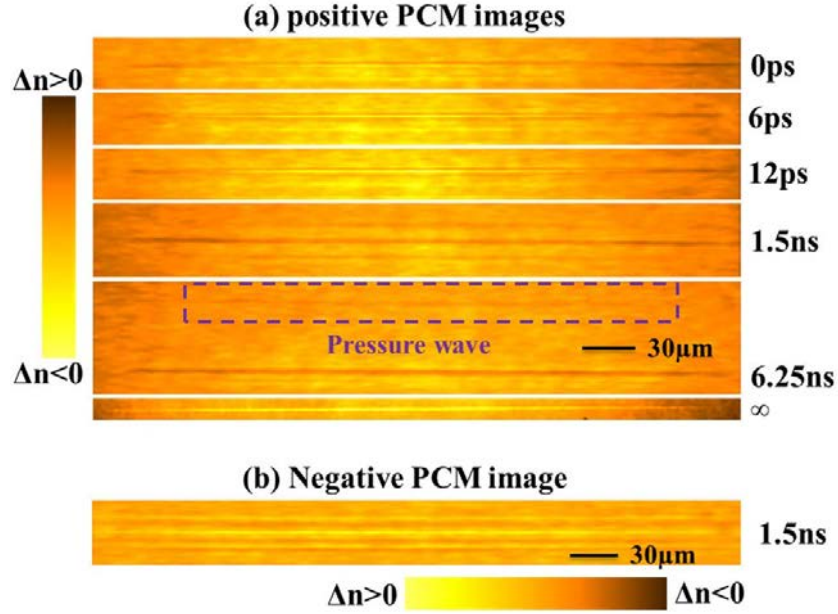


Figure 6.11: (a) Time resolved positive phase contrast microscopy images of the uniform void structure are shown at various probe delays. For the delay of 6.25 ns, the highlighted region shows a phase change that corresponds to the pressure wave propagation. The structure at infinity corresponds to the static PCM structure of the uniform void. (b) Transient negative phase contrast image at the probe delay 1.5 ns indicating the positive phase change. Note the opposite contrast in positive and negative PCM images. Probing was done at 800 nm.

in the conditions of a hot matrix, the efficiency of trapping is reduced due to the decrease in strength of the trapping deformation potential. Also in order to validate the dynamics of free carriers in liquid matrix, we probed the free carrier dynamics in water with Bessel excitation and it is shown in Fig. 6.13. This results indicate a slow dynamics of free carriers in water which is similar to the dynamics of free carriers inside the bulk in void fabrication conditions. Also the release of pressure wave at longer probe delays suggest that the excitation conditions trigger the higher temperature and pressure, obviously consequence of the stronger energy deposition in ps regime. Slower free carrier dynamics associated with attaining the liquid phase and release of pressure wave indicate the hydrodynamic mechanisms that are responsible for the formation of voids.

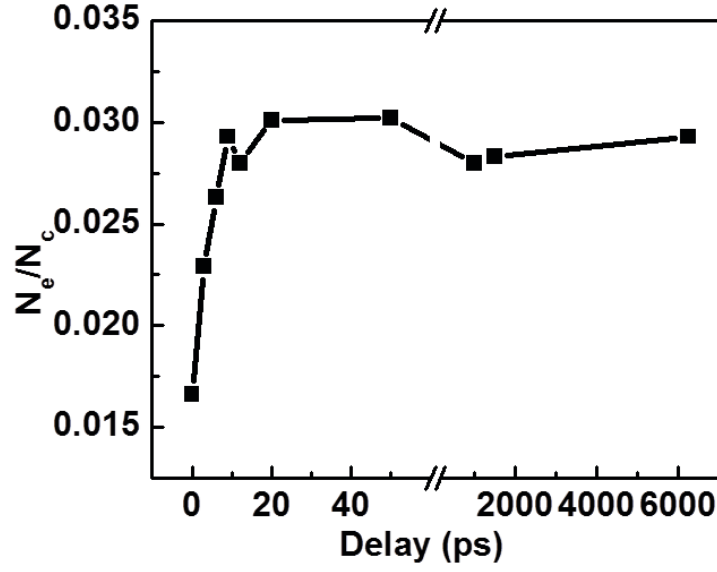


Figure 6.12: Variation in free carrier density over critical density with the probe delay for uniform void structures.

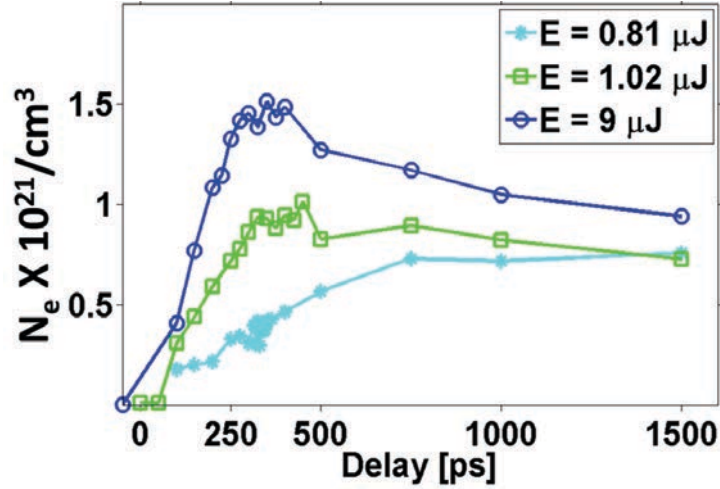


Figure 6.13: Dynamics of free carriers in water upon Bessel excitation at three different energies.

6.4 Potential formation mechanisms

In this section we summarize the results obtained from the experiments and simulations which provide conclusions about the formation mechanisms for smooth positive refractive index and uniform void structures. Here we recall

the dynamics of type-I and type-II structures at the same laser pulse energy. Variation in free carrier density normalized to critical density with the probe delay for conditions corresponding to the formation of smooth refractive index (type-I) and uniform void (type-II) structures at $7 \mu\text{J}/\text{pulse}$ is shown in Fig. 6.14. The fast decaying of free carriers in fs regime is evident compare to the dynamics in ps regime. Also carrier densities are observed to be higher in the ps case resulting from the stronger energy deposition as we have seen equally from simulation results. Also in the following table 6.1, we outlined

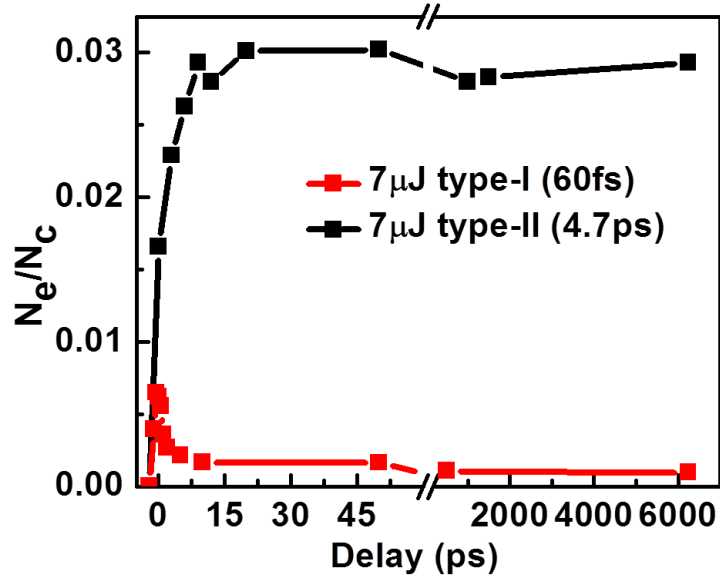


Figure 6.14: Variation in free carrier density over critical density with the probe delay for the type-I and type-II structures at $7 \mu\text{J}/\text{pulse}$.

the important parameters which were estimated experimentally and theoretically such as free-carrier density (N_e) and deposited energy density (E_{dep}). We recall here the mentioned values give only the indicative estimations because of the tolerance in estimating carrier damping time associated with transmittance fluctuations and probe diffusion effects over small structures. Hence for a most realistic carrier damping time (0.5 fs), the experimentally estimated carrier density can be 1.4 times more than the mentioned values (i.e., $\left(\frac{N_e}{N_c}\right)_{0.5fs} = 1.4 \left(\frac{N_e}{N_c}\right)_{0.2fs}$). Also we recall here from the experimental section, carrier density can be increased to 3-4 times of the mentioned values by improving the blurring of averaged images i.e., manually defining the center of each plasma absorption image followed by averaging. Higher free carrier density and stronger energy deposition are observed for a ps laser pulse compare to fs pulse by both experimentally and theoretically. Based on

these results (results that were discussed in this chapter and chapter 4), we formulate the formation mechanisms of the smooth refractive index structures and uniform voids in fs and ps regimes respectively in the following sub-sections.

Parameters	femtosecond regime (60 fs)	picosecond regime (4.7 ps)
Experimentally estimated N_e (7 μ J, $\tau_c = 0.2$ fs)	$4.53 \times 10^{19}/cm^3$ ($0.0065N_c$)	$2.09 \times 10^{20}/cm^3$ ($0.03N_c$)
N_e from simulations (7 μ J, $\tau_c = 0.2$ fs)	$1 \times 10^{21}/cm^3$	$6.25 \times 10^{21}/cm^3$
E_{dep} from simulations (7 μ J, $\tau_c = 0.2$ fs)	$3970 J/cm^3$	$23000 J/cm^3$
E_{dep} from simulations (7 μ J, for a more realistic $\tau_c = 0.5$ fs)	$1400 J/cm^3$	$5490 J/cm^3$ (3.1 ps)

Table 6.1: Comparison of the experimentally estimated free carrier density, simulated free carrier density and deposited energy density (E_{dep}) in femtosecond and picosecond regimes at similar conditions. N_c is the critical density at 400 nm ($6.97 \times 10^{21}/cm^3$). Note that N_e is estimated by assuming a constant optical mass (m_e).

6.4.1 Formation mechanisms of increased (smooth) refractive index structures

From the time resolved dynamics of smooth refractive index structures, we noticed the fast decaying of free carriers with in few hundreds of fs temporal delay corresponds to trapping of the free carriers [MGD⁺97] in excitonic states. In case of fused silica, these are known as self trapped excitons (STEs). Also, formation of STEs is evident from the transient PCM images. Particularly, at longer probe delays (after 5ps), we did not observe transient absorption in OTM images but observed the transient phase change in PCM images and this positive phase change is attributed to the formation of STEs with energy positions in the band gap. Ex-situ photoluminescence results manifest indirectly the formation of STEs via the formation of products derived from STEs. We used a photoluminescence setup based on a confocal desorption. Fig. 6.15 shows the photoluminescence from the increased refractive index structure excited by He-Ne laser (633 nm). The photoluminescence peak at

650 nm corresponds to the NBOHC defects which are the typical product of the STEs in fused silica. This is the major defect contribution in type-I conditions. The self-limited efficiency of electron generation has also further

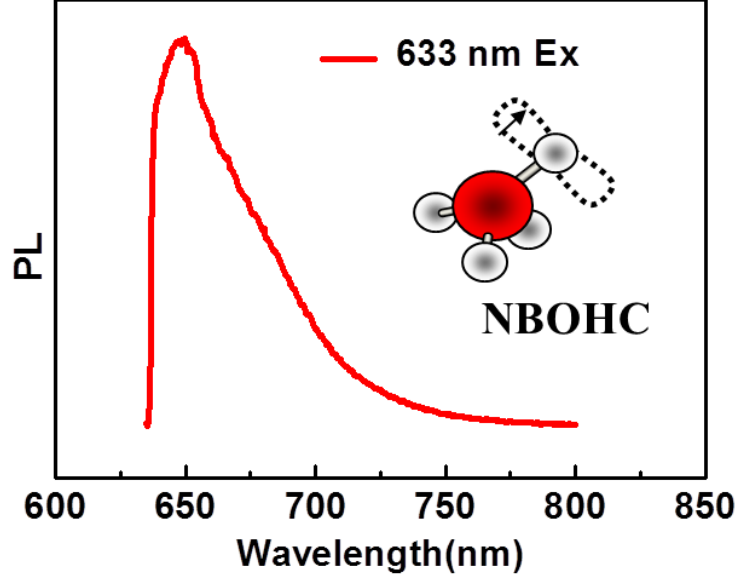


Figure 6.15: Photoluminescence (PL) from the smooth positive refractive index structures excited by 633 nm. Presence of NBOHC defect centers (peak at 650nm) is evident from the PL peak.

notably limited the thermal consequences. Also the rise in temperature in the focal volume is estimated to be well below the softening temperature of the fused silica (discussed in chapter 4). Increasing of the laser pulse energy far above the damage threshold, a still fast decaying in carrier density has been observed. The defocusing nature of free carriers leads to saturation in energy deposition at higher energies (section 5.3). This fast decaying of the free carriers and their trapping can lead to the strain in bonds resulting in formation of defect centers. Formation of NBOHCs after the carrier trapping can determine the densification of the material resulting to an increased refractive index. This scenario was confirmed by Raman analysis in Gaussian laser beam induced type-I structures via the formation of more compacted three member $Si - O$ rings [Mis12]. So defect driven (non-thermal) color centers mediated by formation of trapped carriers lead to the formation of type-I structures with the Bessel excitation in fs laser pulse duration regime.

6.4.2 Formation mechanisms of uniform voids

In the ps case, we observed the persistence of free carriers until much longer time (ns) compare to the fs case and carrier density is found to be higher following the confined energy deposition along the propagation axis. Along with the free carrier dynamics, spectroscopic (photoluminescence) investigation of permanent structures was also performed to identify the permanent defect centers in the conditions corresponds to the uniform voids. The photoluminescence of the permanent uniform void structures is shown in Fig. 6.16 upon 325 nm laser excitation. An emission band centered at 550 nm is observed and it is attributed to a E'_δ defect centers [NWI⁺96]. The signal comes presumably from the interfaces opened during the void formation. The 550 nm peak is accompanied by a weak contribution centered at 650 nm that could arise from the shock affected compression regions surrounding the uniform void structures. The strong luminescence peak at 550 nm along the uniform void structures indicate the presence of oxygen deficiency centers (ODC) i.e., E'_δ centers formation resulting from a strong process of band breaking.

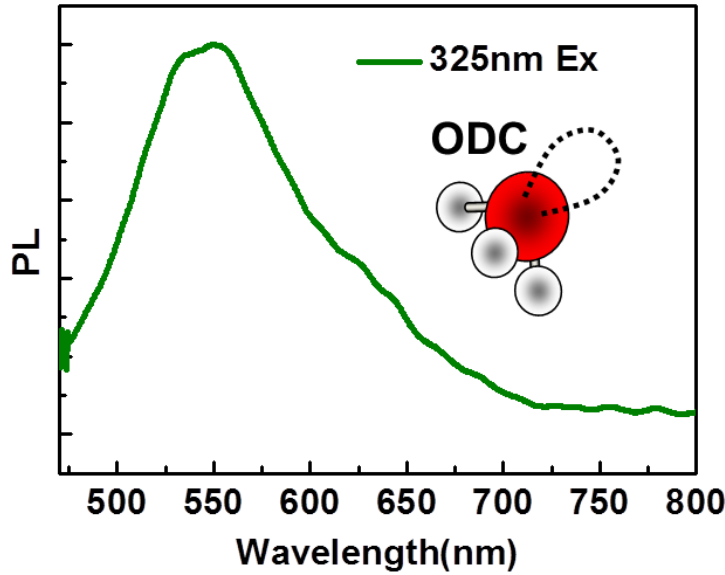


Figure 6.16: Photoluminescence(PL) spectrum originally from the region accompanying void structures excited by 325 nm wavelength.

Correlating the time resolved dynamics, simulation results and photoluminescence studies, important conclusions can be drawn about the formation mechanisms of uniform voids. Transient OTM and PCM results put

forward the generation of higher free carrier densities and their persistence until longer temporal delays. This longer life time of free carriers could be indicating the transformation of the matrix into the liquid phase from the fact that the carrier dynamics is slower in low viscosity, vibrationally hot matrix as the trapping is based on deformation potentials. This signals that the carrier trapping probability is lower in these conditions. For uniform voids, higher carrier density is observed compared to the smooth refractive index structures. This higher carrier density in the focal volume ensures a significant energy transfer to the focal volume which leads to the higher temperature and pressure conditions. A pressure wave is generated in the focal volume and propagates into a surrounding cold material. Here, it is important to note that the propagating shock wave into a cold material loses its energy due to dissipation, for example due to the work performed against the internal pressure (Young modulus) of the cold material which resists the material compression. The shock wave converts into a elastic (sound wave) or pressure wave at the stopping point. The elastic wave propagates further into the material without inducing any permanent changes in the solid. This propagation of elastic wave was observed at longer delays in time resolved PCM images and it is clearly evident at higher probe delays (Fig. 6.11, at 1.5 ns and 6.25 ns). Experimentally, shock effected region (200 – 500 nm in focal volume [JNT⁺06, JMH⁺06]) can not be resolved because of the limitation (spatial resolution) of our setup. The speed of the pressure wave has been observed to be in the order of 6×10^3 m/sec similar to the speed of sound. The shock wave propagation and subsequent rarefaction mechanisms lead to the formation of void inside the material as cavitation in the liquid phase or even a transition to gas phase. The presence of the oxygen deficiency centers was observed in the uniform void regions indicating the nucleation and release of oxygen and the opening of interfaces. So, thermodynamically driven hydrodynamic expansion leads to the formation of uniform voids with the Bessel excitation in ps laser pulse duration regime.

6.5 Dynamics in tight focusing conditions

Some of the self-limiting effects in the fs laser interaction can be overcome by tighter focusing, compensating thus diffraction and light defocusing effects. Pertaining investigations in the tight focusing conditions, we found that the interaction regime may results in void-like regions in between smooth refractive index structures. We noticed that the smooth refractive index structures have a stronger phase contrast (appearing darker) in PCM images, indicating a highly increased refractive index structures. This kind of structures exists

in tight focusing conditions for both fs and ps pulse duration regimes. For instance, the static PCM structure is shown in Fig. 6.17 for the fs case. We present in the following the dynamics corresponding to this structures mixed in these interesting regimes.

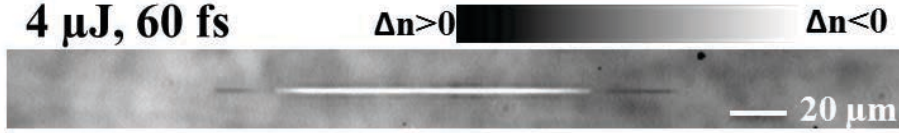


Figure 6.17: Static PCM structure in tight focusing conditions for the cone angle inside the sample is 15.1° at laser pulse energy of $4 \mu\text{J}$ and duration of 60 fs.

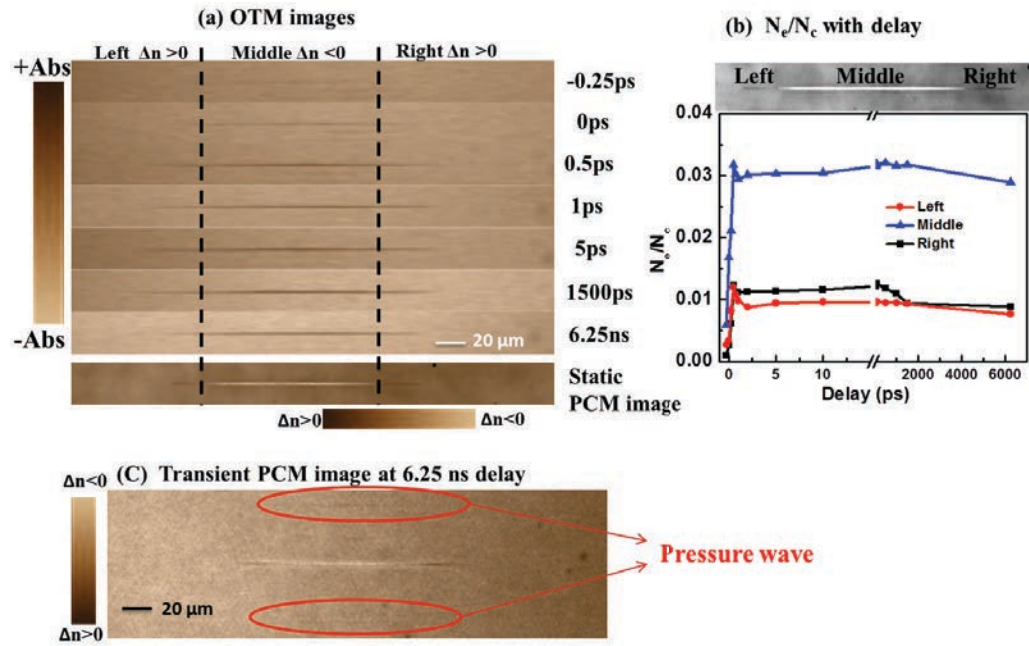


Figure 6.18: (a) Transient OTM images at different probe delays, (b) Estimated free carrier density with the probe delay averaged over three different regions of the structure: left (permanent $\Delta n > 0$), middle (permanent $\Delta n < 0$) and right (permanent $\Delta n > 0$) as highlighted in the figure in tight focusing conditions for the laser pulse energy of $4 \mu\text{J}$ and duration of 60 fs. (c) Transient PCM images at 6.25 ns probe delay and highlighted the phase shift associated to the generation of pressure wave with a weak magnitude.

Transient optical transmission images are shown in Fig. 6.18 (a). Left

and right edge regions in the images indicates the dynamics of positive refractive index structures and center region indicates the dynamics in conditions leading to void-like structure. We estimated relative carrier density at different probe delays corresponding to these three regions. These three different regions were carefully defined by comparing their static structural modification with the pattern of each probe delay. The average carrier density variation with probe delay is shown in Fig. 6.18 (b) in the three regions according to regions highlighted in the figure. Dynamics for void-like conditions is quite close to the void dynamics in moderate focusing conditions. The similar dynamics of void and pressure wave generation (shown in the Fig. 6.18 (c)) indicates similar formation mechanisms that are discussed for void formation i.e., thermally and/or hydrodynamically driven expansion and rarefaction. Remarkably here increased refractive index structures shown a slower dynamics, with a high carrier density, compared to the increased refractive index structures in moderate focusing conditions. Stronger positive phase contrast in static PCM image and slower carrier dynamics indicates the new kind of material modification. We speculate that in this case heating effects add to the reorganization of the matrix via defects.

6.6 Conclusions

In this chapter, we presented the relaxation dynamics following by a Bessel excitation of carriers and formulated the formation mechanisms of single pulse Bessel excited material modifications using time resolved microscopy. Particularly, we studied the free carrier dynamics but the matrix response was equally observed. Difference in an instantaneous free carrier density determine the different relaxation dynamics. For instance, low carrier densities in the case femtosecond pulse duration regime followed the faster decaying and contributing to type-I generation. Low free carrier densities and fast carrier trapping would lead to the strain in bonds by forming the STEs. The formation of STEs were confirmed indirectly by the observation of NBOHC photoluminescence as NBOHC is a typical product of STEs. Carrier trapping is eventually leading to bond breaking (non-thermal structural modification) which can trigger structural reorganization and the densification of the material locally, hence resulting in positive refractive index structures. Whereas higher carrier densities in picosecond pulse duration regime followed a longer relaxation path. Higher carrier densities and effective energy deposition in the picosecond regime lead to release of pressure wave and the subsequent rarefaction leaves behind the low density void structure. So, thermodynamically driven mechanisms were responsible for formation of uniform voids.

Chapter 7

Conclusions and perspectives

7.1 Conclusions

This thesis describes a novel approach to control the laser induced refractive index at sub-micron scale with high aspect ratios inside bulk dielectrics. The process is potentially required for future 3-D integrated photonic device applications. Understanding of the laser induced processes, for instance, processes associated with the electron mediated energy transfer to the lattice following excitation, are important for a better control over the interaction or laser induced refractive index change. For this purpose, we studied underlying physical mechanisms that are associated with the interaction of non-diffracting Bessel beams with fused silica which leading to the high aspect ratio sub-micron structures.

We reported thus material processing using ultrafast non-diffractive zeroth-order Bessel beams. Mainly, we studied the role of focusing conditions and laser parameters such as laser energy and pulse duration on material damage. Moderate focusing conditions permit the achievement of a stable (no modulations) but flexible interaction regimes for formation of either uniform increased refractive index (type-I) structures or low index uniform void (type-II) structures. The question of controllability and optimality of the interaction lies at the core of this study. Laser pulse duration and dispersion engineering were found to be key in obtaining the type-I and type-II structures. For instance, material interaction with femtosecond laser pulse resulted in type-I index increase based on defect assisted compaction structures whereas interaction with picosecond laser pulse resulted in uniform void structures following rarefaction in low viscosity phase. In order to understand the formation of these structures and transitional behavior in structural morphology, free carrier excitation and relaxation dynamics were

presented using the time resolved pump-probe microscopy. The dynamic perspective defines characteristic relaxation times and offers insight into the control factor. Also a numerical model was developed with a focus on the nonlinearity of laser energy deposition.

Pointing out to carrier multiplication and light scattering properties, simulation results shown that the interaction with a femtosecond laser pulse, defocusing of the trailing edge of laser pulse due to the free carriers already generated by the leading edge of the laser pulse lead to the inefficient energy deposition on the axis. Resultantly, it leads to the lower free carrier generation which was confirmed experimentally by the instantaneous carrier excitation studies. We have thus put in place techniques for time-resolved observations of electronic and material response. we found that free carriers in femtosecond laser pulse duration regime decayed in few hundreds of femtosecond temporal delay after the excitation. This fast carrier decay corresponds to the trapping of free carriers, in fused silica, termed as self-trapped excitons (STEs). The formation of STEs was also confirmed by the remnant phase change in phase contrast microscopy images. Post-irradiative photoluminescence studies indicated the presence of NBOHC defect centers, also confirming the formation of STE as NBOHC is a primary typical product of the STEs. The rise in temperature around the focal volume was found to be well below the softening temperature of fused silica. The above mentioned studies strongly conclude that the defect driven structural rearrangements lead to the formation of smooth refractive index structures.

For the picosecond Bessel excitation, simulation results revealed that the lower efficiency of the defocusing effects is a key factor in increasing energy deposition on the axis. This stronger energy deposition on the axis lead to the generation of a higher carrier density confirmed from the experimental instantaneous carrier density measurements. In the picosecond Bessel excitation regime, we noticed that the persistence of free carries until longer temporal delays (ns) and similar carrier dynamics as in water indicating the free carriers that were associated with the material in liquid phase. These results also strongly supported by estimated temperature in the focal volume was found to be above to the softening temperature. The generation of pressure wave accompanying rarefaction was captured experimentally. Consequently the formation of uniform voids for picosecond Bessel excitation can be understood as follows: the higher carrier density in the focal volume ensures the faster energy transportation to the lattice and also lead to the higher temperatures and pressures in the focal volume resulting in material expansion. The propagation of shock wave from the focal volume accompanied by the rarefaction of the material results in formation of voids. Also we confirmed by photoluminescence results that the presence of interface oxygen

deficiency centers in the uniform void regions.

In order to have an accurate evaluation of free carrier density using Drude formalism, we estimated the one of most ambiguous quantity experimentally i.e., free carrier damping time using two color pump-probe absorption technique. We found that the estimated free carrier densities were below the critical carrier densities in both femtosecond and picosecond excitation conditions.

7.2 Future perspectives

In this section we present works that are potentially interesting to be performed in near future as direct perspectives of this work. They lay on two levels: fundamental knowledge and technology potential.

- **Fundamental aspects:** A major question is related to resolving temperature evolution in both electronic and matrix systems. What would be the temperature evolution in increased refractive index and void formation conditions? In order to estimate the temperature, spectrally time-resolved plasma luminescence studies can be suggested as plasma luminescence spectra mainly depends on the evolution of carrier density and the temperature. Dynamic change of plasma luminescence spectra provides a view on comparative manner between two regimes.

As we have seen, the dynamics of increased refractive index structures shown the fast carrier trapping (self-trapped excitons). The positive phase change in phase contrast microscopy images was observed when there was no carrier absorption at longer delays and this phase change is attributed to the excitons. Additionally, primary relaxation steps of the excitons need to be resolved energetically using the time-resolved photoluminescence studies. Also in void formation conditions, strong residual absorption at longer probe delays was noticed. Time-resolved spectral imaging studies can provide the detailed aspects of this absorption and on the presence of excited dense matter. In the same strategy the kinetic properties of ejecta during void formation should be explored to gather information on thermodynamical conditions.

- **Technological aspects:** As we have seen, material processing using zeroth order Bessel beams provide the uniform high aspect ratio structures. This uniform material modification in stable interaction regimes can be employed for fabrication of efficient nano Bragg gratings.

Exotic beam shapes like non-diffractive vortex beams, high order Bessel beams and Airy beams should be further explored for laser material

processing as novel features of interaction are emerging in forms and aspects of processing zones.

Large area structuring is a subject with strong technological potential with connection to the etching of the high aspect ratio structures. This can lead to the fabrication of larger scale microstructures.

Also the non-diffracting needle beams (for example, generation techniques were proposed in [BDG09, BDG12]) with longitudinal field components can be employed for new types of laser matter interaction. Non-diffractive interaction can be performed on parallel ways towards new concepts of efficient fabrication.

Appendix A

Image treatment: Abel inverse transformation

Time resolved optical transmission images are the source for estimating the absorbance and free carrier density. In real practice (imaging with microscope), these images are projecting on to the observing plane (CCD). To have accurate details in optical transmission and carrier density, it is necessary to reconstruct the two dimensional distribution from the measured projections. A special case of this reconstruction is the Abel transformation which is used to study of radially symmetric objects, when an unknown function $f(r)$ can not be measured directly but only by integrating it along straight line paths, thus providing the projection $p(y)$ schematically represented in the Fig. A.1. The relation between these two functions is given by the Abel transform:

$$p(y) = 2 \int_y^R f(r) \frac{r}{\sqrt{r^2 - y^2}} dr \quad (\text{A.1})$$

The reconstruction of the unknown function $f(r)$ from the projection $p(y)$ can be done by means of inverse Abel transform as follows

$$f(r) = \frac{-1}{\pi} \int_y^R \frac{dp(y)}{dy} \frac{dy}{\sqrt{y^2 - r^2}} \quad (\text{A.2})$$

In practice, the projection $p(y)$ is not given analytically i.e., the problems are caused by measurement errors and especially by the differentiation of the noisy data $p(y)$ in Eqn. A.2. We used the Fourier based algorithm which extracts the radial distribution from the projection. This algorithm has been proposed by G. Pretzler [Pre91]. The used algorithm Matlab code can be found on Mathworks ¹. According to this algorithm, $f(r)$ is expanded

¹www.mathworks.fr/matlabcentral/fileexchange/43639-abel-inversion-algorithm

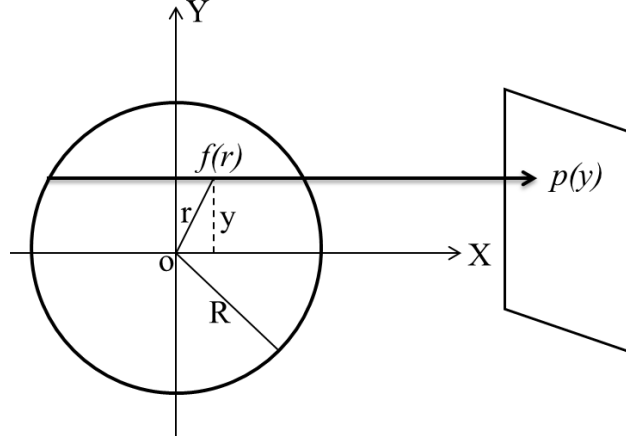


Figure A.1: Schematic representation of radially symmetric distribution $f(r)$ measured by integrating it along X-direction thus producing the projection $p(y)$.

in a series similar to Fourier series.

$$f(r) = \sum_{n=N_i}^{N_n} A_n f_n(r) \quad (\text{A.3})$$

where A_n are amplitudes and $f_n(r)$ is a set of cosine functions e.g.

$$f_n(r) = 1 - (-1)^n \cos(n\pi \frac{r}{R}) \quad (\text{A.4})$$

Following the equation A.1, The Abel transform of the A.3 i.e., $P(y)$ has the form

$$P(y) = 2 \sum_{n=N_i}^{N_n} A_n \int_y^R f_n(r) \frac{r}{\sqrt{r^2 - y^2}} dr \quad (\text{A.5})$$

The integrals

$$p_n(y) = \int_y^R f_n(r) \frac{r}{\sqrt{r^2 - y^2}} dr \quad (\text{A.6})$$

cannot be solved analytically and are calculated numerically by least square method as

$$\sum_{k=1}^N [P(y_k) - p(y_k)]^2 \rightarrow \text{Min.} \quad (\text{A.7})$$

It leads to

$$2 \sum_{n=N_i}^{N_n} \left(A_n \sum_{k=1}^N p_n(y_k) p_m(y_k) \right) = \sum_{k=1}^N p(y_k) p_m(y_k) \quad (\text{A.8})$$

where m varies as $N_i \leq m \leq N_n$. Evaluation of Eqn. A.8 gives the A_n and inserting these amplitudes into the Eqn. A.3 results in the distribution function $f(r)$.

Compared to earlier approaches towards Abel inversion, this algorithm is relatively insensitive to noise and errors in the determination of the object's center[PJN⁺92]. Here, the fundamental idea is to fit the whole projected images to a set of cosine expansion based integrals. We used this Abel inverse algorithm for retrieving the detailed absorbance obtained from the transient optical transmission images and consequently give the free carrier density estimations from the Drude formalism as discussed in chapter 2. For example in the Fig. A.2 (a) and (b), we show the absorbance without (i.e., assuming a constant density profile) and with the Abel inverse transform for a laser pulse energy of $44 \mu\text{J}/\text{pulse}$ and pulse duration of 4.2 ps .

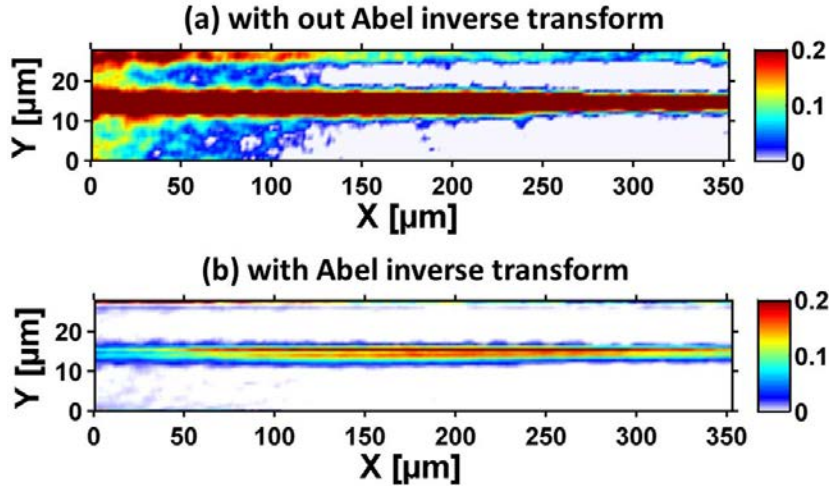


Figure A.2: Absorbance profiles derived from the OTM images with out (a) and with (b) the Abel inverse transform are shown for the plasma object induced by a laser pulse energy of $44 \mu\text{J}/\text{pulse}$ and pulse duration of 4.2 ps .

Bibliography

- [ABDL⁺03] C. Altucci, R. Bruzzese, C. De Lisio, M. Nisoli, E. Priori, S. Stagira, L. Pascolini, M. and Poletto, P. Villorosi, V. Tosa, and K. Midorikawa. Phase-matching analysis of high-order harmonics generated by truncated bessel beams in the sub-10-fs regime. *Phys. Rev. A*, 68(3):033806, 2003.
- [AD00] J. Arlt and K. Dholakia. Generation of high-order bessel beams by use of an axicon. *Opt. Commun.*, 177(1):297–301, 2000.
- [ADDS⁺94] P. Audebert, Ph. Daguzan, A. Dos Santos, J. C. Gauthier, J. P. Geindre, S. Guizard, G. Hamoniaux, K. Krastev, P. Martin, G. Petite, and A. Antonetti. Space-time observation of an electron gas in SiO_2 . *Phys. Rev. Lett.*, 73:1990–1993, Oct 1994.
- [ASF03] J. Amako, D. Sawaki, and E. Fujii. Microstructuring transparent materials by use of nondiffracting ultrashort pulse beams generated by diffractive optics. *J. Opt. Soc. Am. B*, 20(12):2562–2568, 2003.
- [BBS⁺07] I. M. Burakov, N. M. Bulgakova, R. Stoian, A. Mermillod-Blondin, E. Audouard, A. Rosenfeld, A. Husakou, and I. V. Hertel. Spatial distribution of refractive index variations induced in bulk fused silica by single ultrashort and short laser pulses. *J. Appl. Phys.*, 101(4):043506, 2007.
- [BBS⁺08] Y. Bellouard, E. Barthel, A. A. Said, M. Dugan, and P. Bado. Scanning thermal microscopy and raman analysis of bulk fused silica exposed to lowenergy femtosecond laser pulses. *Opt. Express*, 16(24):19520–19534, 2008.
- [BCL⁺10a] M. K. Bhuyan, F. Courvoisier, P-A. Lacourt, M. Jacquot, L. Furfaro, M. J. Withford, and J. M. Dudley. High aspect ratio taper-free microchannel fabrication using femtosecond bessel beams. *Opt. Express*, 18(2):566–574, 2010.

- [BCL⁺10b] M. K. Bhuyan, F. Courvoisier, P. A. Lacourt, M. Jacquot, R. Salut, L. Furfaro, and J. M. Dudley. High aspect ratio nanochannel machining using single shot femtosecond besell beams. *Appl. Phys. Lett.*, 97(8):081102, 2010.
- [BCP⁺11] M. K. Bhuyan, F. Courvoisier, H. S. Phing, O. Jedrkiewicz, S. Recchia, P. Di Trapani, and J. M. Dudley. Laser micro-and nanostructuring using femtosecond besell beams. *Eur. Phys. J. Spec. Top.*, 199(1):101–110, 2011.
- [BCZ08] O. Brzobohatý, Tomáš Cizmar, and P. Zemánek. High quality quasi-bessel beam generated by round-tip axicon. *Opt. Exp.*, 16(17):12688–12700, 2008.
- [BDG09] M. Bock, S. K. Das, and R. Grunwald. Programmable ultrashort-pulsed flying images. *Opt. Express*, 17(9):7465–7478, 2009.
- [BDG12] M. Bock, S. K. Das, and R. Grunwald. Ultrashort highly localized wavepackets. *Opt. Express*, 20(11):12563–12578, 2012.
- [BMTS08] T. Balciunas, A. Melninkaitis, G. Tamosauskas, and V. Sirutkaitis. Time-resolved off-axis digital holography for characterization of ultrafast phenomena in water. *Opt. Lett.*, 33(1):58–60, 2008.
- [BOJR51] A. H. Bennett, H. Osterberg, H. Jupnik, and O. W. Richards. *Phase microscopy: principles and applications*. Wiley New York, 1951.
- [Bor88] Z. Bor. Distortion of femtosecond laser pulses in lenses and lens systems. *J. Mod. Opt.*, 35(12):1907–1918, 1988.
- [Bor89] Z. Bor. Distortion of femtosecond laser pulses in lenses. *Opt. Lett.*, 14(2):119–121, 1989.
- [Boy03] R. W. Boyd. *Nonlinear optics*. Academic press, 2003.
- [BVC⁺14] M. K. Bhuyan, P. K. Velpula, J-P. Colombier, T. Olivier, N. Faure, and R. Stoian. Single-shot high aspect ratio bulk nanostructuring of fused silica using chirp-controlled ultrafast laser besell beams. *Appl. Phys. Lett.*, 104:021107, 2014.

- [BWC98] Z. Bouchal, J. Wagner, and M. Chlup. Self-reconstruction of a distorted nondiffracting beam. *Opt. Commun.*, 151(4):207–211, 1998.
- [CC87] M. Combescot and R. Combescot. Conductivity relaxation time due to electron-hole collisions in optically excited semiconductors. *Phys. Rev. B*, 35(15):7986, 1987.
- [CFM⁺06] A. Couaïron, M. Franco, G. Méchain, T. Olivier, B. Prade, and A. Mysyrowicz. Femtosecond filamentation in air at low pressures: Part i: Theory and numerical simulations. *Opt. Commun.*, 259(1):265–273, 2006.
- [CL77] L. G. Cohen and C. Lin. Pulse delay measurements in the zero material dispersion wavelength region for optical fibers. *Appl. Opt.*, 16(12):3136–3139, 1977.
- [CM07] A. Couaïron and A. Mysyrowicz. Femtosecond filamentation in transparent media. *Phys. Reports*, 441(2):47–189, 2007.
- [CRC⁺03] N. Chattrapiban, E. A. Rogers, D. Cofield, W. T. Hill III, and R. Roy. Generation of nondiffracting bessel beams by use of a spatial light modulator. *Opt. Lett.*, 28(22):2183–2185, 2003.
- [CRO⁺11] A. Crespi, R. Ramponi, R. Osellame, L. Sansoni, I. Bongioanni, F. Sciarrino, G. Vallone, and P. Mataloni. Integrated photonic quantum gates for polarization qubits. *Nature Commun.*, 2:566, 2011.
- [CSF⁺05] A. Couaïron, L. Sudrie, M. Franco, B. Prade, and A. Mysyrowicz. Filamentation and damage in fused silica induced by tightly focused femtosecond laser pulses. *Phys. Rev. B*, 71:125435, Mar 2005.
- [CSM04] Y. Cheng, K. Sugioka, and K. Midorikawa. Microfluidic laser embedded in glass by three-dimensional femtosecond laser microprocessing. *Opt. Lett.*, 29(17):2007–2009, 2004.
- [CXW05] I. H. Chowdhury, X. Xu, and A. M. Weiner. Ultrafast double-pulse ablation of fused silica. *Appl. Phys. Lett.*, 86(15):151110, 2005.
- [DA12] M. Duocastella and C. B. Arnold. Bessel and annular beams for materials processing. *Laser & Photonics Rev.*, 6(5):607–621, 2012.

- [DBB⁺13] J. A. Dharmadhikari, R. Bernard, A. K. Bhatnagar, D. Mathur, and A. K. Dharmadhikari. Axicon-based writing of waveguides in bk7 glass. *Opt. Lett.*, 38(2):172–174, 2013.
- [DCC96a] J. A. Davis, E. Carcole, and D. M. Cottrell. Intensity and phase measurements of nondiffracting beams generated with a magneto-optic spatial light modulator. *Appl. Opt.*, 35(4):593–598, 1996.
- [DCC96b] J. A. Davis, E. Carcole, and D. M. Cottrell. Nondiffracting interference patterns generated with programmable spatial light modulators. *Appl. Opt.*, 35(4):599–602, 1996.
- [DM] M. W. Davidson and A. Mortimer. Optical microscopy. *online material from* <http://www.olympusmicro.com/primer/microscopy.pdf>.
- [DMJE87] J. Durnin, J. J. Miceli Jr., and J. H. Eberly. Diffraction-free beams. *Phys. Rev. Lett.*, 58(15):1499–1501, 1987.
- [DMSH96] K. M. Davis, K. Miura, N. Sugimoto, and K. Hirao. Writing waveguides in glass with a femtosecond laser. *Opt. Lett.*, 21(21):1729–1731, 1996.
- [Dri84] H. M. Van Driel. Optical effective mass of high density carriers in silicon. *Appl. Phys. Lett.*, 44(6):617, 1984.
- [DSS⁺10] B. Dusser, Z. Sagan, H. Soder, N. Faure, J-P. Colombier, M. Jourlin, and E. Audouard. Controlled nanostructures formation by ultra fast laser pulses for color marking. *Opt. Express*, 18(3):2913–2924, 2010.
- [EHS⁺97] M. Erdelyi, Z. L. Horvath, G. Szabo, Z. Bor, F. K. Tittel, J. R. Cavallaro, and M. C. Smayling. Generation of diffraction-free beams for applications in optical microlithography. *J. Vac. Sci. & Tech. B*, 15(2):287–292, 1997.
- [ERH⁺07] L. Englert, B. Rethfeld, L. Haag, M. Wollenhaupt, C. Sarpe-Tudoran, and T. Baumert. Control of ionization processes in high band gap materials via tailored femtosecond pulses. *Opt. Express*, 15(26):17855–17862, 2007.
- [FHS90] AJ Fisher, W Hayes, and AM Stoneham. Theory of the structure of the self-trapped exciton in quartz. *Journal of Physics: Condensed Matter*, 2(32):6707, 1990.

- [FPA⁺00] J. Fan, E. Parra, I. Alexeev, K. Y. Kim, H. M. Milchberg, L. Y. Margolin, and L. N. Pyatnitskii. Tubular plasma generation with a high-power hollow bessel beam. *Phys. Rev. E*, 62(6):R7603, 2000.
- [FW11] J. Fischer and M. Wegener. Three-dimensional direct laser writing inspired by stimulated-emission-depletion microscopy [invited]. *Opt. Mat. Exp.*, 1(4):614–624, 2011.
- [Gae00] A. L. Gaeta. Catastrophic collapse of ultrashort pulses. *Phys. Rev. Lett.*, 84(16):3582, 2000.
- [Gam11] E. G. Gamaly. The physics of ultra-short laser interaction with solids at non-relativistic intensities. *Phys. Reports*, 508(4):91–243, 2011.
- [GCMM⁺02] V. Garcés-Chávez, D. McGloin, H. Melville, W. Sibbett, and K. Dholakia. Simultaneous micromanipulation in multiple planes using a self-reconstructing light beam. *Nature*, 419(6903):145–147, 2002.
- [GM08] R. R. Gattass and E. Mazur. Femtosecond laser micromachining in transparent materials. *Nature Photon.*, 2:219–225, 2008.
- [GVICR⁺01] J. C. Gutiérrez-Vega, M. D. Iturbe-Castillo, G. A. Ramirez, E. Tepichin, R. M. Rodriguez-Dagnino, S. Chávez-Cerda, and G. H. C. New. Experimental demonstration of optical mathieu beams. *Opt. Commun.*, 195(1):35–40, 2001.
- [GVJ⁺06] E. Gaizauskas, E. Vanagas, V. Jarutis, S. Juodkazis, V. Mizeikis, and H. Misawa. Discrete damage traces from filamentation of gauss-bessel pulses. *Opt. Lett.*, 31(1):80–82, 2006.
- [HKP04] A. Horn, E. W. Kreutz, and R. Poprawe. Ultrafast time-resolved photography of femtosecond laser induced modifications in bk7 glass and fused silica. *Appl. Phys. A*, 79(4-6):923–925, 2004.
- [Hor03] A. Horn. Zeitaufgelöste analyse der wechselwirkung von ultrakurz gepulster laserstrahlung mit dielektrika. *PhD thesis, Fakultät fuer Maschinenwesen der Rheinisch-Westfälischen Technischen Hochschule Aachen*, 2003.

- [HSKR10] C. Hnatovsky, V. G. Shvedov, W. Krolikowski, and A. V. Rode. Materials processing with a tightly focused femtosecond laser vortex pulse. *Opt. Lett.*, 35(20):3417–3419, 2010.
- [JMH⁺06] S. Juodkazis, H. Misawa, T. Hashimoto, E. G. Gamaly, and B. Luther-Davies. Laser-induced microexplosion confined in a bulk of silica: Formation of nanovoids. *Appl. Phys. Lett.*, 88(20):201909–201909, 2006.
- [JMX⁺14] V. Jukna, C. Milián, C. Xie, T. Itina, J. Dudley, F. Courvoisier, and A. Couairon. Filamentation with nonlinear bessel vortices. *Opt. Express*, 22(21):25410–25425, 2014.
- [JNT⁺06] S. Juodkazis, K. Nishimura, S. Tanaka, H. Misawa, E. G. Gamaly, B. Luther-Davies, L. Hallo, Ph. Nicolaï, and V. T. Tikhonchuk. Laser-induced microexplosion confined in the bulk of a sapphire crystal: evidence of multimegabar pressures. *Phys. Rev. Lett.*, 96(16):166101, 2006.
- [JPS00] V. Jarutis, R. Paškauskas, and A. Stabinis. Focusing of laguerre-gaussian beams by axicon. *Opt. Commun.*, 184(1):105–112, 2000.
- [KHP05] E. W. Kreutz, A. Horn, and R. Poprawe. Electron excitation in glasses followed by time-and space-measuring tools. *Appl. Surf. Sci.*, 248(1):66–70, 2005.
- [KPKK09] V. V. Kononenko, V. P. Pashinin, M. S. Komlenok, and V. I. Konov. Laser-induced modification of bulk fused silica by femtosecond pulses. *Laser Phys.*, 19(6):1294–1299, 2009.
- [KRVS00] A. Kaiser, B. Rethfeld, M. Vicanek, and G. Simon. Microscopic processes in dielectrics under irradiation by subpicosecond laser pulses. *Phys. Rev. B*, 61(17):11437, 2000.
- [KS08] Peter G Kazansky and Yasuhiko Shimotsuma. Self-assembled sub-wavelength structures and form birefringence created by femtosecond laser writing in glass: properties and applications. *J. Ceram. Soc. Japan*, 116(1358):1052–1062, 2008.
- [LCL⁺13] Y. Liao, Y. Cheng, C. Liu, J. Song, F. He, Y. Shen, D. Chen, Z. Xu, Z. Fan, X. Wei, K. Sugioka, and K. Midorikawa. Direct laser writing of sub-50 nm nanofluidic channels buried in glass

- for three-dimensional micro-nanofluidic integration. *Lab Chip*, 13(8):1626–1631, 2013.
- [LGTL04] S. Liu, H. Guo, H. Tang, and M. Liu. Direct acceleration of electrons using single hermite–gaussian beam and bessel beam in vacuum. *Phys. Lett. A*, 324(2):104–113, 2004.
- [Mar75] JH Marburger. Self-focusing: theory. *Progress in Quant. Elect.*, 4:35–110, 1975.
- [Mau10] C. Mauchair. Spatio–temporal ultrafast laser tailoring for bulk functionalization of transparent materials. *PhD thesis, Université Jean Monnet, France and Freie Universität Berlin, Germany*, 2010.
- [MB07] A. Mermillod–Blondin. Analysis and optimization of ultrafast laser–induced bulk modifications in dielectric materials. *PhD thesis, Université Jean Monnet, France and Freie Universität Berlin, Germany*, 2007.
- [MD05] D. McGloin and K. Dholakia. Bessel beams: diffraction in a new light. *Cont. Phys.*, 46(1):15–28, 2005.
- [MDA⁺08] G. D. Marshall, P. Dekker, M. Ams, J. A. Piper, and M. J. Withford. Directly written monolithic waveguide laser incorporating a distributed feedback waveguide-bragg grating. *Opt. Lett.*, 33(9):956–958, 2008.
- [MDV⁺13] K. Mishchik, C. D’Amico, P. K. Velpula, C. Mauchair, A. Boukenter, Y. Ouerdane, and R. Stoian. Ultrafast laser induced electronic and structural modifications in bulk fused silica. *J. Appl. Phys.*, 114(13):133502, 2013.
- [MGD⁺97] P. Martin, S. Guizard, Ph. Daguzan, G. Petite, P. d’Oliveira, P. Meynadier, and M. Perdrix. Subpicosecond study of carrier trapping dynamics in wide-band-gap crystals. *Phys. Rev. B*, 55(9):5799, 1997.
- [Mis12] K. Mishchik. Ultrafast laser-induced modification of optical glasses : a spectroscopy insight into the microscopic mechanisms. *PhD thesis, Université Jean Monnet, France*, 2012.

- [MJM⁺01] A. Marcinkevičius, S. Juodkazis, S. Matsuo, V. Mizeikis, and H. Misawa. Application of bessel beams for microfabrication of dielectrics by femtosecond laser. *Jpn. J. Appl. Phys.*, 40(11A):L1197, 2001.
- [MKŠ⁺13] Mindaugas Mikutis, Tadas Kudrius, Gintas Šlekys, Domas Paipulas, and Saulius Juodkazis. High 90% efficiency bragg gratings formed in fused silica by femtosecond gauss-bessel laser beams. *Optical Materials Express*, 3(11):1862–1871, 2013.
- [Mou13] A. Mouskeftaras. Study of the physical mechanisms involved in the femtosecond laser optical breakdown of dielectric materials. *PhD thesis, Laboratoire des Solides Irradiés, Ecole Polytechnique, ParisTech.*, 2013.
- [MQG⁺04] S. S. Mao, F. Quéré, S. Guizard, X. Mao, R. E. Russo, G. Petite, and P. Martin. Dynamics of femtosecond laser interactions with dielectrics. *Appl. Phys. A*, 79(7):1695–1709, 2004.
- [MSGMD10] M. Mazilu, D. J. Stevenson, F. Gunn-Moore, and K. Dholakia. Light beats the spread: non-diffracting beams. *Laser & Photonics Rev.*, 4(4):529–547, 2010.
- [MSZR05] M. Mero, A. J. Sabbah, J. Zeller, and W. Rudolph. Femtosecond dynamics of dielectric films in the pre-ablation regime. *Appl. Phys. A*, 81(2):317–324, 2005.
- [MZC⁺12] C. Mauchair, M. Zamfirescu, G. Colombier, J-P. and Cheng, K. Mishchik, E. Audouard, and R. Stoian. Control of ultrafast laser-induced bulk nanogratings in fused silica via pulse time envelopes. *Opt. Express*, 20(12):12997–13005, 2012.
- [NWB03] S. Nolte, M. Will, J. Burghoff, and A. Tuennermann. Femtosecond waveguide writing: a new avenue to three-dimensional integrated optics. *Appl. Phys. A*, 77(1):109–111, 2003.
- [NWI⁺96] H. Nishikawa, E. Watanabe, D. Ito, Y. Sakurai, K. Nagasawa, and Y. Ohki. Visible photoluminescence from si clusters in γ -irradiated amorphous sio₂. *J. Appl. Phys.*, 80(6):3513–3517, 1996.
- [PCF⁺07] P. Polesana, A. Couairon, D. Faccio, A. Parola, M. A. Porras, A. Dubietis, A. Piskarskas, and P. Di Trapani. Observation

of conical waves in focusing, dispersive, and dissipative kerr media. *Phys. Rev. Lett.*, 99(22):223902, 2007.

- [PFC⁺08] P. Polesana, M. Franco, A. Couairon, D. Faccio, and P. Di Trapani. Filamentation in kerr media from pulsed bessel beams. *Phys. Rev. A*, 77(4):043814, 2008.
- [PJN⁺92] G. Pretzier, H. Jager, T. Neger, H. Philipp, and J. Woisetschlager. Comparison of different methods of abel inversion using computer simulated and experimental side-on data. *Z. Naturforsch*, 47(a):955–970, 1992.
- [PPF⁺04] M. A. Porras, A. Parola, D. Faccio, A. Dubietis, and P. Di Trapani. Nonlinear unbalanced bessel beams: stationary conical waves supported by nonlinear losses. *Phys. Rev. Lett.*, 93(15):153902, 2004.
- [Pre91] G. Pretzier. A new method for numerical abel-inversion. *Z. Naturforsch*, 46(a):639–641, 1991.
- [PZT07] D. G. Papazoglou, I. Zergioti, and S. Tzortzakis. Plasma strings from ultraviolet laser filaments drive permanent structural modifications in fused silica. *Opt. lett.*, 32(14):2055–2057, 2007.
- [QGM⁺99] F Quéré, S Guizard, P Martin, G Petite, O Gobert, P Meynadier, and M Perdrix. Ultrafast carrier dynamics in laser-excited materials: subpicosecond optical studies. *Applied Physics B*, 68(3):459–463, 1999.
- [Ret04] B. Rethfeld. Unified model for the free-electron avalanche in laser-irradiated dielectrics. *Phys. Rev. Lett.*, 92(18):187401, 2004.
- [RKMW07] D. E. Roskey, M. Kolesik, J. V. Moloney, and E. M. Wright. Self-action and regularized self-guiding of pulsed bessel-like beams in air. *Opt. Express*, 15(16):9893–9907, 2007.
- [RVC08] J. Reif, O. Varlamova, and F. Costache. Femtosecond laser induced nanostructure formation: self-organization control parameters. *Appl. Phys. A*, 92(4):1019–1024, 2008.
- [SB02] A. M. Streltsov and N. F. Borrelli. Study of femtosecond-laser-written waveguides in glasses. *J. Opt. Soc. Amer. B*, 19(10):2496–2504, 2002.

- [SBDC07] G. A. Siviloglou, J. Broky, A. Dogariu, and D. N. Christodoulides. Observation of accelerating airy beams. *Phys. Rev. Lett.*, 99(21):213901, 2007.
- [SBM01] C. B. Schaffer, A. Brodeur, and E. Mazur. Laser-induced breakdown and damage in bulk transparent materials induced by tightly focused femtosecond laser pulses. *Measurement Sci. and Tech.*, 12(11):1784, 2001.
- [SC14] K. Sugioka and Y. Cheng. Femtosecond laser three-dimensional micro-and nanofabrication. *Appl. Phys. Rev.*, 1(4):041303, 2014.
- [SCF⁺02] L. Sudrie, A. Couairon, M. Franco, B. Lamouroux, B. Prade, S. Tzortzakis, and A. Mysyrowicz. Femtosecond laser-induced damage and filamentary propagation in fused silica. *Phys. Rev. Lett.*, 89(18):186601, 2002.
- [SCM⁺14] R. Stoian, J-P. Colombier, C. Mauclair, G. Cheng, M. K. Bhuyan, P. K. Velpula, and P. Srisungsitthisunti. Spatial and temporal laser pulse design for material processing on ultrafast scales. *Appl. Phys. A*, 114(1):119–127, 2014.
- [Ser89] B. E. Sernelius. Generalized drude approach to the conductivity relaxation time due to electron-hole collisions in optically excited semiconductors. *Phys. Rev. B*, 40(18):12438, 1989.
- [SFH⁺96] BC Stuart, MD Feit, S Herman, AM Rubenchik, BW Shore, and MD Perry. Nanosecond-to-femtosecond laser-induced breakdown in dielectrics. *Physical Review B*, 53(4):1749, 1996.
- [SG93] P. N. Saeta and B. I. Greene. Primary relaxation processes at the band edge of sio 2. *Phys. Rev. Lett.*, 70(23):3588, 1993.
- [Shl88] A. L. Shluger. The model of a triplet self-trapped exciton in crystalline sio2. *J. Phys. C: Solid State Phys.*, 21(13):L431, 1988.
- [SHM10] K. Sugioka, Y. Hanada, and K. Midorikawa. Three-dimensional femtosecond laser micromachining of photosensitive glass for biomicrochips. *Laser & Photonics Rev.*, 4(3):386–400, 2010.
- [SJM⁺05] Q. Sun, H. Jiang, Y. Liu, Z. Wu, H. Yang, and Q. Gong. Measurement of the collision time of dense electronic plasma

- p>induced by a femtosecond laser in fused silica.
- Opt. Lett.*
- , 30(3):320–322, 2005.
- [SSV⁺10] L. Sansoni, F. Sciarrino, G. Vallone, P. Mataloni, A. Crespi, R. Ramponi, and R. Osellame. Polarization entangled state measurement on a chip. *Phys. Rev. Lett.*, 105:200503, Nov 2010.
- [SSV⁺12] L. Sansoni, F. Sciarrino, G. Vallone, P. Mataloni, A. Crespi, R. Ramponi, and R. Osellame. Two-particle bosonic-fermionic quantum walk via integrated photonics. *Phys. Rev. Lett.*, 108(1):010502, 2012.
- [ST05] M. Sakakura and M. Terazima. Initial temporal and spatial changes of the refractive index induced by focused femtosecond pulsed laser irradiation inside a glass. *Phys. Rev. B*, 71(2):024113, 2005.
- [SWJ⁺08] R. Schmidt, C. A. Wurm, S. Jakobs, J. Engelhardt, A. Egner, and S. W. Hell. Spherical nanosized focal spot unravels the interior of cells. *Nat. Methods*, 5(6):539–544, 2008.
- [TBLS⁺11] R. R. Thomson, T. A. Birks, S. G. Leon-Saval, A. K. Kar, and J. Bland-Hawthorn. Ultrafast laser inscription of an integrated photonic lantern. *Opt. Express*, 19(6):5698–5705, 2011.
- [TLY] S. H. Tao, W. M. Lee, and X. Yuan. Experimental study of holographic generation of fractional bessel beams.
- [TSTZ⁺06] VV Temnov, K Sokolowski-Tinten, P Zhou, A El-Khamhawy, and D Von Der Linde. Multiphoton ionization in dielectrics: comparison of circular and linear polarization. *Physical review letters*, 97(23):237403, 2006.
- [VP03] V. Vaičaitis and Š. Paulikas. Formation of bessel beams with continuously variable cone angle. *Opt. and Quant. Elec.s*, 35(11):1065–1071, 2003.
- [VTF89] A. Vasara, J. Turunen, and A. T. Friberg. Realization of general nondiffracting beams with computer-generated holograms. *JOSA A*, 6(11):1748–1754, 1989.

- [WBS⁺06] S. W. Winkler, I. M. Burakov, R. Stoian, N. M. Bulgakova, A. Husakou, A. Mermillod-Blondin, A. Rosenfeld, D. Ashkenasi, and I. V. Hertel. Transient response of dielectric materials exposed to ultrafast laser radiation. *Appl. Phys. A*, 84(4):413–422, 2006.
- [WKNW13] R. J. Williams, R. G. Krämer, S. Nolte, and M. J. Withford. Femtosecond direct-writing of low-loss fiber bragg gratings using a continuous core-scanning technique. *Optics letters*, 38(11):1918–1920, 2013.
- [WSL⁺08] H. Wang, L. Shi, B. Lukyanchuk, C. Sheppard, and C. T. Chong. Creation of a needle of longitudinally polarized light in vacuum using binary optics. *Nature Phot.*, 2(8):501–505, 2008.
- [YB86] G-Z. Yang and N. Bloembergen. Effective mass in picosecond laser-produced high-density plasma in silicon. *IEEE J. Quantum Electron.*, 22(1):195, 1986.
- [Zer55] F. Zernike. How i discovered phase contrast. *Science*, 121(3141):345–349, 1955.
- [ZGBK14] J. Zhang, M. Gecevičius, M. Beresna, and P. G. Kazansky. Seemingly unlimited lifetime data storage in nanostructured glass. *Phys. Rev. Lett.*, 112(3):033901, 2014.

Appendix B

Acknowledgements

The presented work in this thesis is absolutely not be accomplished by a single person. Therefore, it is time to express my sincere gratitude to the people who have supported me directly and indirectly to finish this wonderful work.

First, I would like to thank Prof. Florent Pigeon, Directeur, Laboratoire Hubert Curien for providing me the excellent working environment and all necessary facilities to carry out this work.

I am very grateful to my thesis reporters (rapporteurs) Dr. Stephane Guizard and Dr. Francoise Courvoisier for dedicating their important time to going through my thesis and providing their valuable remarks. Also thank them for their fruitful discussions. Additionally I would like to thank Dr. F. Courvoisier for providing the FIB cleaved SEM images of our structures. I am also thankful to examiners (examineurs) of my PhD thesis defense, Prof. Javier Solis, Dr. Betrand Poumellec, Prof. Florence Garrelie and Prof. Youcef Ouerdane for dedicating their valuable time and evaluating my work.

My sincere thanks goes to my supervisor, Dr. Razvan Stoian for his encouragement and unconditional assistance. His depth of knowledge and focus in the field helped me a great extent. His friendly guidance and rigorous discussions on broad fields of laser-matter interaction strengthen my skills and lead to a confident researcher. I thank him again for everything that he did during this memorable stay, since day one I landed here.

Equally, I would also like to thank my co-supervisor Dr. Jean-Philippe Colombier for his great association for numerical simulations. He has been so friendly and encouraged me at any stage. Also I should not forget to mentioned him a special thanks for doing all the French administrative things and French translation whenever I required.

It is difficult to realize this work with out support form Dr. Manoj Kumar Bhuyan. He has been there always for any single doubt and dis-

cussion about the problem which I encountered. His expertise in the field of non-diffracting (Bessel) beams helped me enormously. Thanks Manoj for everything.

I would like to thank Mr. Nicola Faure for his wonderful technical assistance and arranging me the convenient laser timings (although I never offered him any doughnut's). I would like to say a special thanks to him for helping me with the Labview programming.

I would also like to thank Dr. Cyril Mauclair for his great help when I am setting up pump-probe microscopy. Also I thank him for his discussions and basic guidance to handling the pump-probe setup and EMCCD camera.

Many thanks to Dr. Ciro D'amico for his excellent support and stimulating discussions on nonlinear optics. Also I would like to thank Dr. Konstantin Mishchik for his wonderful discussions about fused silica and laser induced defect centers which helped me to get a broad scope on laser-induced damage in transparent materials. Thanks to Dr. Hao Zhang for providing me the FDTD simulations.

I thank Dr. Tatiana Itina, Prof. Aziz Boukenter, Prof. Sylvain Girard, Dr. Emmanuel Marin, Dr. Thomas Olivier and Dr. Florent Bourquard for their direct and indirect support during this stay.

Thanks to Mr. Gérard Bernaud for his extraordinary support to make sample holders and many other hardware designs according to our experimental need. Thanks to Mrs. Julie Debiesse for her great help concerning all administrative work during this stay.

My sincere thanks to Prof. D. Narayana Rao for his excellent support and encouragement. Also many thanks to Dr. Soma Venugopal Rao, Dr. Anchal Srivastava for their wonderful guidance and help.

My thanks also goes to the other LaHC colleagues who have made my stay more memorable and enjoyable. A special thanks goes to Chiru, Andrey, Emile, Deigo, David, Adriana, Chiara, Serena, Nikita, Thibault, Teddy, Sedo, Anton, Julien, Maxime and Chen. (I hope I did not miss anyone)

I thank friends from image processing group for their great help whenever I needed to treat the image with Matlab. Always they have a immediate solution for my problems or questions. Thanks to Hasnat, Mohammad, Rahat and Rahul.

I would like to thank my friends and previous colleagues at University of Hyderabad for their support and encouragement. Special thanks to Dr. Kallepalli Lakshmi Narayana Deepak, Dr. Manoj Kumar Brundavanam, Dr. Bala Murali Krishna, Dr. Sadik Ali, Dr. Valigantla Sreeramulu, Dr. Guddala Sriram, Dr. Sai Kiran, Dr. Sai Santosh Kumar, Dr. Shivakiran Bhaktha, Dr. Venkatram Nalla and Dr. Krishna Chaitanya Vishnubatla.

Also many thanks to my dear friends, Bandi Raju, Kiran, Malli, Edla

Raju, Lakshun, Inam, Tatiana, Sakina, Lynn, Bua (Ar-pha), Chinna, Mahesh, Santosh, Joshi, Srinu, Om Prakash, Raju and Prasanna.

Finally, I would especially thank my family members, particularly my parents and my dear sister for their unconditional support and love to finish this work.

Appendix C

Publications

International Journals

- **P. K. Velpula**, M. K. Bhuyan, F. Courvoisier, H. Zhang, J. P. Colombier, and R. Stoian “Spatio-temporal dynamics of nondiffractive Bessel ultrafast laser nanoscale structuring” (manuscript under preparation).
- M. K. Bhuyan, **P. K. Velpula**, J. P. Colombier, F. Courvoisier and R. Stoian “Self-limited axial energy deposition in transparent materials using nonlinear Bessel beams”, Opt. Lett., 2015 (submitted).
- **P. K. Velpula**, M. K. Bhuyan, C. Mauchair, J.P. Colombier, R. Stoian “Role of free carriers excited by ultrafast Bessel beams for sub-micron structuring applications”, Opt. Eng., 53 (7), 076108 (2014).
- **P. K. Velpula**, M. K. Bhuyan, C. Mauchair, J.P. Colombier, R. Stoian “Ultrafast imaging of free carriers: controlled excitation with chirped ultrafast laser Bessel beams” Proceedings of SPIE, 8967-37 (2014).
- M. K. Bhuyan, **P. K. Velpula**, J. P. Colombier, T. Olivier, N. Faure and R. Stoian “Single-shot high aspect ratio bulk structuring of fused silica using chirp-controlled ultrafast laser Bessel beams”, Appl. Phys. Lett., 104 (2), 021107 (2014).
- R. Stoian, J. P. Colombier, C. Mauchair, M. Bhuyan, **P. K. Velpula**, P. Srisungsitthisunti “Spatial and temporal laser pulse design for material processing on ultrafast scales”, Appl. Phys. A., 114(1), 119-127 (2013).
- K. Mishchik, C. D’Amico, **P. K. Velpula**, C. Mauchair, A. Boukenter, Y. Ouerdane, and R. Stoian “Ultrafast laser induced electronic and structural modifications in bulk fused silica”, J. Appl. Phys. 114, 133502 (2013).

Oral presentations

- “Ultrafast imaging of highly efficient submicron structures fabrication using nondiffractive Bessel beams”, LASE, SPIE Photonics West, 06 Feb. 2014 San Francisco, USA (**Best student paper award**).
- “Time-resolved dynamics of ultrafast Bessel and Gaussian beam propagation and energy deposition in transparent materials”, 12 Oct. 2013, EUROMAT, Sevilla, Spain.
- “High aspect ratio submicron fabrication in bulk dielectrics with non-diffractive ultrafast Bessel beams; dynamics and interaction regimes”, 17 June. 2014, Laser Precision Microfabrication (LPM), Lithuania.

Poster presentations

- **P. K. Velpula**, M. K. Bhuyan, J. P. Colombier, and R. Stoian “High aspect ratio nanoscale structuring in transparent materials using ultrafast Bessel beams; A dynamic view on the underlying physical mechanisms”, HCERES Comité dévaluation, Laboratoire Hubert Curien, Université Jean Monnet, France (2015).
- **P. K. Velpula**, M. K. Bhuyan, C. Mauchair, J. P. Colombier, and R. Stoian “Sub-micron structuring and its ultrafast physics using engineered fs laser beams”, Journée de la recherche, Université Jean Monnet, France (2014).
- **P. K. Velpula**, M. K. Bhuyan, C. Mauchair, J. P. Colombier, and R. Stoian “Static and transient dynamics of ultrafast Bessel beam propagation and energy deposition in transparent materials”, Séminaire LABEX MANUTECH-SISE, Marcoux, France (2013).
- M. K. Bhuyan, **P. K. Velpula**, J. P. Colombier, and R. Stoian “Single-Shot Bulk Structuring of Transparent Materials Using Ultrafast Bessel Beams”, COLA, Italy (2013).